Impact on air quality of carbon and sulfur volatile compounds emitted from hydrothermal discharges: the case study of Pisciarelli (Campi Flegrei, South Italy).

R. Biagi[a]*, F. Tassi[a,b], S. Caliro[c], F. Capecchiacci[a], S. Venturi[a,b]

[a]*Department of Earth Sciences, University of Florence, Via G. La Pira 4, 50121 Firenze (Italy)*

[b]*Institute of Geosciences and Earth Resources (IGG), National Research Council of Italy (CNR), Via G. La Pira 4, 50121 Firenze (Italy)*

[c]*National Institute of Geophysics and Volcanology (INGV), Department of Naples, Osservatorio Vesuviano, Via Diocleziano 328, 80124 Napoli (Italy)*

* Corresponding author. Department of Earth Sciences, University of Florence, Via G. La Pira 4, 50121 Firenze (Italy). Tel: +39 3316312879. E-mail: rebecca.biagi1@stud.unifi.it – rebecca.biagi6@gmail.com

Submitted to Science of the Total Environment

Abstract

Volcanoes are currently to be regarded as natural sources of air pollutants. Climatic and environmental forcing of large volcanic eruptions are well known, although gases emitted through passive degassing during periods of quiescence or hydrothermal activity can also be highly dangerous for the environment and public health. Based on compositional and isotopic data, a survey on the spatial distribution in air of the main volatile compounds of carbon (CO_2 and CH_4) and sulfur (H_2S and SO_2) emitted from the fumarolic field of Pisciarelli (Campi Flegrei, Pozzuoli, Naples), a hydrothermal area where degassing activity has visibly increased since 2009, was carried out. The main goals of this study were (i) to evaluate the impact on air quality of these natural manifestations and (ii) inquire into the behavior of the selected chemical species once released in air, and their possible use as tracers to distinguish natural and anthropogenic sources. Keeling plot analysis of CO_2 and CH_4 isotopes revealed that the hydrothermal area acts as a net source of CO_2 in air, whilst CH_4 originated entirely from anthropogenic sources. Approaching the urban area, anthropogenic sources of CO_2 increased and, at distances greater than 800 m from the Pisciarelli field, they prevailed over the hydrothermal signal. While hydrothermal CO_2 simply mixed with that in the atmospheric background, H_2S was possibly affected by oxidation processes. Therefore, SO_2 measured in the air near the hydrothermal emissions had a secondary origin, i.e. generated by oxidation of hydrothermal H_2S. Anthropogenic SO_2 was recognized only in the furthest measurement site from Pisciarelli. Finally, in the proximity of a geothermal well, whose drilling was in progress during our field campaign, the H_2S concentrations have reached values up to 3 orders of magnitude higher than the urban background, claiming the attention of the local authorities.

Keywords: *hydrothermal systems, air quality, carbon isotopes, hydrothermal volatile compounds.*

1. Introduction

Air pollution poses a serious hazard to public health and environment. According to the World Health Organization (WHO), deaths caused by exposure to polluted air were around 4.2 million worldwide in 2016, while 90 % of people live in places where concentrations of pollutants in the air exceed the recommended threshold values (WHO, 2018). Air pollutants from anthropogenic activity are regarded as the main causes of global scale phenomena having a dramatically impact on ecosystems and human

health, such as greenhouse effect, the ozone hole, and acidic rains, (McCormick et al., 1995; Robock, 2000; Monks et al., 2009; Burton et al., 2013).

Volcanoes are significant sources of air pollutants, such as trace elements (Calabrese et al., 2016, and references therein) and acidic gases (Reikard, 2019, and references therein). Magmas contain dissolved volatiles (mostly consisting of water vapor, CO_2, and SO_2) that are released in large quantities during (i) volcanic eruptions (e.g., Robock, 2004; Self, 2005) and (ii) long periods of quiescence through a persistent diffuse degassing or fumarolic vents (e.g., Mörner and Etiope, 2002; Aiuppa, 2015; Cardellini et al., 2017). Water vapor and CO_2 are regarded as two of the main greenhouse gases, whereas SO_2 and H_2S, the latter being mainly produced by SO_2 reduction in a hydrothermal environment, react in air with hydroxyl radicals (OH) and water vapor producing H_2SO_4 that forms aerosol that reflects solar radiation, causing a generalized cooling of the troposphere and the warming of the stratosphere (Rampino and Self, 1982; Self et al., 1993; McCormick et al., 1995). Sulfur-bearing volatiles also concur to (i) the degradation of the ozone layer, (ii) production of acidic rains, and (iii) air pollution known as "volcanic smog" or "vog" (McGee et al., 1997; Andres and Kasgnoc, 1998; Robock, 2000; Textor et al., 2003; von Glasow et al., 2009).

Most studies focused on the environmental and climatic impacts and the associated risks of large eruptions (e.g. Robock, 1981; Kelly and Sear, 1984; Allard et al., 1991a; Hansen et al., 1992; Self et al., 1993; McCormick et al., 1995; Robock, 2000; Oppenheimer, 2003; Textor et al., 2003; Robock, 2004; Self et al., 2004; Self, 2005; Horwell and Baxter, 2006; Self, 2006; von Glasow et al., 2009; Gerlach, 2011; Raible et al., 2016), whereas little is known about the fate of gases emitted during the long-lasting non-eruptive periods and hydrothermal activity. Recent studies have shown that volcanoes emit to the atmosphere a huge amount of volatiles even during quiescent periods (Baubron et al., 1990; Allard et al., 1991a; Delmelle et al., 2002; Mörner and Etiope, 2002). For instance, Mount Etna (Sicily, South Italy) emits about 21×10^9 g day^{-1} of TV (Total Volatile) (Aiuppa et al., 2008); Stromboli Island (Aeolian Islands, South Italy) 6-12 $\times 10^9$ g day^{-1} (Allard et al., 1994) and the volcano Masaya (Nicaragua) 14-16 $\times 10^9$ g day^{-1} (Burton et al., 2000; Martin et al., 2010; Girona et al., 2014).

Campi Flegrei caldera (CFc) in southern Italy, one of the most active volcanic complexes of the Mediterranean area, hosts the densely populated Pozzuoli town (1,844 inhabitants per square kilometer

in 2019; AdminStat, 2020), thus representing one of the most prominent example of coexistence of human settlements with active volcanic systems. CFc is currently showing an intense hydrothermal activity, mostly occurring (i) at the Solfatara Crater and (ii) in an area approximately 400 m eastward from Solfatara namely Pisciarelli, where the hydrothermal discharge rate has been strongly increased in the last decade (Chiodini et al., 2015, 2017; Tamburello et al., 2019).

In this study, we present the results of a geochemical survey carried out at five sites near the Pisciarelli hydrothermal field, where high-frequency measurements in air of CO_2, CH_4, SO_2 and H_2S concentrations, and $\delta^{13}C\text{-}CO_2$ and $\delta^{13}C\text{-}CH_4$ values were performed. The main aim was to investigate the spatial distribution of the fluids emitted in air from the Pisciarelli hydrothermal discharges in order to (i) evaluate their impact on air quality and (ii) inquire into the behavior of the selected chemical species once released in air, and their possible use as tracers to distinguish natural (hydrothermal) and anthropogenic sources.

2 Study area

The Phlegrean Volcanic District is a volcanic complex of alkali-potassic affinity (Florio et al., 1999) located along the Tyrrhenian margin, NW of Naples (Italy). It consists of a series of monogenic volcanic edifices, including the islands of Procida and Ischia, and submarine vents in the northwestern Gulf of Naples (Orsi et al., 1996). The morpho-structural setting is dominated by collapsed structures produced during two main eruptive events: (i) the Campanian Ignimbrite eruption (39 ka; De Vivo et al., 2001), which originated a first caldera, and (ii) the Neapolitan Yellow Tuff eruption, which caused a further collapse about 14.9 ka (Orsi et al., 1996, 2004; Deino et al., 2004). The last eruptive activity occurred in 1538 A.D. (Monte Nuovo eruption; Di Vito et al., 1987; Orsi et al., 1996), whereas bradyseismic crises occurred in 1970-72 and 1982-84 (Barberi et al., 1984; Bonafede and Mazzanti, 1998), the latter causing ground uplifts up to 3.5 m, a situation that imposed the evacuation of more than 40,000 people in 1984 (Barberi et al., 1984; De Vivo et al., 2001). These slow vertical ground movements were accompanied by thousands of earthquakes with epicenters at the Solfatara Crater (Vilardo et al., 1991), a 1.4 km^2-wide tuff cone (Fig. 1a) produced about 4 ka from a low-magnitude eruption (Isaia et al., 2009).

Solfatara crater hosts the most prominent hydrothermal discharges in CFc (Chiodini et al., 2012; Cardellini et al., 2017), whose deep source (2,000-2,500 m depth) is a liquid-dominated aquifer at ≥ 360 °C and 200-250 bar, overlain by a vapor-dominated zone at 200-240 °C (Caliro et al., 2007, and references therein). Pisciarelli, located approximately 400 m eastward of the Solfatara Crater, is a 0.03 km^2 hydrothermal fault-related system (67 m a.s.l.) including several high-flow fumaroles and boiling pools (Fig. 1b). In this site, a significant increase of both shallow seismicity and hydrothermal activity has recently been observed, as testified by the opening of a new fumarolic vent in 2009 emitting fluids with temperatures up to 114 °C (Chiodini et al., 2015; Tamburello et al., 2019). Recent studies (Aiuppa et al., 2013, Queißer et al., 2017; Tamburello et al., 2019) have shown that the fluid output from Pisciarelli in the last years account for several kilotons for day, with >29 MW of energy being released from only the 2009 fumarole.

Hydrothermal diffuse emissions and weak fumaroles occur along the Antiniana street, a densely urbanized sector of CFc located about 1 km south of Pisciarelli in the Agnano crater. In this area, two geothermal wells are also present, one abandoned and showing a low flow rate, the other, characterized by a strong flow rate, drilled in June 2020 (INGV-OV, 2020).

3. Materials and methods

3.1 Measurement strategy

Carbon- and sulfur-bearing pollutants on air were measured in January and June 2020. During the first campaign, the measurements were carried out at four sites, as follows: (i) FU ("Fumaroles"), (ii) AC ("Artificial Conduit"), (iii) HT ("Hotel Tennis"), and (iv) DS ("Distal Site") (Fig. 1b). During the second campaign, the measurements were (i) performed at the GW ("Geothermal Well") site, and (ii) repeated at the AC site.

The FU site was the closest one (about 85 m; Fig. 1b) to the main hydrothermal discharges of Pisciarelli, whereas the AC site was at the entrance of a sport center (about 120 m far from the Pisciarelli discharges; Fig. 1b) at few meters from a cemented conduit that conveys to air the hydrothermal fluids discharged by emissions covered the local infrastructures. The GW site was located within a car parking along the Antiniana street, i.e. close (about 40 m) to the geothermal well in drilling (Fig. 1b). The HT site was

situated inside the parking lot of a hotel, at about 325 m from the main Pisciarelli hydrothermal discharges (Fig. 1b). Noteworthily, the parking lot hosts the outlet tubing of the hotel boiler system, discharging vapors at relatively high rate. The DS site was the farthest one (about 800 m) from the main Pisciarelli hydrothermal discharges (Fig. 1b). It was located along Pisciarelli street, a trafficked road connecting the homonymous locality (belonging to the Municipality of Pozzuoli) to Agnano (part of the 10th Municipality of Naples).

Timing and duration of the measurement sessions carried out at each site were reported in Table 1.

3.2 Instrumental equipment and data acquisition

CO_2 and CH_4 concentration (in mg/m^3) and the δ^{13}C-CO_2 and δ^{13}C-CH_4 values (in ‰ vs. V-PDB) were measured by WS-CRDS (Wavelenght-Scanned Cavity Ring-Down Spectroscopy) using a Picarro G2201-*i* analyzer. This instrument is characterized by a high data acquisition frequency (1 measurement for second) and precision values of 0.4 mg/m^3 (CO_2), 0.03 mg/m^3 (CH_4), 0.16 ‰ (δ^{13}C-CO_2) and 1.15 ‰ (δ^{13}C-CH_4) (Venturi et al., 2020 and references therein). As suggested by Malowany et al. (2015), a copper-stripes trap was installed at the analyzer inlet port to minimize spectral interferences caused by high concentrations of H_2S, which could result in significant depletion in ^{13}C. H_2S and SO_2 concentrations (in µg/m^3) were measured by PF (Pulsed Fluorescence) using a Thermo® 450*i* analyzer (Thermo Fisher Scientific, 2012). The instrument, providing 1 measurement for min, has detection limits of 5.2 and 2.8 µg/m^3 for SO_2 and H_2S, respectively, and precision of ± 1 % (Venturi et al., 2016, 2019). Air samples were drawn through Teflon tubing using vacuum pumps with sampling rate of 25 mL min^{-1} and 70 mL min^{-1} for the Picarro and the Thermo, respectively. Minute-averages were obtained from the dataset acquired from each instrument and used for further data processing.

Meteorological parameters (wind speed, wind direction, humidity, and temperature) were also measured using a portable Kestrel® 4500 meteorological station (Kestrel®, 2020) which were integrated with those available online at www.wunderground.com.

3.3 Keeling-plot analysis

CO_2 and CH_4 parameters (concentrations and δ^{13}C values) were analyzed according to the Keeling plot analysis (Keeling, 1958, 1961), to recognize the main sources of these gases. The method relies on a

two members-mixing model, i.e. the environmental background and local source(s), and is based on two mass balance equations (Pataki et al., 2003; Venturi et al., 2020):

i) $C_m = C_b + C_s$

ii) $\delta^{13}C_m \times C_m = \delta^{13}C_b \times C_b + \delta^{13}C_s \times C_s$

where C and δ^{13}C are the concentration and the carbon isotopic composition of the gaseous species respectively, and *m*, *b* and *s* subscripts refer to the measured, background and source(s) values respectively. By combining equations (i) and (ii) as follows (iii), a straight line is identified on a 1/C vs. δ^{13}C plot, whose intercept corresponds to the isotopic signature of the emitting source:

iii) $\delta^{13}C_m = \frac{(\delta^{13}C_b - \delta^{13}C_s) \times C_b}{C_m} + \delta^{13}C_s$

When the gas concentration increases, the isotopic ratios tend to move away from the background values as a function of the source(s) characteristics. The background values can remain unknown, but both the background and source(s) values are assumed to be constant during the observation period (Pataki et al., 2003; Venturi et al., 2020).

Considering the prerequisite of constant mixing of background and sources, we applied the Keeling plot analysis to short-time intervals (≤6 hours) at each site, having pre-processed data in 5min-moving averages, which allowed to improve the stability in data trends, attenuating the oscillations due to sudden gusts of wind. Data reduction (minute-averages and moving averages) were performed using R (R Core Team, 2017) implemented with the Openair package (Carslawand Ropkins, 2012; Carslaw, 2014).

The R^2 determination coefficient was used to verify the ability of the linear regression model to describe the data distribution. The estimated isotopic data is not to be considered reliable when $R^2 < 0.75$.

4. Results

The summary descriptive statistical parameters (minimum, maximum, mean, median, standard deviation) on the minute-averaged data measured at each site, and meteorological parameters (wind direction, wind speed), are reported in Table 1.

4.1 Meteorological parameters

During the first campaign of measurements, the weather was mainly fairly. On 21st January 2020, prevailing wind direction blew from NE-NNE in the late afternoon, with wind speed around 13 km/h, and from N-NW sector during nighttime, with lower wind speed (5-11 km/h) (Tab. 1). On 22nd January 2020, prevailing wind directions blew from N-NNE in the early morning, while during the late morning, the afternoon and nighttime they were mostly variable with a speed constantly <8 km/h (Tab. 1). On 23rd January 2020, wind speed was relatively low (3-5 km/h), mostly from N-NE (Tab. 1).

During the second campaign, the weather conditions were partially cloudy or cloudy. On the afternoon of 9th June 2020, wind direction blew mainly from W, with wind speed ranging from 19 to 22 km/h (Tab. 1). In the morning and afternoon of 10th June 2020, wind direction blew mainly from W with wind speed from 11 to 24 km/h (Tab. 1). Eventually, on the morning of 11th June 2020, prevailing wind direction came from SSW-SW, with wind speed from 11 to 19 km/h (Tab. 1).

Air temperature was higher in June (19-23 °C) than in January 2020 (3-15 °C). During both the observation periods, it followed a typical diurnal cycle, characterized by maximum values at early afternoon and minimum at nighttime and early morning.

Air humidity was higher in January (minimum 48%, maximum 100%) than in June 2020 (minimum 34%, maximum 73%), and reached the highest values during nighttime and the lowest ones at midday.

4.2 Concentrations and $\delta^{13}C$ values of CO_2 and CH_4

4.2.1 CO_2

The measurement sites located near the main fumaroles (FU), the new geothermal well (GW), and the cemented conduit at the entrance of the sport center (AC) displayed relatively high CO_2 concentrations, ranging from 922 to 1,677, from 746 to 1,197, and from 774 to 1,068 mg/m^3, respectively (Tab. 1), whereas the $\delta^{13}C$-CO_2 values were from -10.51 to -5.94, from -10.30 to -6.82, and from -7.97 to -5.74 ‰ vs. V-PDB, respectively (Tab. 1). At FU, the mean and median values of CO_2 concentrations and $\delta^{13}C$-CO_2 were 1,090 and 1,054 mg/m^3 (SD: 120; Tab. 1), and -8.61 and -8.73 ‰ vs. V-PDB (SD: 0.09), respectively. The distribution of these data was almost symmetric with a slight right-skew. At the AC site, CO_2 concentrations were on average higher on January 2020 (mean: 980 mg/m^3, median: 939 mg/m^3, SD: 107; Tab. 1) than on June 2020 (mean: 831 mg/m^3, median: 801 mg/m^3, SD: 77; Tab. 1), whereas the average $\delta^{13}C$-CO_2 values on January 2020 (mean: -8.85 ‰ vs. V-PDB, median: -8.84 ‰

vs. V-PDB, SD: 0.73; Tab.1) and on June 2020 (mean: -8.43 ‰ vs. V-PDB, median: -8.61 ‰ vs. V-PDB, SD: 0.61; Tab. 1) were similar. At GW site, the mean and median values of CO_2 concentrations and $\delta^{13}C\text{-}CO_2$ were, respectively, as follows: 884 and 879 mg/m^3 (SD: 53; Tab. 1), and -7.05 and -7.02 ‰ vs. V-PDB (SD: 0.36; Tab. 1) in the morning of 10th June 2020; 871 and 875 mg/m^3 (SD: 66; Tab. 1), and -6.89 and -6.90 ‰ vs. V-PDB (SD: 0.52; Tab. 1) in the afternoon of 10th June 2020; 864 and 853 mg/m^3 (SD: 55; Tab. 1) and -7.22 and -7.27 ‰ vs. V-PDB (SD: 0.36; Tab. 1) on 11th June 2020. CO_2 concentrations and isotopic values showed a direct correlation in all the three sites (Fig. A.1-6).

Surprisingly, the highest CO_2 concentrations were measured at the distal HT site, where they ranged from 1,087 to 2,109 mg/m^3 on 21st-22nd January 2020 (mean: 1,567 mg/m^3, median: 1,580 mg/m^3, SD: 230; Tab. 1), and from 1,170 to 2,193 mg/m^3 on 22nd-23rd January 2020 (mean: 1,591 mg/m^3, median: 1,584 mg/m^3, SD: 153; Tab. 1). The $\delta^{13}C\text{-}CO_2$ values ranged from -12.41 to -5.82 ‰ vs. V-PDB on 21st-22nd January 2020 (mean: -7.58 ‰ vs. V-PDB, median: -7.06 ‰ vs. V-PDB, SD: 1.50; Tab. 1), and from -11.38 to -5.65 ‰ vs. V-PDB on 22nd-23rd January 2020 (mean: -7.31 ‰ vs. V-PDB, median: -7.00 ‰ vs. V-PDB, SD: 1.03; Tab. 1). Similarly to the previous sites, CO_2 concentrations and isotopic values were directly correlated (Fig. A.7 and A.8). During both the measurement sessions carried out at this site, the CO_2 concentrations (and the associated isotopic values) were significantly higher at nighttime than in the morning (Fig. A.7 and A.8). Relatively high CO_2 concentrations (from 998 to 1,374 mg/m^3, mean: 1,176 mg/m^3, median: 1,145 mg/m^3, SD: 0.14; Tab 1) were also measured at the other distal site (DS), where the $\delta^{13}C\text{-}CO_2$ values ranged from -14.33 and -12.52 ‰ vs. V-PDB (mean and median: -13.6 ‰ vs. V-PDB, SD: 0.40; Tab. 1). Notably, in this case CO_2 concentrations and $\delta^{13}C\text{-}CO_2$ values were inversely correlated (Fig. A.9).

4.2.2 CH_4

During the period of observation, the CH_4 concentrations measured at the FU site showed minor variations (from 1.41 to 1.46 mg/m^3; Tab. 1) around the mean value of 1.43 mg/m^3 and the median value of 1.42 mg/m^3 (SD 0.009; Tab. 1) (Fig. A.10). At AC, CH_4 concentrations ranged from 1.26 to 1.40 mg/m^3 and were on the average higher on January 2020 (mean and median: 1.40 mg/m^3, SD: 0.003; Tab. 1) than on June 2020, when the mean and median CH_4 concentrations values were both 1.27 mg/m^3 (SD: 0.002; Tab.1) (Fig. A.11 and A.12). The GW site displayed almost constant CH_4 concentrations

during the three measuring sessions (average values: 1.30 mg/m^3; Tab. 1), ranging from 1.29 to 1.33 mg/m^3 (SDs: 0.003 and 0.005 on 10th June 2020, and 0.004 on 11th June 2020; Tab. 1) (Fig. A.13-15). Overall, CH_4 concentrations at sites near hydrothermal discharges were lower on June (i.e. at AC and GW sites) than on January (i.e. FU and AC sites).

At the HT site, CH_4 showed almost constant concentrations during nighttime, with mean values of 1.45 mg/m^3 (median: 1.43 mg/m^3, SD: 0.05; Tab. 1) on 21st-22nd January 2020, and 1.42 mg/m^3 (median: 1.40 mg/m^3, SD: 0.05; Tab. 1) on 22nd-23rd January 2020, whereas increasing trends occurred in the morning, from 1.43 to 1.63 mg/m^3 and from 1.40 to 1.53 mg/m^3, respectively (Fig. A.16 and A.17). It is worth noting that the highest CH_4 concentration (1.72 mg/m^3), measured at 3:35 on 23rd January 2020 (Fig. A.17), corresponds to a negative peak of CO_2 concentrations (Fig. A.8). At DS site, the CH_4 concentrations ranged from 1.54 to 2.23 mg/m^3, with a mean value of 1.69 mg/m^3 and a median value of 1.66 mg/m^3 (SD: 0.14; Tab. 1).

The δ^{13}C-CH_4 values varied over a relatively wide range among the measuring sites. At FU, the δ^{13}C-CH_4 ranged from -49.8 to -43.8 ‰ vs. V-PDB (mean and median: -45.9 ‰ vs. V-PDB, SD: 0.88; Tab. 1). At AC site, δ^{13}C-CH_4 values varied from -49.3 to -44.7 ‰ vs. V-PDB on January 2020 (Tab. 1), and from -52.8 to -48.5 ‰ vs. V-PDB on June 2020 (Tab. 1), showing on average more negative values on spring (mean: -50.8 ‰ vs. V-PDB, median: -50.7 ‰ vs. V-PDB, SD: 0.88; Tab. 1) than on winter (mean and median: -47.0 ‰ vs. V-PDB, SD: 0.75; Tab. 1). The δ^{13}C-CH_4 values measured on 10th (morning and afternoon) and 11th June 2020 at GW site ranged from -51.2 to -45.0, from -48.7 to -44.1 and from -48.8 to -45.4 ‰ vs. V-PDB, respectively (mean: -48.6, -46.6, and -47.0 ‰ vs. V-PDB, respectively; median: -48.5, -46.6, and -46.8 ‰, respectively; and SD: 1.17, 0.94, and 0.84, respectively; Tab. 1). According to the measures of central tendency of these three sites, the δ^{13}C-CH_4 data were distributed symmetrically around the average values. At the HT site, the δ^{13}C-CH_4 values ranged from -50.4 to -44.2 ‰ vs. V-PDB on 21st-22nd January 2020 (Tab. 1), and from -50.0 to -45.2 ‰ vs. V-PDB on 22nd-23rd January 2020 (Tab. 1). The coincidence of the mean (-46.3 and -47.1 ‰ vs. V-PDB, respectively; Tab. 1) and median values (-46.2 and -47.1 ‰ vs. V-PDB, respectively; Tab. 1) suggests a symmetrical distribution of data (SD: 0.86 and 0.78, respectively; Tab. 1). The DS site showed δ^{13}C-CH_4 values from -49.9 to -44.8 ‰ vs. V-PDB (Tab. 1), with a mean value of -47.8 ‰ vs. V-PDB and a median value of

-47.7 ‰ vs. V-PDB (SD: 1.10; Tab. 1). Differently from CO_2, no clear correlation was observed between CH_4 concentrations and $\delta^{13}C$-CH_4 values.

4.3 Concentrations of H_2S and SO_2

The concentrations of H_2S and SO_2 at the FU site ranged from 94 to 1,333 µg/m^3 (mean: 362 µg/m^3, median: 326 µg/m^3, SD: 183; Tab. 1) and from 7.05 to 44 µg/m^3 (mean: 20 µg/m^3, median: 18 µg/m^3, SD: 7.3; Tab. 1), respectively, and showed a positive correlation (Fig. A.19). Significantly lower H_2S and SO_2 concentrations were measured at the AC site both in January 2020 (from 0.78 to 82 µg/m^3 and from 1.30 to 9.79 µg/m^3, respectively) and in June 2020 (from 1.40 µg/m^3 to 396 µg/m^3 and from 3.26 to 29 µg/m^3, respectively) (Tab. 1; Fig. A.20 and A.21). The average concentrations of both S-bearing species were less abundant on winter (H_2S and SO_2 mean: 10 and 4.58 µg/m^3 respectively, H_2S and SO_2 median: 7.64 and 4.19 µg/m^3 respectively, H_2S and SO_2 SD: 12 and 1.7 respectively; Tab. 1) than on spring (H_2S and SO_2 mean: 45 and 10 µg/m^3 respectively, H_2S and SO_2 median: 8.48 and 9.22 µg/m^3 respectively, H_2S and SO_2 SD: 68 and 5.4 respectively; Tab. 1). The difference in mean and median values on H_2S and SO_2 concentrations in June 2020 displayed a right-skew distribution of data, suggesting that, in this case, the median value should be the most reliable position measure for the descriptive statistic. The highest H_2S concentrations were measured at the GW site (Fig. A.22-24), where they ranged from 2.28 to 1,570 µg/m^3 (Tab. 1), whereas SO_2 concentrations were from 9.10 to 87 µg/m^3 (Tab. 1). The mean and median H_2S concentrations values were, respectively, 497 and 460 µg/m^3 in the morning of 10th June 2020 (SD: 188.223; Tab. 1), 375 and 357 µg/m^3 in the afternoon of 10th June 2020 (SD: 254; Tab. 1), and 233 and 175 µg/m^3 on 11th June 2020 (198; Tab. 1), whereas the mean and median values of SO_2 concentrations were 42 and 39 µg/m^3 (SD: 10.6; Tab. 1), 37 and 38 µg/m^3 (SD: 15.5; Tab. 1), and 20 and 18 µg/m^3 (SD: 8.6; Tab. 1), respectively.

At the HT site, H_2S concentrations varied from 10 to 618 µg/m^3 on 21st-22nd January 2020 (mean: 192 µg/m^3, median: 180 µg/m^3, SD: 126; Tab. 1), and from 5.83 to 126 µg/m^3 on 22nd-23rd January 2020 (mean: 44 µg/m^3, median: 35 µg/m^3, SD: 29; Tab. 1), whereas SO_2 concentrations were from 0.54 to 21 µg/m^3 on 21st-22nd January 2020 (mean: 9.15 µg/m^3, median: 8.22 µg/m^3, SD: 4.2; Tab. 1), and ≤11 µg/m^3 on 22nd-23rd January 2020 (mean: 4.50 µg/m^3, median: 4.33 µg/m^3, SD: 1.9; Tab. 1). During the first measuring night, H_2S and SO_2 concentrations were relatively high, showing a positive correlation

296 (except at lower H_2S values; Fig. A.25). The DS site was characterized by H_2S and SO_2 concentrations
297 ranging from 27 to 91 $\mu g/m^3$ and from 11 to 92 $\mu g/m^3$ (Tab. 1), with mean and median concentration
298 values of 52 and 46 $\mu g/m^3$ for H_2S (SD: 16; Tab. 1), and 23 and 17 $\mu g/m^3$ for SO_2 (SD: 15; Tab. 1), and
299 showed an inverse correlation (Fig. A.27).
300
301 **5. Discussion**
302 **5.1 Hydrothermal fluid input in the air**
303 In order to investigate the distribution and behavior of the hydrothermal gases in the air, as well as their
304 possible use as tracers to distinguish natural and anthropogenic sources in environments where human
305 settlements and hydrothermal fluid discharges coexist, we firstly analyzed the chemical and isotopic
306 data measured in air from sites located near to the main hydrothermal discharges.
307 Excluding water vapor, CO_2 and H_2S are the main volatile species commonly emitted by hydrothermal
308 systems (Carapezza et al., 1984, 2003; Caliro et al., 2007; Granieri et al., 2009; Viveiros et al., 2010;
309 Cabassi et al., 2017). CO_2 is also emitted in the air from several other natural sources (mainly vegetation
310 and oceans; Carlson et al., 2001; Riebeek and Simmon, 2011), and most anthropic activities related to
311 the massive exploitation and combustion of fossil fuels (Venturi et al., 2019, 2020), resulting in global
312 air background concentrations up to 730 mg/m^3 (NOAA/ESRL Global Monitoring Division;
313 www.esrl.noaa.gov/gmd), which basically represent the "background air" value. H_2S is naturally
314 produced in wetlands and stagnant water under reducing conditions (Rubright et al., 2017 and references
315 therein), and by different human activities, e.g. pulp and paper mills, rayon textile manufacturing,
316 chemical manufacturing, waste disposal (Llavador Colomer et al., 2012), extraction and refining of oil
317 and natural gas, production of geothermal energy (WHO, 1981, 2000a, 2003; NYS Department of
318 Health, 2005; Thorsteinsson et al., 2013; Rubright et al., 2017). Hence, in those sites of the study area
319 located in the proximity of the hydrothermal discharges (FU, GW and AC; Fig. 1b), the measured CO_2
320 was deriving from both the hydrothermal contributions and a large list of undefined anthropogenic
321 sources that basically constitute the local background, whereas no significant H_2S sources, other than
322 the hydrothermal discharges, can be recognized. In agreement with these considerations, the H_2S/CO_2
323 ratios measured at FU and GW strongly increased with the H_2S concentrations, approaching those of

gases directly collected from the corresponding hydrothermal discharges, i.e. Pisciarelli fumarole (Caliro et al., 2007) and the geothermal well (INGV, 2020) (Fig. 2a), although the discharged hydrothermal gases were strongly diluted (up to 3 orders of magnitude) at the FU and GW measurement stations. On the other hand, as the H_2S concentrations decreased, the H_2S/CO_2 ratio decreased, according with a distribution basically controlled only by dilution with the local background (Fig. 2a). However, in the H_2S vs. CO_2 binary diagram (Fig. 2b), the FU and GW data display a significant CO_2-enrichment with respect to the dilution curves (blue and magenta dashed lines), suggesting (i) a local heterogeneity of background CO_2 (trend A) likely due to anthropogenic inputs from the urban area, and (ii) a partial H_2S depletion (trend B) possibly caused by oxidizing processes typically affecting this gas compound in air, as observed by Badalamenti et al. (2001) and Carapezza et al. (2003) based on measurement of air composition in other areas affected by hydrothermal emissions. Both the H_2S concentrations and H_2S/CO_2 ratios measured at AC were on average lower than those measured at the other two proximal sites (FU and GW). At a first approximation, this could be ascribed to the relatively long distance separating AC and the Pisciarelli fumarole (Fig. 1b) and/or to the occurrence of anthropogenic inputs of CO_2 affecting the AC background value (Fig. 2b; trend A). However, it has to be considered that the measurements at the AC site were likely influenced by gas emissions from the cemented conduit located just few meters away (Fig. 1b). Gases from this source were likely depleted in H_2S, being fed by emissions at the periphery of the Pisciarelli main emitting site, where the shallow aquifer has a relatively high pH (Crognale et al., 2021). This hypothesis is confirmed by the distribution of the AC measurements in the CO_2 vs. H_2S binary diagram (Fig. 2b; trend B), showing relatively low H_2S concentrations at CO_2 values comparable to those measured at FU and GW. Noteworthy, part of the AC samples plot at intermediate position between the AC main group and the FU samples, particularly in June (Fig. 2b), suggesting occasional contributions from the Pisciarelli fumaroles related to more favorable wind conditions.

By applying the Keeling plot analysis (Keeling, 1958, 1961) to the CO_2 concentrations in air measured at the FU site (Fig. 3a), assuming a two-member mixing model between background air and hydrothermal gases, the isotopic signature of CO_2 discharged from the Pisciarelli fumaroles was estimated at -0.41 ± 0.21 ‰ vs. V-PDB ($R^2 = 0.82$; Tab. 2). As expected, this value is consistent with

those reported in literature (e.g. Caliro et al., 2007) for fumarolic CO_2 of the Pisciarelli area. According to a similar approach (Fig. 3b), the $\delta^{13}C$-CO_2 estimates based on the data acquired at the GW site on 11th June (when winds were blowing from SSW-SW, i.e. the measurement equipment was upwind to the geothermal well; Fig. 1b) allowed to confirm the hydrothermal origin of the fluids emitted by the geothermal well under construction (-2.51 ± 0.30 ‰ vs V-PDB, R^2 = 0.78; Tab 2). On the contrary, on 10th June the coefficients of determination R^2 were too low to determine with certainty the isotopic signature of the CO_2 source (-6.54 ± 0.44 ‰ vs V-PDB, R^2 = 0.002, and -1.21 ± 0.38 ‰ vs V-PDB, R^2 = 0.69, in the morning and afternoon of 10th June, respectively; Tab. 2). This might indicate that, notwithstanding the proximity to the hydrothermal fluid source (40 m, Fig. 1b), the area was affected by anthropogenic CO_2 input, controlled by variable weather conditions, producing a large dispersal of data. The $\delta^{13}C$-CO_2 values computed using the data measured at the AC site (Fig. 3c) were -2.75 ± 0.29 ‰ vs V-PDB (R^2 = 0.85) and -1.75 ± 0.16 ‰ vs. V-PDB (R^2 = 0.95) (Tab. 2) in January and June, respectively. The slight difference between the $\delta^{13}C$-CO_2 values computed for the FU and AC sites was possibly due to a more negative isotopic signature of the CO_2 emitted from the cemented conduit, likely influencing the AC site, since this gas interacted with the surficial aquifer occurring at the periphery of the Pisciarelli fumarolic area.

In urban environments, SO_2 originates from several anthropogenic activities, mainly related to the combustion of fossil fuels containing sulfur (WHO, 2000b). Accordingly, the natural SO_2 background value in highly anthropized zones is up to 25 μg/m^3, whereas in rural areas it is generally <5 μg/m^3 (WHO, 2000b). Fluids emitted from hydrothermal emissions are generally characterized by extremely low SO_2 concentrations with respect to those of H_2S, which is the most stable S-bearing gas compound at the highly reducing redox conditions typically dominating the hydrothermal reservoirs (e.g. Giggenbach, 1996). The timeplots of the H_2S and SO_2 concentrations measured at the FU, GW and AC sites (Fig. A.19-24), show that, at relatively high H_2S concentrations (>100 μg/m^3), H_2S and SO_2 have almost identical trends, suggesting that the peaks of SO_2 in air were significantly related to inputs from the hydrothermal emissions, being likely produced by oxidation of hydrothermal H_2S since primary hydrothermal SO_2 is to be considered negligible. Differently, when the hydrothermal gas fraction in air was too low, SO_2 produced from H_2S was masked by that from different, likely anthropogenic, sources.

Although CH_4 is by far the most abundant organic volatile in hydrothermal-volcanic fluids (e.g. Giggenbach, 1996), the concentrations of this gas compound in the fumarolic fluids is relatively low (about 7 mg/m^3; Caliro et al., 2007). In agreement with the dilution magnitude observed for CO_2 and H_2S (Fig. 2a), the hydrothermal contribution to the CH_4 concentrations in FU, GW and AC sites would range from 0.007 to 0.7 mg/m^3. However, is likely to assume that part of the CH_4 discharged from the hydrothermal vents was lost by oxidation in the air (e.g. Holmes, 2018). This explains the lack of any evidence of hydrothermal CH_4 contribution, as shown by the CH_4 concentrations measured in air close to the hydrothermal discharges, which were constantly <1.50 mg/m^3 (Tab. 1) and didn't display a correlation with the trends of the typical hydrothermal species (Fig. A.10-15). The latter value slightly exceeds that of global background (1.28 mg/m^3; Dlugokencky, 2021), as commonly observed in urban areas (e.g. Lowry et al., 2001; Chamberlain et al., 2016; Venturi et al., 2020, 2021), where different anthropogenic CH_4 sources, including domestic heating, vehicular traffic and landfills (e.g. Zazzeri et al., 2017), and natural inputs, including wetlands and green areas (e.g. Barlett and Harriss, 1993; Saunois et al., 2019), likely occur.

5.2 Insights from distal sites

The spatial distribution of the fluids emitted in the air from the hydrothermal discharges at increasing distance from the Pisciarelli hydrothermal field (i.e. at the HT and DS sites; Fig. 1b) was investigated to evaluate the impact of the hydrothermal emissions on the air quality of inhabited areas and their possible use as tracers to distinguish natural (hydrothermal) and anthropogenic sources.

As abovementioned, H_2S in the investigated area is to be considered purely of hydrothermal origin, whilst CH_4 was related to the local background, with no evidence of the influence of the hydrothermal gas discharges even near the main fumarolic vents. In agreement with these considerations, the concentrations in air of these two gas species, plotted in the H_2S vs. CH_4 binary diagram (Fig. 4a), were clearly independent. In fact, while the lowest CH_4 concentrations were found at those sites close to Pisciarelli, relatively high CH_4 values were measured at DS (i.e. the measurement site located at the highest distance from the fumaroles) and at HT, with no relation with the H_2S concentrations. It is worth noting that the CH_4 background values measured in winter data (FU, AC Jan, HT and DS) were significantly higher than those measured in June (AC Jun and GW) (Fig. 4a). This is possibly related to

the higher anthropogenic contribution to CH_4 emissions during the colder season due to the use of the domestic heating, as commonly observed in urban areas (Venturi et al., 2020; Venturi et al., 2021 and references therein).

Contrary to the sites close to Pisciarelli, where CH_4 concentrations were not sufficient to extrapolate information on the isotopic characteristics of the emissive source through the Keeling plot analysis, at HT and DS sites the CH_4 concentrations reached values sufficiently high to apply this statistical approach (Fig. 4b-d). Considering the prerequisite of constant mixing of background and sources, data measured at HT site, respectively, during night (0:00-5:59; Fig. 3b and 3c shaded dots) and morning (6:00-end of detection; Fig. 3b and 3c solid dots) were distinguished. As depicted in the Keeling plot of $\delta^{13}C\text{-}CH_4$ vs. $1/CH_4$ (Fig. 4b), at HT the concentrations and $\delta^{13}C$ values of CH_4 were relatively constant during nighttime on 21st-22nd January (around 1.45 mg/m^3 and −46.3 ‰ vs. V-PDB, respectively; Tab. 1), pointing to the absence of relevant local emitting sources. In the morning, the increase of the CH_4 concentrations (up to 1.64 mg/m^3; Tab. 1) was coupled with a decrease in $\delta^{13}C\text{-}CH_4$ down to -50.1 ‰ vs. V-PDB (Tab. 1). According to the Keeling plot analysis computed on the morning data, the intercept was at -60.3 ± 0.6 ‰ vs. V-PDB (Fig. 4b; Tab. 2), corresponding to $\delta^{13}C\text{-}CH_4$ values typical of biogenic sources, including landfills (around −58 ‰ vs. V-PDB; e.g. Zazzeri et al., 2017), agriculture- and livestock-related emissions (from −66 to −55 ‰ vs. V-PDB; e.g. Levin et al., 1993; Lowry et al., 2001; Townsend-Small et al., 2012; Zazzeri et al., 2017 and references therein), emissions from wastewater treatments (around −53 ‰ vs. V-PDB; e.g. Zazzeri et al., 2017) and wetlands (around −60 ‰ vs. V-PDB; e.g. Quay et al., 1988). Although the relatively low correlation coefficient of the alignment depicted by the HT morning data (R^2=0.70; Tab. 2) suggests caution to evaluate the computed isotopic signature of the CH_4 source affecting this site, it is reliable to suppose that it was mostly related gas vapors released from the outlet tubing of the boiler system hosted in the parking lot of the hotel (Fig. 1b). The Keeling plot of $\delta^{13}C\text{-}CH_4$ vs. $1/CH_4$ of the measurements carried out at the HT site on 22nd-23rd January shows a similar distribution (Fig. 4c). The $\delta^{13}C\text{-}CH_4$ endmember, estimated using the data measured during night (i.e. when the CH_4 concentrations reached the highest values, up to 1.72 mg/m^3; Tab. 1), was -58.4 ± 0.6 ‰ vs. V-PDB (R^2=0.48; Tab. 2). This isotopic value agreed with that computed with the data measured the previous day (Fig. 4b), confirming the occurrence of a local biogenic CH_4

source at the HT site. In the Keeling plot of $\delta^{13}C\text{-}CH_4$ vs. $1/CH_4$ of the DS site (Fig. 4d), which as aforementioned displayed the highest concentrations of CH_4 (up to 2.23 mg/m^3; Tab. 1), data distribution seems to be consistent with a CH_4 source having relatively high $\delta^{13}C\text{-}CH_4$ value. Such an isotopic signature, i.e. about −44 ‰ vs. V-PDB, is consistent with that of a number of urban CH_4 sources including vehicular traffic and natural gas employment (e.g. Schwietzke et al., 2016; Sherwood et al., 2017; Venturi et al., 2020, 2021 and references therein).

Notwithstanding the distance separating HT from the hydrothermal discharges of Pisciarelli, the highest concentrations of CO_2 were observed at this site (up to 2,193 mg/m^3; Tab. 1), possibly due to the static conditions of the near-surface atmosphere during nighttime and to the depressed morphology of the parking lot (Fig. 1b). As depicted in the Keeling plot of $\delta^{13}C\text{-}CO_2$ vs. $1/CO_2$ (Fig. 5), the CO_2 at HT showed isotopic characteristics that indissolubly bound it to a hydrothermal origin (-2.85 ± 0.06 ‰ vs. V-PDB, R^2=0.93; Tab. 2), even if it was affected by mixing with the atmospheric background. However, the HT site was also affected by CO_2 inputs from anthropogenic sources, possibly related, as for CH_4, to the hotel boiler emissions and local biogenic sources, which, consisting of lower CO_2 concentrations and more negative values of $\delta^{13}C\text{-}CO_2$, shifted a branch of data toward the DS site field (Fig. 5 dashed arrow). The latter is the only site whose emitted CO_2, characterized by relatively low $\delta^{13}C\text{-}CO_2$ values independently on CO_2 concentrations (Fig. 5), was purely to ascribe to anthropogenic sources related to the urban environment (e.g. Chamberlain et al., 2016; Venturi et al., 2020 and references therein).

In summary, the detected CO_2 in the study area resulted from the mixing, at different proportions, between three main endmembers: (i) the hydrothermal discharges, (ii) anthropogenic emissions and (iii) the local atmospheric background; the latter showing a significant variability both in space (e.g. AC in June and GW) and in time (e.g. AC January and AC June) (Fig. 5).

The aforementioned hypothesis of partial oxidation of the hydrothermal H_2S in the air to produce SO_2, is confirmed by the distribution of data in the SO_2 vs. H_2S binary diagram (Fig. 6), which evidences the strong (genetic) relationship between the two S-bearing gases. Data measured at the GE site were not consistent with the main trend, being SO_2 inversely correlated with H_2S (Fig. 6). This suggests that the origin of SO_2 measured at this distal site was mainly anthropogenic, i.e. related to the crowded urban settlements and the intense vehicular traffic characterizing this zone.

464

465 **5. Conclusions**

466 Hydrothermal areas are largely recognized as hot spots of pollutant emissions, thus representing an
467 environmental hazard in the near-surface atmosphere (e.g. Carapezza et al., 1984, 2003; Badalamenti et
468 al., 2001; Vaselli et al., 2011; Tassi et al., 2009, 2013, 2015; Aiuppa, 2015; Cabassi et al., 2017). This
469 study, based on a geochemical survey of air quality in the proximity of Pisciarelli, i.e. one of the main
470 hydrothermal emissions at Campi Flegrei, evidenced the occurrence of anomalously high CO_2 and H_2S
471 concentrations at the near-surface level, clearly related to the hydrothermal discharges, as confirmed by
472 the isotopic signature of CO_2 measured at sites located at a distance <325 m from the main hydrothermal
473 emission area (FU, AC, GW and HT). On the other hand, H_2S measured in these sites was to be
474 considered purely of hydrothermal origin, being the most abundant sulfur compound in hydrothermal
475 gases and in absence of significant H_2S anthropogenic sources. At HT, secondary anthropogenic CO_2
476 sources were also recognized, likely related to vapors released from the outlet tubing of a boiler system
477 hosted in the parking lot of the hotel. This hypothesis was confirmed by the occurrence of relatively
478 high concentrations of CH_4, which, on the contrary, did not show any anomalous concentrations in the
479 other measurements sites near the hydrothermal emissions (i.e. FU, AC and GW). On the whole, the
480 H_2S-CO_2 pair has proved to be a successful tracer to investigate the spatial distribution of hydrothermal
481 gases in air in the proximity of hydrothermal emission spots, the latter being dependent on (i) dilution
482 by mixing with air and (ii) consumption processes, mostly affecting H_2S through oxidation to SO_2. In
483 fact, SO_2 concentrations measured at FU, AC and GW and HT were found to be strongly related to those
484 of H_2S. At DS, i.e. the measurement site located at about 800 m from the Pisciarelli fumarolic emissions,
485 the main hydrothermal tracers (CO_2 and H_2S) were completely masked by anthropogenic sources.
486 Accordingly, anomalously high SO_2 concentrations were interpreted as related to anthropogenic
487 activities, being not accompanied by H_2S.

488 The results of this study evidence that the hydrothermal emissions discharged by the under-construction
489 geothermal well at the GW site had a significant impact on local air quality, leading to a dramatic
490 increase of CO_2 and H_2S concentrations (up to 1,061 mg/m^3 and 1,570 μg/m^3, respectively) in a densely
491 inhabited zone of Pozzuoli town. Such evidence claimed the attention of local competent authorities

492 which suspended the well construction. It is worth noting that, although CO_2 concentrations in air
493 remained well below the alert threshold of 0.5 % (OSHA, 2019), the H_2S concentrations were up to 3
494 orders of magnitude higher than those of the urban background (1-3 $\mu g/m^3$; Kourtidis et al., 2008),
495 occasionally exceeding the threshold values suggested by the WHO (2000a) for prolonged exposures,
496 i.e. 150 $\mu g/m^3$ for exposures up to 24 h, 100 $\mu g/m^3$ for exposures >14 days, and 20 $\mu g/m^3$ for exposures
497 >90 days (average values during the period). This situation may pose a potential hazard for the local
498 population, especially when weather conditions. i.e. low wind and cloudy sky, favor the accumulation
499 of H_2S in depressed areas and/or enclosed spaces.
500
501 **Acknowledgments**
502 **References**
503 AdminStat, 2020. https://ugeo.urbistat.com/AdminStat/it/it/demografia/dati-sintesi/pozzuoli/63060/4.
504 Aiuppa, A., Giudice, G., Gurrieri, S., Liuzzo, M., Burton, M., Caltabiano, T., McGonigle, A.J.S.,
505 Salerno, G., Shinohara, H., Valenza, M., 2008. Total volatile flux from Mount Etna. Geophys. Res. Lett.
506 35, L24302. https://doi.org/10.1029/2008GL035871.
507 Aiuppa, A., 2015. Volcanic-gas monitoring, in: Schmidt, A., Fristad, K., Elkins-Tanton, L. (Eds.),
508 Volcanism and Global Environmental Change. Cambridge University Press, pp. 81-96.
509 https://doi.org/10.1017/CBO9781107415683.009.
510 Allard, P., Carbonnelle, J., Dajlevic, D., Le Bronec, J., Morel, P., Robe, M.C., Maurenas, J.M., Faivre-
511 Pierret, R., Martin, D., Sabroux, J.C., Zettwoog, P., 1991a. Eruptive and diffuse emissions of CO_2 from
512 Mount Etna. Nature 351, 387-391. https://doi.org/10.1038/351387a0.
513 Allard, P., Carbonnelle, J., Métrich, N., Loyer, H., Zettwoog, P., 1994. Sulphur output and magma
514 degassing budget of Stromboli volcano. Nature 368, 326-330. https://doi.org/10.1038/368326a0.
515 Andres, R.J., Kasgnoc, A.D., 1998. A time-averaged inventory of subaerial volcanic sulfur emissions.
516 J. Geophys. Res. 103 (D19) 25,251-25,261. https://doi.org/10.1029/98JD02091.
517 Badalamenti, B., Liotta, M., Valenza, M., 2001. An automatic system for continuous monitoring of CO_2,
518 H_2S, SO_2 and meteorological parameters in the atmosphere of volcanic areas. Geochem.Trans. 5.
519 https://doi.org/10.1039/B104622P.

Barberi, F., Corrado, G., Innocenti, F., Luongo, G., 1984. Phlegraean Fields 1982-1984: Brief Chronicle of a Volcano Emergency in a Densely Populated Area. Bull. Volcanol. 47 (2) 175-185. https://doi.org/10.1007/BF01961547.

Bartlett, K.B., and Harriss, R.C., 1993. Review and assessment of methane emissions from wetlands. Chemosphere 26 (l-4), 261-320. https://doi.org/10.1016/0045-6535(93)90427-7.

Baubron, J.C., Allard, P., Toutain, J.P., 1990. Diffuse volcanic emissions of carbon dioxide from Vulcano Island, Italy. Nature 344, 51-53. https://doi.org/10.1038/344051a0.

Bonafede, M., Mazzanti, M., 1998. Modelling gravity variations consistent with ground deformation in the Campi Flegrei caldera (Italy). J. Volcanol. Geotherm. Res. 81, 137-157. https://doi.org/10.1016/S0377-0273(97)00071-1.

Burton, M.R., Oppenheimer, C., Horrocks, L.A., Francis, P.W., 2000. Remote sensing of CO_2 and H_2O emission rates from Masaya volcano, Nicaragua. Geology 28, 915-918. https://doi.org/10.1130/0091-7613(2000)28<915:RSOCAH>2.0.CO;2.

Burton, M.R., Sawyer, G.M., Granieri, D., 2013. Deep Carbon Emissions from Volcanoes. Rev. Mineral. Geochem. 75, 323-354. https://doi.org/10.2138/rmg.2013.75.11.

Calabrese, S., Randazzo, L., Daskalopoulou, K., Milazzo, S., Scaglione, S., Vizzini, S., Tramati, C.D., D'Alessandro, W., Brusca, L., Bellomo, S., Giuffrida, G.B., Pecoraino, G., Montana, G., Salerno, G., Giammanco, S., Catalbiano, T., Parello, F., 2016. Mount Etna volcano (Italy) as a mayor "dust" point source in the Mediterranean area. Arabian J. Geosci. 9, 219. https://doi.org/10.1007/s12517-015-2165-0.

Cabassi, J., Tassi, F., Venturi, S., Calabrese, S., Capecchiacci, F., D'Alessandro, W., Vaselli, O., 2017. A new approach for the measurement of gaseous elemental mercury (GEM) and H_2S in air from anthropogenic and natural sources: Examples from Mt. Amiata (Siena, Central Italy) and Solfatara Crater (Campi Flegrei, Southern Italy). J. Geochem. Explor. 175, 48-58. https://doi.org/10.1016/j.gexplo.2016.12.017.

Caliro, S., Chiodini, G., Moretti, R., Avino, R., Granieri, D., Russo, M., Fiebig, J., 2007. The origin of the fumaroles of La Solfatara (Campi Flegrei, South Italy). Geochim. Cosmochim. Acta 71, 3040-3055. https://doi.org/10.1016/j.gca.2007.04.007.

548 Carapezza, M.L., Gurrieri, S., Nuccio, P.M., Valenza, M., 1984. CO_2 and H_2S Concentrations in the
549 Atmosphere at the Solfatara of Pozzuoli. BulI. Volcanol. 47 (2) 287-293.
550 https://doi.org/10.1007/BF01961559.
551 Carapezza, M.L., Badalamenti, B., Cavarra, L., Scalzo, A., 2003. Gas hazard assessment in a densely
552 inhabited area of Colli Albani Volcano (Cava dei Selci, Roma). J. Volcanol. Geotherm. Res. 123, 81-
553 94. https://doi.org/10.1016/S0377-0273(03)00029-5.
554 Cardellini, C., Chiodini, G., Frondini, F., Avino, R., Bagnato, E., Caliro, S., Lelli, M., Rosiello, A.,
555 2017. Monitoring diffuse volcanic degassing during volcanic unrests: the case of Campi Flegrei (Italy).
556 Sci. Rep. 7 (1). https://doi.org/10.1038/s41598-017-06941-2.
557 Carlson, C. A., Bates, N. R., Hansell, D. A., Steinberg, D. K., 2001. Carbon Cycle. In: Encyclopedia of
558 Ocean Sciences: Second Edition, 477-486. Elsevier Inc. https://doi.org/10.1016/B978-012374473-
559 9.00272-1.
560 Carslaw, D.C., 2014. The Openair Manual — Open-Source Tools for Analyzing Air Pollution Data.
561 Manual for Version 1.0. King's College London.
562 Carslaw, D.C., Ropkins, K., 2012. Openair — an R package for air quality data analysis. Environ. Model
563 Softw. 27-28, 52–61. https://doi.org/10.1016/j.envsoft.2011.09.008.
564 Chamberlain, S.D., Ingraffea, A.R., Sparks, J.P., 2016. Sourcing methane and carbon dioxide emissions
565 from a small city: influence of natural gas leakage and combustion. Environ. Pollut. 218, 102–111.
566 https://doi.org/10.1016/j.envpol.2016.08.036.
567 Chiodini, G., Caliro, S., De Martino, P., Avino, R., Gherardi, F., 2012.Early signals of new volcanic
568 unrest at Campi Flegrei caldera? Insights from geochemical data and physical simulations. Geology 40,
569 943-946. https://doi.org/10.1130/G33251.1.
570 Chiodini, G., Vandemeulebrouck, J, Caliro, S., D'Auria, L., De Martino, P., Mangiacapra, A., Petrillo,
571 Z., 2015. Evidence of thermal-driven processes triggering the 2005–2014 unrest at Campi Flegrei
572 caldera. EPLS 414, 58-67. https://doi.org/10.1016/j.epsl.2015.01.012.
573 Chiodini, G., Selva, J., Del Pezzo, E., Marsan, D., De Siena, L., D'Auria, L., Bianco, F., Caliro, S., De
574 Martino, P., Ricciolino, P., Petrillo, Z., 2017. Clues on the origin of post-2000 earthquakes at Campi
575 Flegrei caldera (Italy). Sci. Rep. 7 (1), 1–10. https://doi.org/10.1038/s41598-017-04845-9.

576 Crognale, S., Venturi, S., Tassi, F., Rossetti, S., Cabassi, J., Capecchiacci, F., Bicocchi, G., Orlando, V.,
577 Morrison, H.G., Sogin, M.L., Fazi, S., 2021. The interplay between microbes and hydrothermal fluids
578 in extremely acidic environments: the case of Pisciarelli hot springs (Campi Flegrei, Italy). Into
579 submission.
580 Delmelle, P., Stix, J., Baxter, P.J., Garcia-Alvarez, J., Barquero, J., 2002. Atmospheric dispersion,
581 environmental effects and potential health hazard associated with the low-altitude gas plume of Masaya
582 volcano, Nicaragua. Bull. Volcanol. 64, 423-434. https://doi.org/10.1007/s00445-002-0221-6.
583 Deino, A.L., Orsi, G., de Vita, S., Piochi, M., 2004. The age of the Neapolitan Yellow Tuff caldera-
584 forming eruption (Campi Flegrei caldera - Italy) assessed by $^{40}Ar/^{39}Ar$ dating method. J. Volcanol.
585 Geotherm. Res. 133, 157–170. https://doi.org/10.1016/S0377-0273(03)00396-2.
586 De Vivo, B., Rolandi, G., Gans, P.B., Calvert, A., Bohrson, W.A., Spera, F.J., Belkin, H.E., 2001. New
587 constraints on the pyroclastic eruptive history of the Campanian volcanic Plain (Italy). Mineral. Petrol.
588 73, 47-65. https://doi.org/10.1007/s007100170010.
589 Di Vito, M., Lirer, L., Mastrolorenzo, G., Rolandi, G., 1987. The 1538 Monte Nuovo eruption (Campi
590 Flegrei, Italy). Bull. Volcanol. 49, 608-615. https://doi.org/10.1007/BF01079966.
591 Dlugokencky, E., 2021. NOAA/ESRL. www.esrl.noaa.gov/gmd/ccgg/trends_ch4/.
592 Florio, G., Fedi, M., Cella, F., Rapolla, A., 1999. The Campanian Plain and Phlegrean Fields: structural
593 setting from potential field data. J. Volcanol. Geotherm. Res. 91, 361-379.
594 https://doi.org/10.1016/S0377-0273(99)00044-X.
595 Gerlach, T., 2011. Volcanic Versus Anthropogenic Carbon Dioxide. EOS 92 (24), 201-208.
596 https://doi.org/10.1029/2011EO240001.
597 Giggenbach, W.F., 1996. Chemical composition of volcanic gases. In: Monitoring and Mitigation of
598 Volcano Hazards. Springer Verlag, Berlin, pp. 222–256. https://doi.org/10.1007/978-3-642-80087-0_7.
599 Girona, T., Costa, F., Newhall, C., Taisne, B., 2014. On depressurization of volcanic magma reservoirs
600 by passive degassing. J. Geophysi. Res.: Solid Earth 119, 8667-8687.
601 https://doi.org/10.1002/2014JB011368.

602 Granieri, D., Avino, R., Chiodini, G., 2009. Carbon dioxide diffuse emission from the soil: ten years of
603 observations at Vesuvio and Campi Flegrei (Pozzuoli), and linkages with volcanic activity. Bull.
604 Volcanol. 72, 103-118. https://doi.org/10.1007/s00445- 009-0304-8.
605 Hansen, J., Lacis, A., Ruedy, R., Sato, M., 1992. Potential climate impact of Mount Pinatubo eruption.
606 Geophys. Res. Lett. 19 (2), 215-218. https://doi.org/10.1029/91GL02788.
607 Holmes, C.D., 2018. Methane Feedback on Atmospheric Chemistry: Methods, Models, and
608 Mechanisms. JAMES 10, 1087–1099. https://doi.org/10.1002/2017MS001196.
609 Horwell, C.J., Baxter, P.J., 2006. The respiratory health hazards of volcanic ash: a review for volcanic
610 risk mitigation. Bull. of Volcanol. 69 (1), 1-24. https://doi.org/10.1007/s00445-006-0052-y.
611 INGV-OV, 2020. Perforazioni per pozzo Geotermico area Campi Flegrei – progetto Geogrid. Istituto
612 Nazionale di Geofisica e Vulcanologia AOO INGV Protocollo Generale – U N. 0006939 del
613 17/06/2020.
614 Isaia, R., Marianelli, P., Sbrana, A., 2009. Caldera unrest prior to intense volcanism in Campi Flegrei
615 (Italy) at 4.0 ka B.P.: implications for caldera dynamics and future eruptive scenarios. Geophys. Res.
616 Lett. 36, L21303. https://doi.org/10.1029/2009GL040513.
617 Keeling, C. D., 1958. The concentration and isotopic abundances of atmospheric carbon dioxide in rural
618 areas. Geochim. Cosmochim. Acta 13, 322-334. https://doi.org/10.1016/0016-7037(58)90033-4.
619 Keeling, C. D., 1961. The concentration and isotopic abundance of carbon dioxide in rural and marine
620 air. Geochim. Cosmochim. Acta 24, 277-298. https://doi.org/10.1016/0016-7037(61)90023-0.
621 Kelly, P.M., Sear, C.B., 1984. Climatic impact of explosive volcanic eruptions. Nature 311, 740-743.
622 https://doi.org/10.1038/311740a0.
623 Kestrel®, 2020. https://cdn.shopify.com/s/files/1/0084/9012/files/Kestrel_CoC.pdf?1810.
624 Kourtidis, K., Kelesis, A., Petrakakis, M., 2008. Hydrogen sulfide (H_2S) in urban ambient air. Atm.
625 Environm. 42, 7476-7482. https://doi.org/10.1016/j.atmosenv.2008.05.066.
626 Levin, I., Bergamaschi, P., Dörr, H., Trapp, D., 1993. Stable isotopic signature of methane from major
627 sources in Germany. Chemosphere 26 (1–4), 161–177. https://doi.org/10.1016/0045-6535(93)90419-6.
628 Llavador Colomer, F., Espinós Morató, H., Mantilla Iglesias, E., 2012. Estimation of hydrogen sulfide
629 emission rates at several wastewater treatment plants through experimental concentration measurements

and dispersion modeling, J.the Air Waste Manag. Assoc. 62 (7), 758-766. https://doi.org/10.1080/10962247.2012.674008.

Lowry, D., Holmes, C.W., Rata, N.D., O'Brien, P., Nisbet, E.G., 2001. London methane emissions: use of diurnal changes in concentration and $\delta^{13}C$ to identify urban sources and verify inventories. J. Geophys. Res. 106 (D7), 7427–7448. https://doi.org/10.1029/2000JD900601.

Malowany, K., Stix, J., Van Pelt, A., Lucic, G., 2015. H_2S interference on CO_2 isotopic measurements using a Picarro G1101-*i* cavity ring-down spectrometer. Atmos. Meas. Tech. 8, 4075-4082. https://doi.org/10.5194/amt-8-4075-2015.

Martin, R.S., Sawyer, G.M., Spampinato, L., Salerno, G.G., Ramirez, C., Ilyinskaya, E., Witt, M.L.I., Mather, T.A., Watson, I.M., Phillips, J.C., Oppenheimer, C., 2010. A total volatile inventory for Masaya Volcano, Nicaragua. J. Geophys. Res. 115, B09215. https://doi.org/10.1029/2010JB007480.

McCormick, M.P., Thomason, L.W., Trepte, C.R., 1995. Atmospheric effects of the Mt Pinatubo eruption. Nature 373, 399-404. https://doi.org/10.1038/373399a0.

McGee, K.A., Doukas, M.P., Kessler, R., Gerlach, T.M., 1997. Impacts of Volcanic Gases on Climate, the Environment, and People. U.S. Geological Survey Open-File Report 97-262. https://pubs.usgs.gov/openfile/of97-262/of97-262.html.

Monks, P.S., Granier, C., Fuzzi, S., Stohl, A., Williams, M.L., Akimoto, H., Amanni, M., Baklanov, A., Baltensperger, U., Bey, I., Blake, N., Blake, R.S., Carslawn, K., Cooper, O.R., Dentener, F., Fowler, D., Fragkou, E., Frost, G.J., Generoso, S., Ginoux, P., Grewet, V., Guenther, A., Hansson, H.C., Hennew, S., Hjorth, J., Hofzumahaus, A., Huntrieser, H., Isaksen, I.S.A., Jenkin, M.E., Kaiser, J., Kanakidou, M., Klimont, Z., Kulmala, M., Laj, P., Lawrence, M.G., Lee, J.D., Liousse, C., Maione, M., McFiggans, G., Metzger, A., Mieville, A., Moussiopoulos, N., Orlando, J.J., O'Dowd, C.S., Palmer, P.I., Parrish, D.D., Petzold, A., Platt, U., Pöschl, U., Prévôt, A.S.H., Reeves, C.E., Reimannw, S., Rudich, Y., Sellegri, K., Steinbrecher, S., Simpson, D., ten Brink, H., Theloke, J., van der Werf, G.R., Vautard, R., Vestreng, V., Vlachokostas, Ch., von Glasowbb, R., 2009. Atmospheric composition change – global and regional air quality. Atmos. Environ. 43, 5268-5350. https://doi.org/10.1016/j.atmosenv.2009.08.021.

Mörner, N.A., Etiope, G., 2002. Carbon degassing from the lithosphere. Glob. Planet. Change 33, 185-203. https://doi.org/10.1016/S0921-8181(02)00070-X.

NYS Department of Health, 2005. Hydrogen Sulfide Chemical Information Sheet. https://www.health.ny.gov/environmental/chemicals/hydrogen_sulfide/.

Oppenheimer, C., 2003. Climatic, environmental and human consequences of the largest known historic eruption: Tambora volcano (Indonesia) 1815. Prog. Phys. Geogr. 27 (2) 230-259. https://doi.org/10.1191/0309133303pp379ra.

Orsi, G., De Vita, S., Di Vito, M., 1996. The restless, resurgent Campi Flegrei nested caldera (Italy): constraints on its evolution and configuration. J. Volcanol. Geotherm. Res. 74, 179-214. https://doi.org/10.1016/S0377-0273(96)00063-7.

Orsi, G., Di Vito, M., Isaia, R., 2004. Volcanic hazard assessment at the restless Campi Flegrei caldera. Bull. Volcanol. 66, 514-530. https://doi.org/10.1007/s00445-003-0336-4.

OSHA, 2019. Carbon Dioxide Health Hazard Information Sheet. FSIS Environmental, Safety and Health Group. https://www.osha.gov/chemicaldata/chemResult.html?recNo=183.

Pataki, D.E., Ehleringer, J.R., Flanagan, L.B., Yakir, D., Bowling, D.R., Still, C.J., Buchmann, N., Kaplan, J.O., Berry, J.A., 2003. The application and interpretation of Keeling plots in terrestrial carbon cycle research. Global Biogeochem. Cycles 17 (1), 1022. https://doi.org/10.1029/2001GB001850.

Quay, P., King, S.L., Lansdown, J.M.,Wilbur, D.O., 1988. Isotopic composition of methane released from wetlands: implications for the increase in atmospheric methane. Glob. Biogeochem. Cycles 2 (4), 385–397. https://doi.org/10.1029/GB002i004p00385.

Quay, P., Stutsmann, J., Wilbur, D., Snover, A., Dlugokencky, E., Brown, T., 1999. The isotopic composition of atmospheric methane. Global Biogeochem. Cycles 13 (2), 445-461.

Queißer, M., Granieri, D., Burton, M., Arzilli, F., Avino, R., Carandente, A., 2017. Increasing CO_2 flux at Pisciarelli, Campi Flegrei, Italy. Solid Earth 8 (5), 1017-1024. https://doi.org/10.519/se-8-1017-2017.

R Core Team, 2017. R: A Language and Environment for Statistical Computing. https://www.R-project.org/.

Raible, C.C., Brönnimann, S., Auchmann, R., Brohan, P., Frölicher, T.L., Graf, H.F., Jones, P., Luterbacher, J., Muthers, S., Neukom, R., Robock, A., Self, S., Sudrajat, A., Timmreck, C., Wegmann, M., 2016. Tambora 1815 as a test case for high impact volcanic eruptions: Earth system effects. WIREs Clim. Change 7, 569-589. https://doi.org/10.1002/wcc.407.

686 Rampino, M.R., Self, S., 1982. Historic Eruptions of Tambora (1815), Krakatau (1883), and Agung
687 (1963), Their Stratospheric Aerosols, and Climatic Impact. Quat. Res. 18, 127-143.
688 https://doi.org/10.1016/0033-5894(82)90065-5.
689 Reikard, G., 2019. Volcanic emissions and air pollution: Forecasts from time series models. Atmosph.
690 Environ. 1, 100001. https://doi.org/10.1016/j.aeaoa.2018.100001.
691 Riebeek, H. and Simmon, R., 2011. The Carbon Cycle.
692 https://earthobservatory.nasa.gov/features/CarbonCycle.
693 Robock, A., 1981. The Mount St. Helens Volcanic Eruption of 18 May 1980: Minimal Climatic Effect.
694 Science 212, 1383-1384. https://doi.org/10.1126/science.212.4501.1383.
695 Robock, A., 2000. Volcanic eruptions and climate. Rev. Geoph. 38, 191-219.
696 https://doi.org/10.1029/1998RG000054.
697 Robock, A., 2004. Climatic Impact of Volcanic Emissions, in: Sparks, R.S.J., Hawkesworth, C.J. (Eds.),
698 State of the Planet: Frontiers and Challenges in Geophysics, AGU Geophysical Monograph Volume
699 150, pp. 125-134. https://doi.org/10.1029/150GM11.
700 Rubright, S.L.M., Pearce, L.L., Peterson, J., 2017. Environmental toxicology of hydrogen sulfide. Nitric
701 Oxide 71, 1-13. https://doi.org/10.1016/j.niox.2017.09.011.
702 Saunois, M., Stavert, A.R., Poulter, B., Bousquet, P., Canadell, J.G., Jackson, R.B., Raymond, P.A.,
703 Dlugokencky, E.J., Houweling, S., Patra, P.K., Ciais, P., Arora, V.K., Bastviken, D., Bergamaschi, P.,
704 Blake, D.R., Brailsford, G., Bruhwiler, L., Carlson, K.M., Carrol, M., Castaldi, S., Chandra, N.,
705 Crevoisier, C., Crill, P.M., Covey, K., Curry, C.L., Etiope, G., Frankenberg, C., Gedney, N., Hegglin,
706 M.I., Höglund-Isaksson, L., Hugelius, G., Ishizawa, M., Ito, A., Janssens-Maenhout, G., Jensen, K.M.,
707 Joos, F., Kleinen, T., Krummel, P.B., Langenfelds, R.L., Laruelle, G.G., Liu, L., Machida, T.,
708 Maksyutov, S., McDonald, K.C., McNorton, J., Miller, P.A., Melton, J.R., Morino, I., Müller, J.,
709 Murguia-Flores, F., Naik, V., Niwa, Y., Noce, S., O'Doherty, S., Parker, R.J., Peng, C., Peng, S., Peters,
710 G.P., Prigent, C., Prinn, R., Ramonet, M., Regnier, P., Riley, W.J., Rosentreter, J.A., Segers, A.,
711 Simpson, I.J., Shi, H., Smith, S.J., Steele, L.P., Thornton, B.F., Tian, H., Tohjima, Y., Tubiello, F.N.,
712 Tsuruta, A., Viovy, N., Voulgarakis, A., Weber, T.S., van Weele, M., van der Werf, G.R., Weiss, R.F.,
713 Worthy, D., Wunch, D., Yin, Y., Yoshida, Y., Zhang, W., Zhang, Z., Zhao, Y., Zheng, B., Zhu, Q., Zhu,

714 Q., Zhuang, Q., 2019. The Global Methane Budget 2000-2017. Earth System Science Data. doi:
715 10.5194/essd-2019-128.
716 Schwietzke, S., Sherwood, O.A., Bruhwiler, L.M.P., Miller, J.B., Etiope, G., Dlugokencky, E.J.,
717 Englund Michel, S., Arling, V.A., Vaughn, B.H., White, J.W.C., Tans, P.P., 2016. Upward revision of
718 global fossil fuel methane emissions based on isotope database. Nature 538, 88–91.
719 https://doi.org/10.1038/nature19797.
720 Self, S., Zhao, J.X., Holasek, R.E., Torres, R.C., King, A.J., 1993. The Atmospheric Impact of the 1991
721 Mount Pinatubo Eruption. NASA/CR93-207274.
722 Self, S., Gertisser, R., Thordarson, T., Rampino, M.R., Wolff, J.A., 2004. Magma volume, volatile
723 emissions, and stratospheric aerosols from the 1815 eruption of Tambora. Geophys. Res. Lett. 31,
724 L20608. https://doi.org/10.1029/2004GL020925.
725 Self, S., 2005. Effects of volcanic eruptions on the atmosphere and climate, in: Martí, J., Ernst, G.G.J.
726 (Eds.), Volcanoes and the Environment. Cambridge University Press, pp. 152-174.
727 Self S., 2006. The effects and consequences of very large explosive volcanic eruptions. Philos. Trans.
728 R. Soc. A 364, 2073-2097. https://doi.org/10.1098/rsta.2006.1814.
729 Sherwood, O.A., Schwietzke, S., Arling, V.A., Etiope, G., 2017. Global inventory of gas geochemistry
730 data from fossil fuel, microbial and burning sources, version 2017. Earth System Science Data 9, 639–
731 656. https://doi.org/10.5194/essd-9-639-2017.
732 Tamburello, G., Caliro, S., Chiodini, G., De Martino, P., Avino, R., Minopoli, C., Carandente, A.,
733 Rouwet, D., Aiuppa, A., Costa, A., Bitetto, M., Giudice, G., Francofonte, V., Ricci, T., Sciarra, A.,
734 Bagnato, E., Capecchiacci, F., 2019. Escalating CO_2 degassing at the Pisciarelli fumarolic system, and
735 implications for the ongoing Campi Flegrei unrest. J. Volcanol. Geotherm. Res. 384, 151-157.
736 https://doi.org/10.1016/j.jvolgeores.2019.07.005.
737 Tassi, F., Vaselli, O., Cuccoli, F., Buccianti, A., Nisi, B., Lognoli, E., Montegrossi, G., 2009. A
738 geochemical multi-methodological approach in hazard assessment of CO_2-rich gas emissions at Mt.
739 Amiata volcano (Tuscany, central Italy). Water, Air, Soil Pollution Focus 9, 117-127.
740 https://doi.org/10.1007/s11267-008-9198-2.

741 Tassi, F., Nisi, B., Cardellini, C., Capecchiacci, F., Donnini, M., Vaselli, O., Avino, R., Chiodini, G.,
742 2013. Diffuse soil emission of hydrothermal gases (CO_2, CH_4, and C_6H_6) at Solfatara crater (Campi
743 Flegrei, southern Italy). Appl. Geochem. 35, 142-153.
744 https://doi.org/10.1016/j.apgeochem.2013.03.020.
745 Tassi, F., Venturi, S., Cabassi, J., Capecchiacci, F., Nisi, B., Vaselli, O., 2015. Volatile organic
746 compounds (VOCs) in soil gases from Solfatara crater (Campi Flegrei, southern Italy): Geogenic
747 source(s) vs. biogeochemical processes. Appl. Geochem. 56, 37-49.
748 https://doi.org/10.1016/j.apgeochem.2015.02.005.
749 Textor, C., Graf, H.F., Herzog, M., Oberhuber, J.M., 2003. Injection of gases into the stratosphere by
750 explosive volcanic eruptions. J. Geophys. Res. 108, 4606. https://doi.org/10.1029/2002JD002987.
751 Thermo Fisher Scientific Inc, 2012. Thermo Scientific model 450*i* hydrogen sulfide & sulfur dioxide
752 analyzer manual.
753 https://www.thermofisher.com/content/dam/tfs/ATG/EPD/EPD%20Documents/Product%20Manuals
754 %20&%20Specifications/Air%20Quality%20Instruments%20and%20Systems/Ambient%20Gas/D197
755 31~.pdf.
756 Thorsteinsson, T., Hackenbruch, J., Sveinbjörnsson, E., Jóhannsson, T., 2013. Statistical assessment and
757 modeling of the effects of weather conditions on H_2S plume dispersal from Icelandic geothermal power
758 plants. Geothermics 45, 31-40.
759 Townsend-Small, A., Tyler, S.C., Pataki, D.E., Xu, X., Christensen, L.E., 2012. Isotopic measurements
760 of atmospheric methane in Los Angeles, California, USA: influence of “fugitive” fossil fuel emissions.
761 J. Geophys. Res. 117, D07308. https://doi.org/10.1029/2011JD016826.
762 Vaselli, O., Nisi, B., Tassi, F., Rappuoli, D., Pancioli, V., Ucciero, S., Giannini, L., 2011. CO_2 hazard
763 vs touristic attraction at the Mt. Amiata Volcano (Italy). Acta Vulcanol. 23 (1-2), 73-80.
764 Venturi, S., Cabassi, J., Tassi, F., Capecchiacci, F., Vaselli, O., Bellomo, S., Calabrese, S.,
765 D’Alessandro, W., 2016. Hydrogen sulfide measurements in air by passive/diffusive samplers and high-
766 frequency analyzer: A critical comparison. App. Geochem. 72, 51-58.
767 https://doi.org/10.1016/j.apgeochem.2016.07.001.

Venturi, S., Tassi, F., Cabassi, J., Vaselli, O., Minardi, I., Neri, S., Caponi, C., Capasso, G., Di Martino, R.M.R., Ricci, A., Capecchiacci, F., Lelli, M., Sciarra, A., Cinti, D., Virgili, G., 2019. A multi-instrumental geochemical approach to assess the environmental impact of CO_2-rich gas emissions in a densely populated area: The case of Cava dei Selci (Latium, Italy). App. Geochem. 101, 109-126. https://doi.org/10.1016/j.apgeochem.2019.01.003.

Venturi, S., Tassi, F., Cabassi, J., Gioli, B., Baronti, S., Vaselli, O., Caponi, C., Vagnoli, C., Picchi, G., Zaldei, A., Magi, F., Miglietta, F., Capecchiacci, F., 2020. Seasonal and diurnal variations of greenhouse gases in Florence (Italy): Inferring sources and sinks from carbon isotopic ratios. STOTEN 698, 134245. https://doi.org/10.1016/j.scitotenv.2019.134245.

Venturi, S., Cabassi, J., Tassi, F., Maioli, G., Randazzo, A., Capecchiacci, F., Vaselli, O., 2021. Near-surface atmospheric concentrations of greenhouse gases (CO_2 and CH_4) in Florence urban area: Inferring emitting sources through carbon isotopic analysis. Urban Climate 39, 100968. https://doi.org/10.1016/j.uclim.2021.100968.

Vilardo, G., Alessio, G., Luongo, G., 1991. Analysis of the Magnitude-Frequency Distribution for the 1983– 1984 Earthquake Activity of Campi Flegrei, Italy. J. Volcanol. Geotherm. Res. 48(1–2), 115–125. https://doi.org/10.1016/0377-0273(91)90037-Z.

Viveiros, F., Cardellini, C., Ferreira, T., Caliro, S., Chiodini, G., Silva, C., 2010. Soil CO_2 emissions at Furnas Volcano, São Miguel Island, Azores archipelago: volcano monitoring perspectives, geomorphologic studies, and land use planning application. J. Geophys. Res. 115 (B12208). https://doi.org/10.1029/2010JB007555.

von Glasow, R., Bobrowski, N., Kern, C., 2009. The effects of volcanic eruptions on atmospheric chemistry. Chem. Geol. 263, 131-142. https://doi.org/10.1016/j.chemgeo.2008.08.020.

WHO, 1981. Hydrogen sulfide. Environmental Health Criteria, 19. World Health Organization, Geneva, Switzerland. http://www.inchem.org/documents/ehc/ehc/ehc019.htm.

WHO, 2000a. Hydrogen sulfide. Air Quality Guidelines for Europe - Second Edition. © WHO Regional Office for Europe, Copenhagen, Denmark. https://www.euro.who.int/__data/assets/pdf_file/0005/74732/E71922.pdf.

WHO, 200b. Sulfur dioxide. Air Quality Guidelines for Europe - Second Edition. © WHO Regional Office for Europe, Copenhagen, Denmark. https://www.euro.who.int/__data/assets/pdf_file/0020/123086/AQG2ndEd_7_4Sulfurdioxide.pdf.

WHO, 2003. Hydrogen sulfide: human health aspects. Concise International Chemical Assessment Document 53. World Health Organization, Geneva, Switzerland. https://www.who.int/ipcs/publications/cicad/en/cicad53.pdf.

WHO, 2018. Ambient (outdoor) air pollution. https://www.who.int/news-room/fact-sheets/detail/ambient-(outdoor)-airquality-and-health.

Zazzeri, G., Lowry, D., Fisher, R.E., France, J.L., Lanoisellé, M., Grimmond, C.S.B., Nisbet, E.G., 2017. Evaluating methane inventories by isotopic analysis in the London region. Sci. Rep. 7, 4854. https://doi.org/10.1038/s41598-017-04802-6.

807 Figure 1. (a) Satellite image of Campi Flegrei area, with location of Solfatara crater and Pisciarelli
808 hydrothermal fields. (b) Location of measuring sites (red dots) and hydrothermal discharges (orange
809 stars).
810
811 Figure 2. (a) H_2S/CO_2 vs. H_2S binary diagram of FU (blue dots), GW (magenta dots), and AC (yellow
812 and orange dots) sites. Hydrothemal discharges of Pisciarelli fumaroles (blue star) and the geothermal
813 well (magenta stars) are also reported. The mixing lines between (i) hydrothermal components, and (ii)
814 air, are shown as dashed lines. (b) CO_2 vs. H_2S binary diagram of FU (blue dots), GW (magenta dots),
815 and AC (yellow and orange dots) sites. The mixing lines between (i) hydrothermal components, and (ii)
816 air, are reported as abovementioned. The black arrows show trends of (i) enrichment in CO_2 (Trend A),
817 and (ii) depletion in H_2S (Trend B).
818
819 Figure 3. Keeling plot of $\delta^{13}C\text{-}CO_2$ vs. $1/CO_2$ of (a) FU, (b) GW, and (c) AC. The mixing between (i)
820 hydrothemal discharges, and (ii) local background, is depicted with the grey area. The isotopic ranges
821 of hydrothemal and background end-members are also reported (black lines).
822
823 Figure 4. (a) H_2S vs. CH_4 binary diagram of FU (blue dots), AC (yellow and orange dots), GW (magenta
824 dots), HT (light and dark green dots), and DS (turquoise dots). (b) Keeling plot of $\delta^{13}C\text{-}CH_4$ vs. $1/CH_4$
825 of HT during 21st-22nd January 2020 nighttime measurements. The data are divided into night data (0:00-
826 5:59; olive green dots) and morning data (6:00-end of measurements; light green dots). (c) Keeling plot
827 of $\delta^{13}C\text{-}CH_4$ vs. $1/CH_4$ of HT during 22nd-23rd January 2020 nighttime measurements. The data are
828 divided into night data (0:00-5:59; teal green dots) and morning data (6:00-end of measurements; dark
829 green dots). (d) Keeling plot of $\delta^{13}C\text{-}CH_4$ vs. $1/CH_4$ of DS (turquoise dots). In (b), (c) and (d), the mixing
830 trends between (i) air background and urban emissions, and (ii) air background and biogenic emissions,
831 are reported (black dashed lines).
832
833 Figure 5. Keeling plot of $\delta^{13}C\text{-}CO_2$ vs. $1/CO_2$ of FU (blue dots), AC (yellow and orange dots), GW
834 (magenta dots), HT (light and dark green dots), and DS (turquoise dots). The isotopic ranges of

hydrothemal, background and anthropogenic end-members are reported (black lines). The mixing between (i) hydrothemal discharges and local background, and (ii) anthropogenic emissions and local background, are depicted with the grey areas. The shift of a branch of HT data toward the DS site field is marked with the black dashed arrow.

Figure 6. SO_2 vs. H_2S binary diagram of FU (blue dots), AC (yellow and orange dots), GW (magenta dots), HT (light and dark green dots), and DS (turquoise dots).

Table 1. Summary descriptive statistical parameters on the minute-averaged data measured at each site, and meteorological parameters (WD=wind direction, WS=wind speed).

Chemical compositions of CO_2 and CH_4 are in mg/m^3; chemical compositions of H_2S and SO_2 are in $\mu g/m^3$; $\delta^{13}C\text{-}CO_2$ and $\delta^{13}C\text{-}CH_4$ are in ‰ vs. V-PDB; WS (minimum-maximum) are in km/h.

Table 2. $\delta^{13}C\text{-}CO_2$ and $\delta^{13}C\text{-}CH_4$ (‰ vs. V-PDB) source values extrapoleted using the Keeling plot analysis. Standard errors and determination coefficients R^2 are also reported.

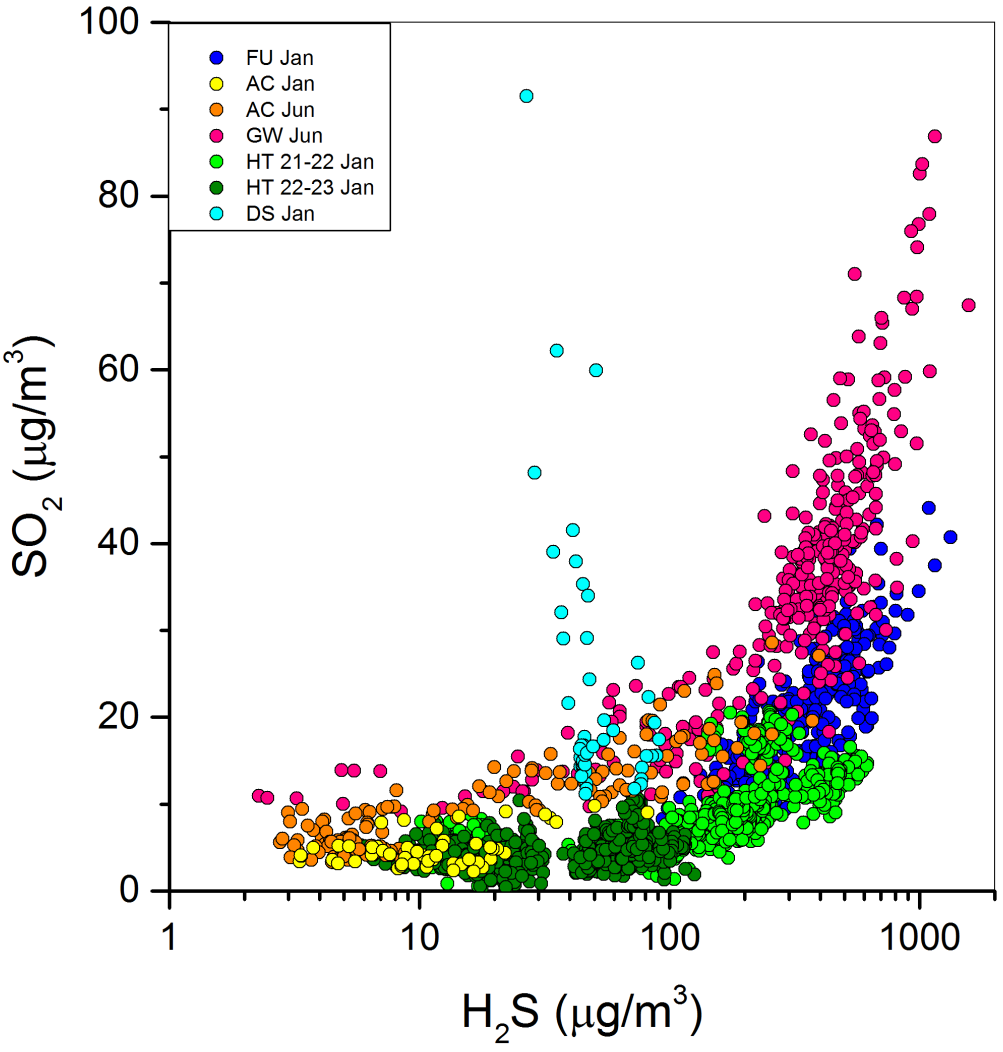
FU Jan
AC Jan
AC Jun
GW Jun
HT 21-22 Jan
HT 22-23 Jan
DS Jan
100
80
60
40
20
0
1
10
100
1000
SO2 (µg/m3)
H2S (µg/m3)

850

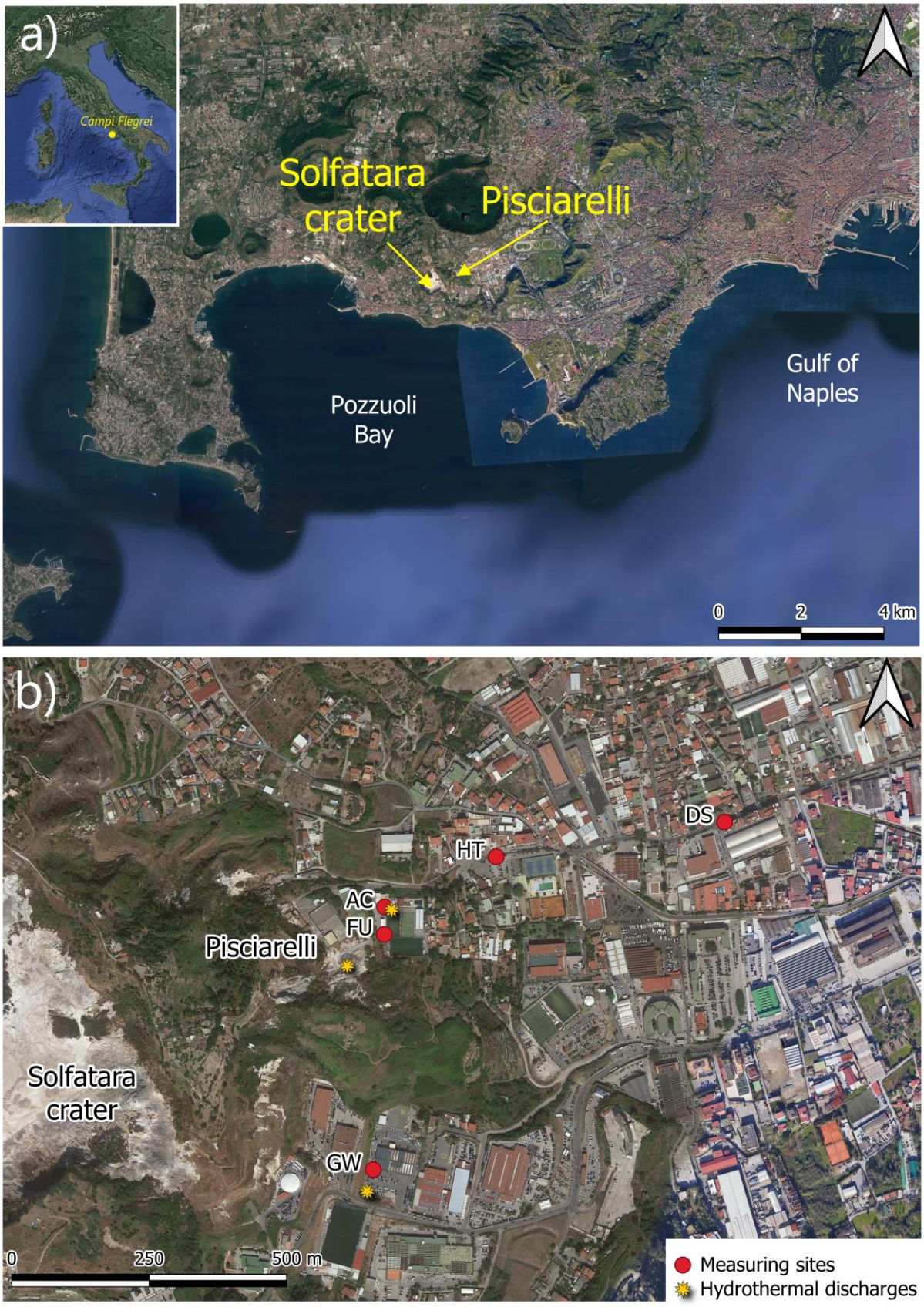
a)
Campi Flegrei
Solfatara
crater
Pisciarelli
Pozzuoli
Bay
Gulf of
Naples
0
2
4 km
b)
DS
HT
AC
FU
Pisciarelli
Solfatara
crater
GW
0
250
500 m
Measuring sites
Hydrothermal discharges

851

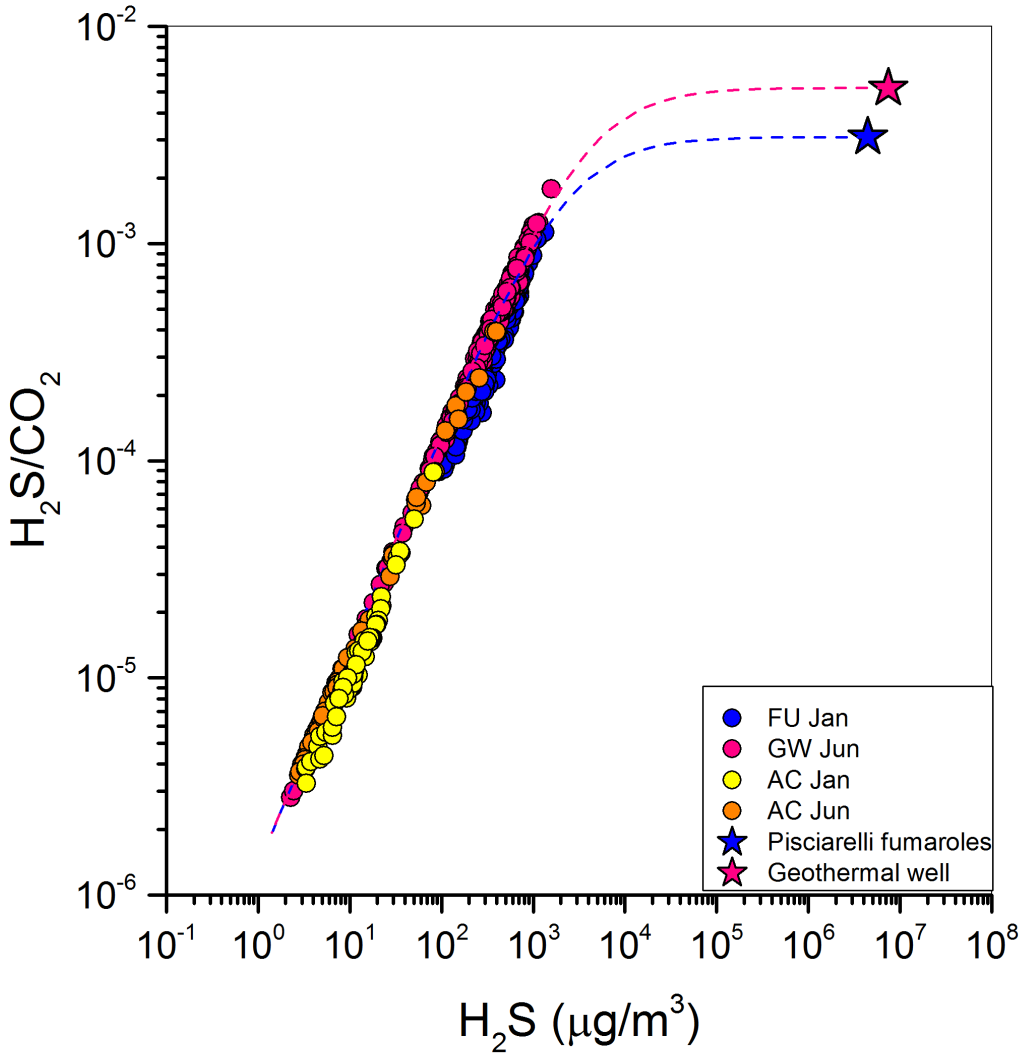
10^{-2}
10^{-3}
10^{-4}
10^{-5}
10^{-6}
H_2S/CO_2
10^{-1} 10^{0} 10^{1} 10^{2} 10^{3} 10^{4} 10^{5} 10^{6} 10^{7} 10^{8}
H_2S (μg/m^3)
FU Jan
GW Jun
AC Jan
AC Jun
Pisciarelli fumaroles
Geothermal well

852

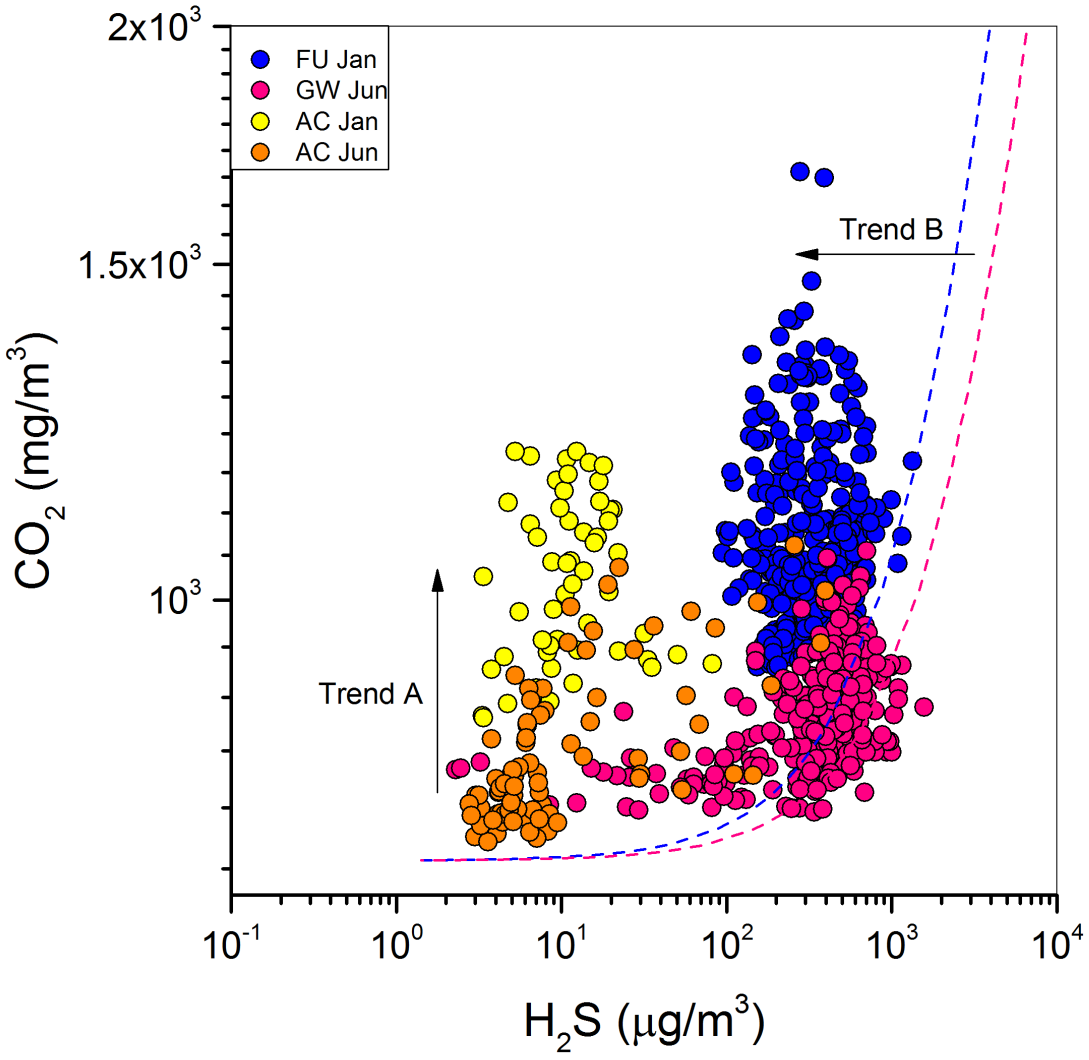
2x10^3
1.5x10^3
10^3
CO2 (mg/m^3)
FU Jan
GW Jun
AC Jan
AC Jun
Trend A
Trend B
10^-1
10^0
10^1
10^2
10^3
10^4
H2S (µg/m^3)

853

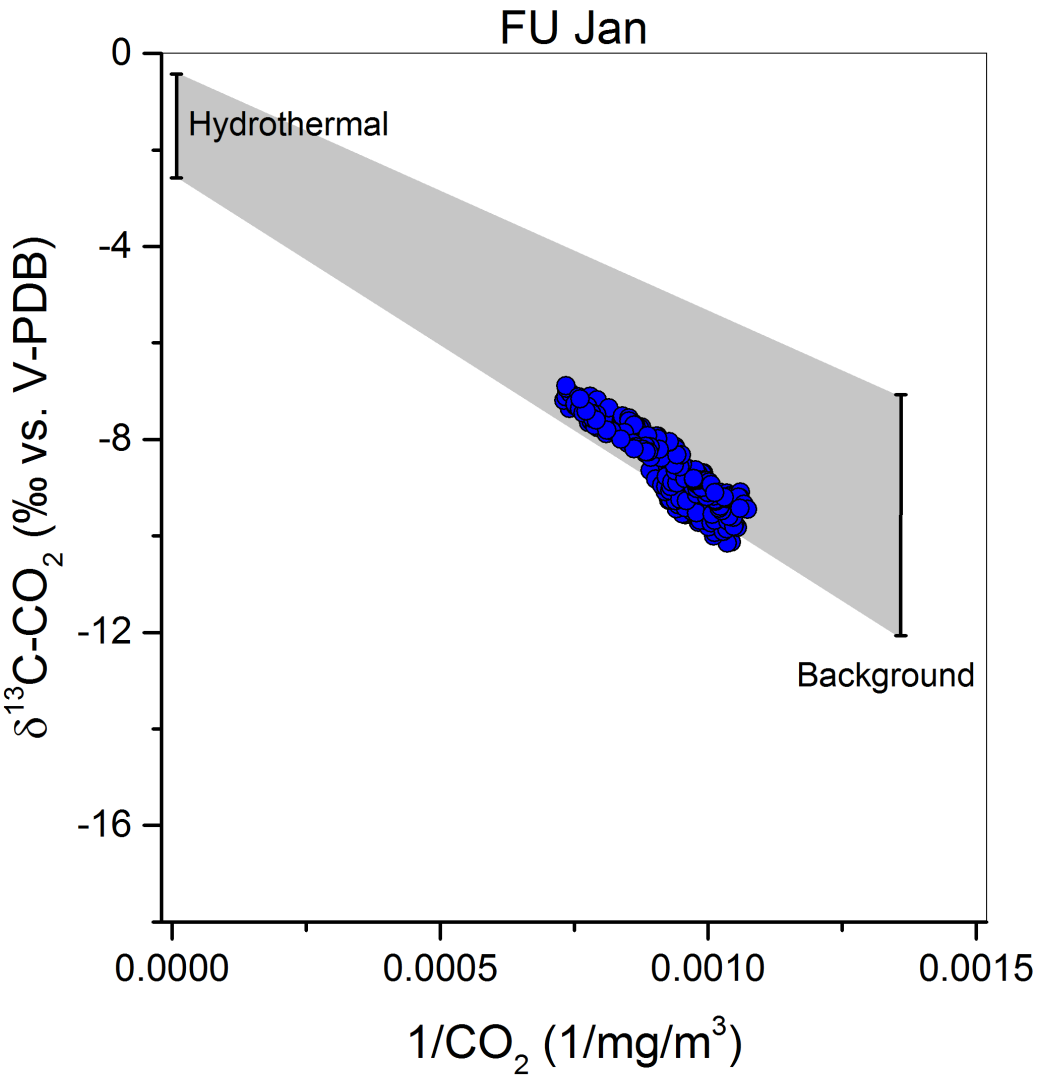
FU Jan
Hydrothermal
Background
0
-4
-8
-12
-16
0.0000
0.0005
0.0010
0.0015
δ13C-CO2 (‰ vs. V-PDB)
1/CO2 (1/mg/m3)

854

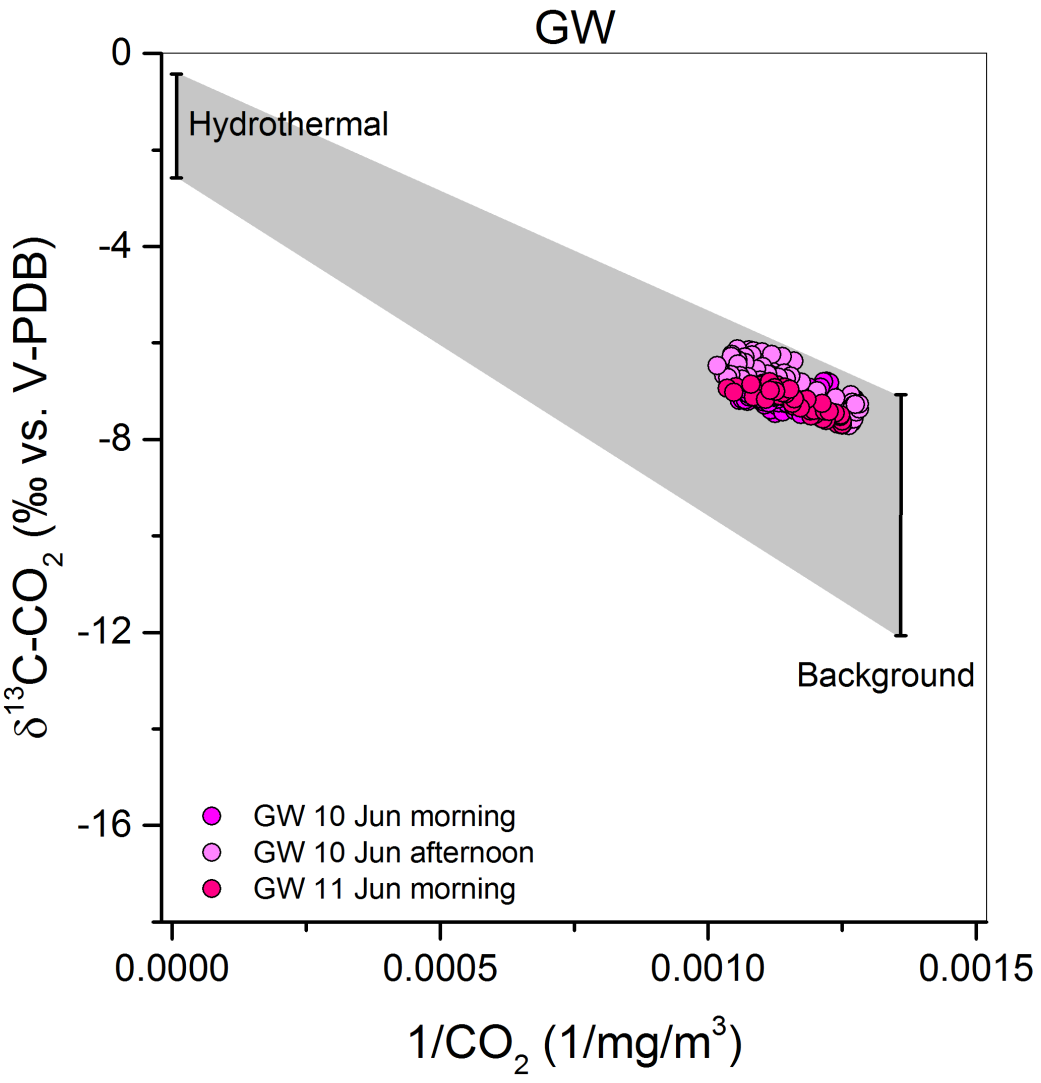
GW
Hydrothermal
Background
GW 10 Jun morning
GW 10 Jun afternoon
GW 11 Jun morning
0
-4
-8
-12
-16
0.0000
0.0005
0.0010
0.0015
δ13C-CO2 (‰ vs. V-PDB)
1/CO2 (1/mg/m3)

855

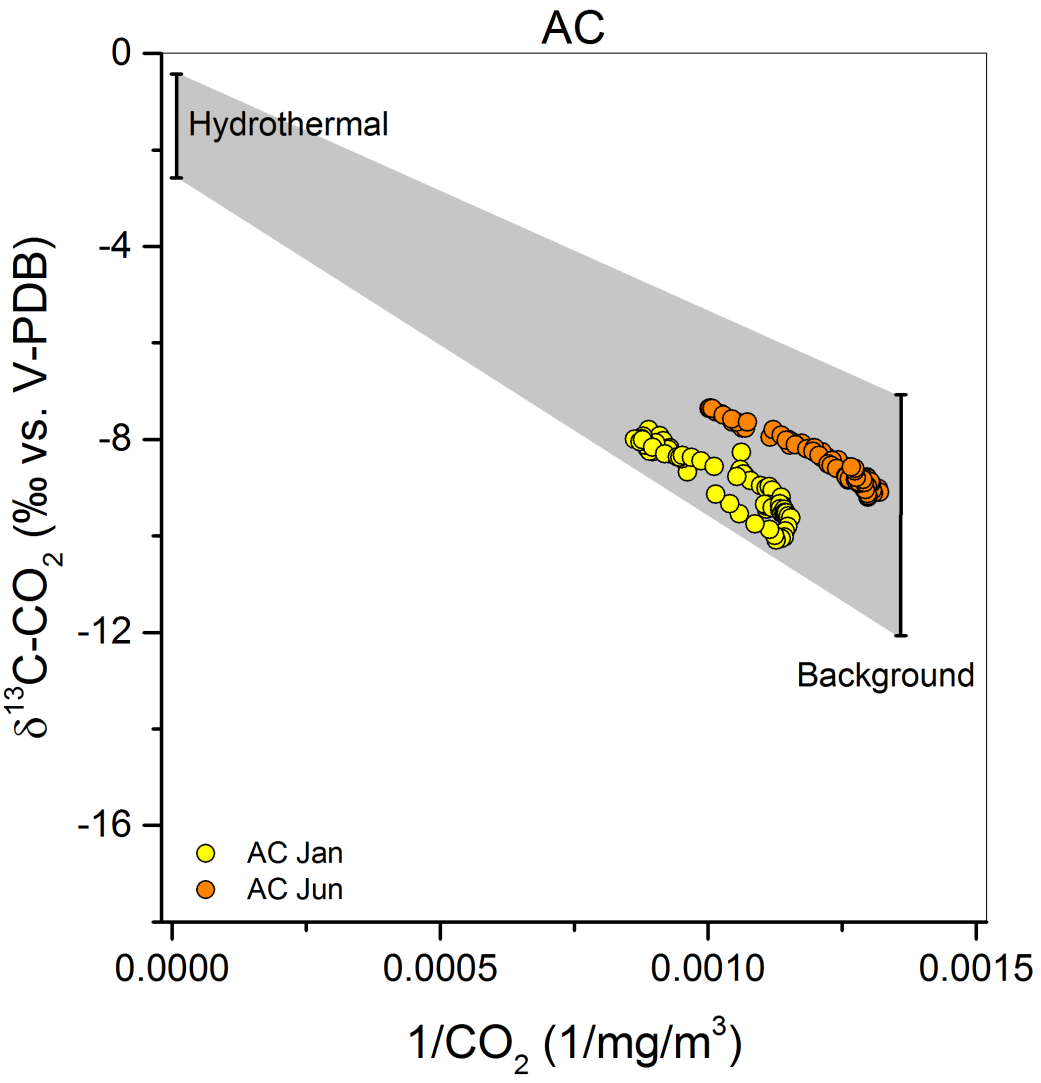
AC
Hydrothermal
Background
AC Jan
AC Jun
0
-4
-8
-12
-16
0.0000
0.0005
0.0010
0.0015
δ13C-CO2 (‰ vs. V-PDB)
1/CO2 (1/mg/m3)

856

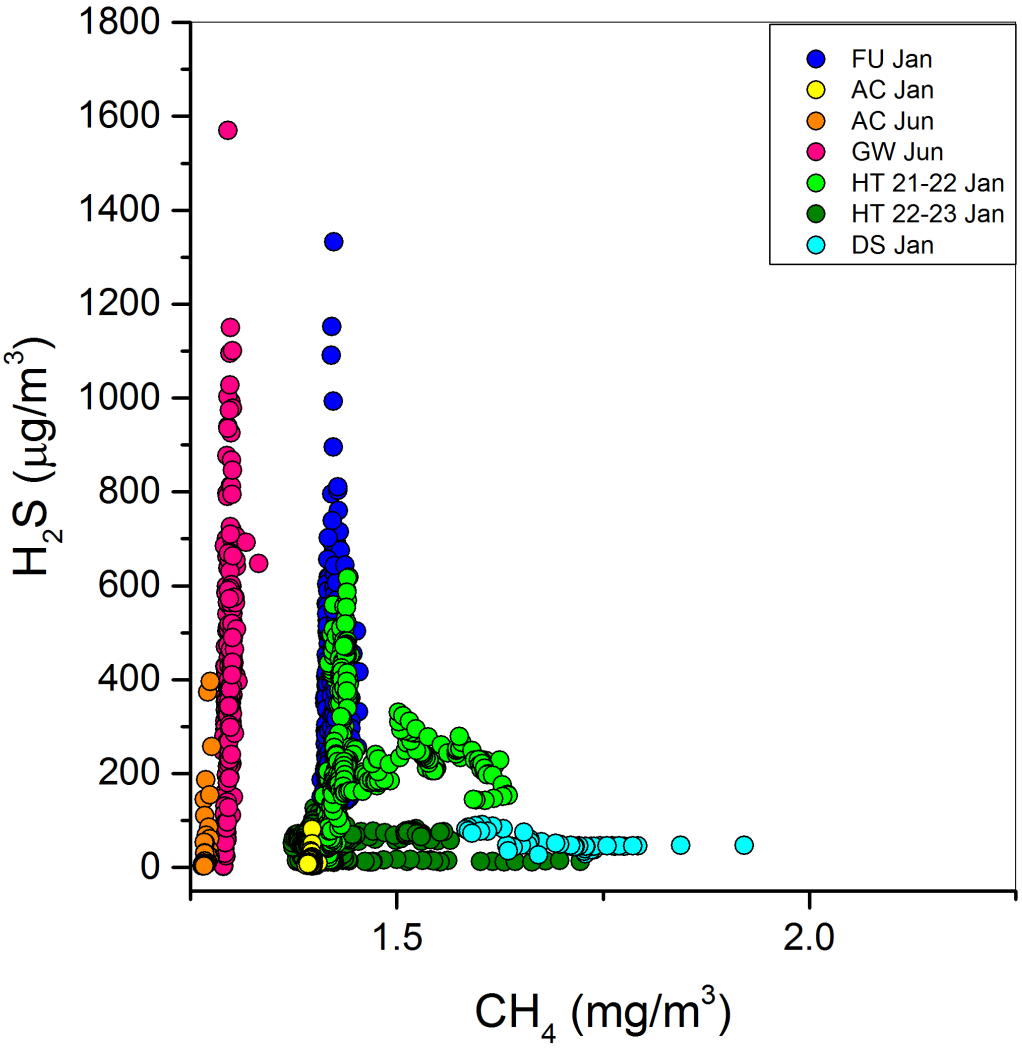
1800
1600
1400
1200
1000
800
600
400
200
0
1.5
2.0
H2S (µg/m3)
CH4 (mg/m3)
FU Jan
AC Jan
AC Jun
GW Jun
HT 21-22 Jan
HT 22-23 Jan
DS Jan

857

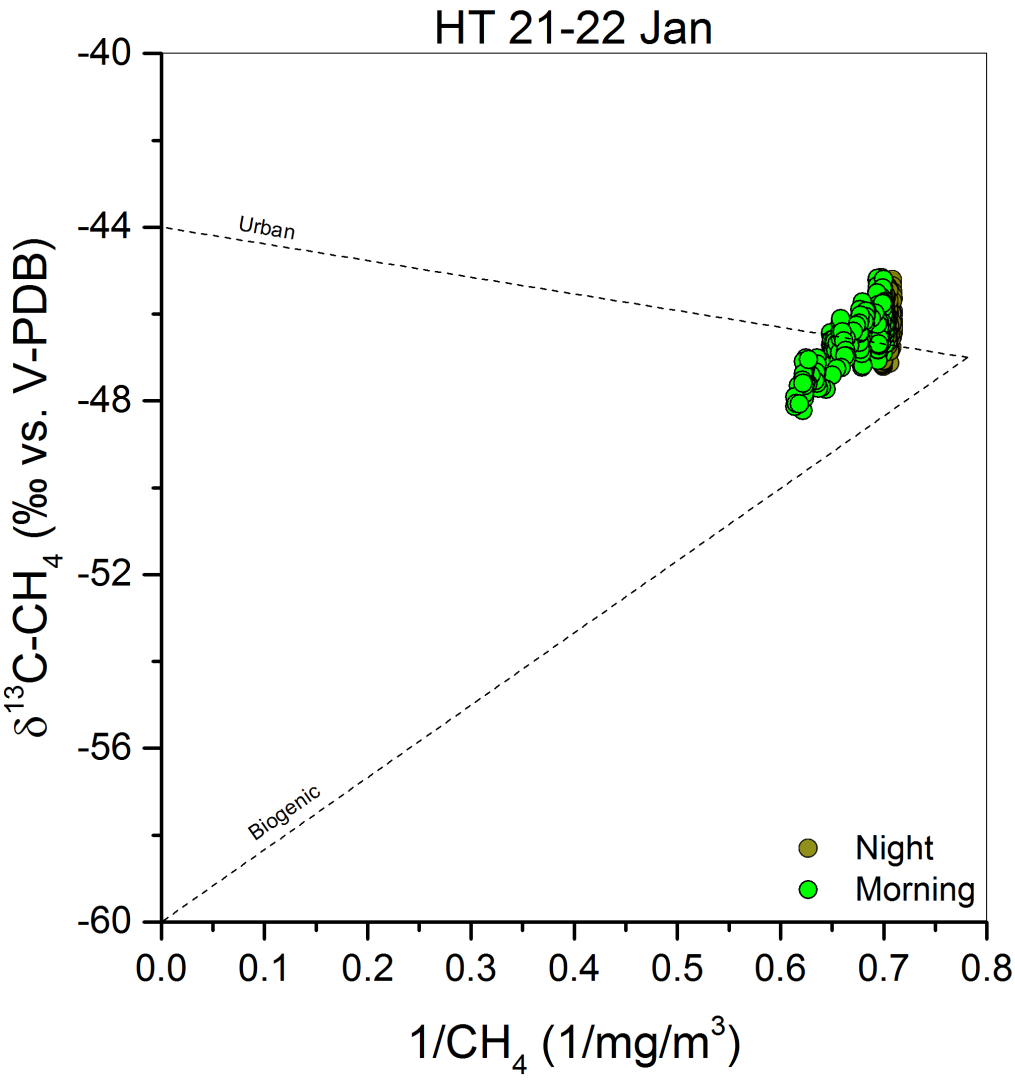
HT 21-22 Jan
-40
-44
-48
-52
-56
-60
Urban
Biogenic
Night
Morning
0.0
0.1
0.2
0.3
0.4
0.5
0.6
0.7
0.8
δ13C-CH4 (‰ vs. V-PDB)
1/CH4 (1/mg/m3)

858

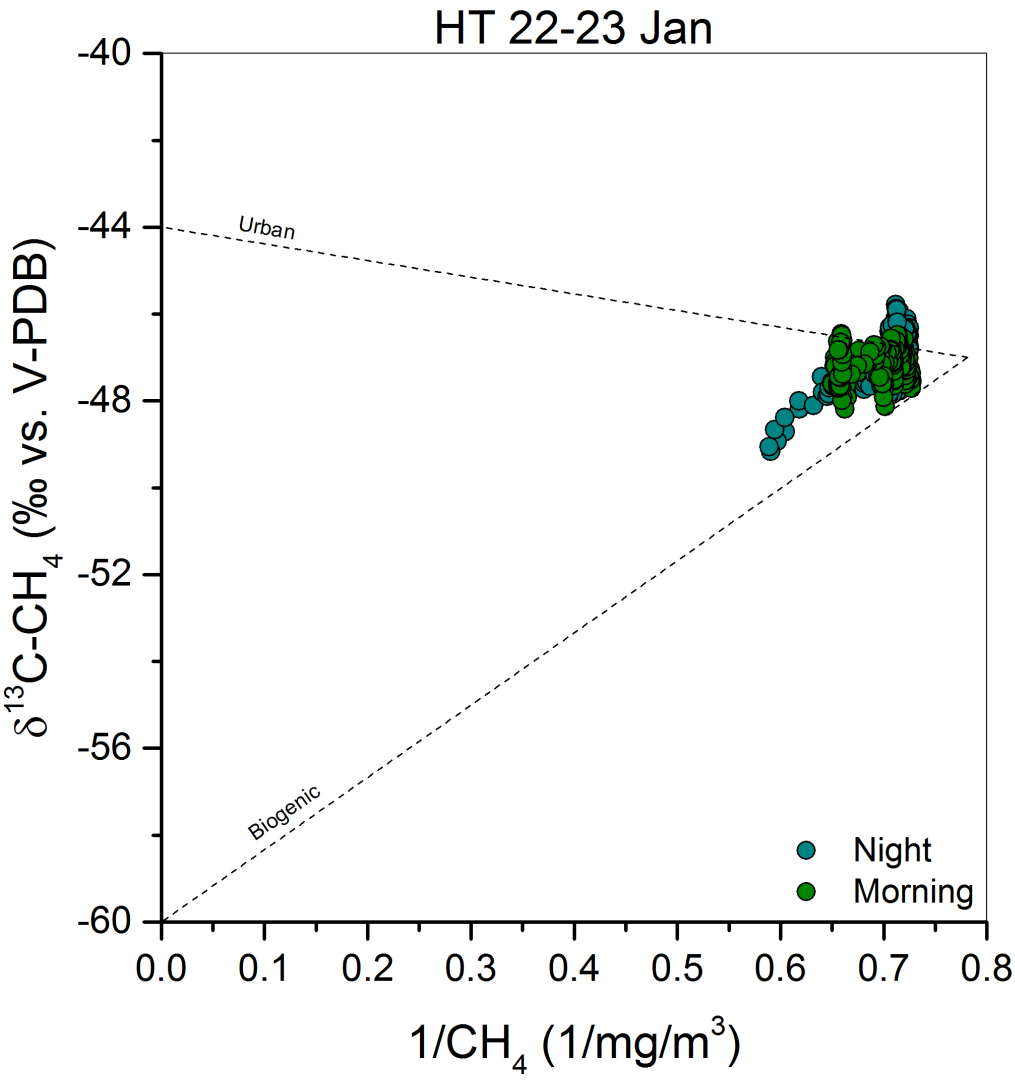
HT 22-23 Jan
-40
-44
-48
-52
-56
-60
Urban
Biogenic
Night
Morning
0.0
0.1
0.2
0.3
0.4
0.5
0.6
0.7
0.8
δ13C-CH4 (‰ vs. V-PDB)
1/CH4 (1/mg/m3)

859

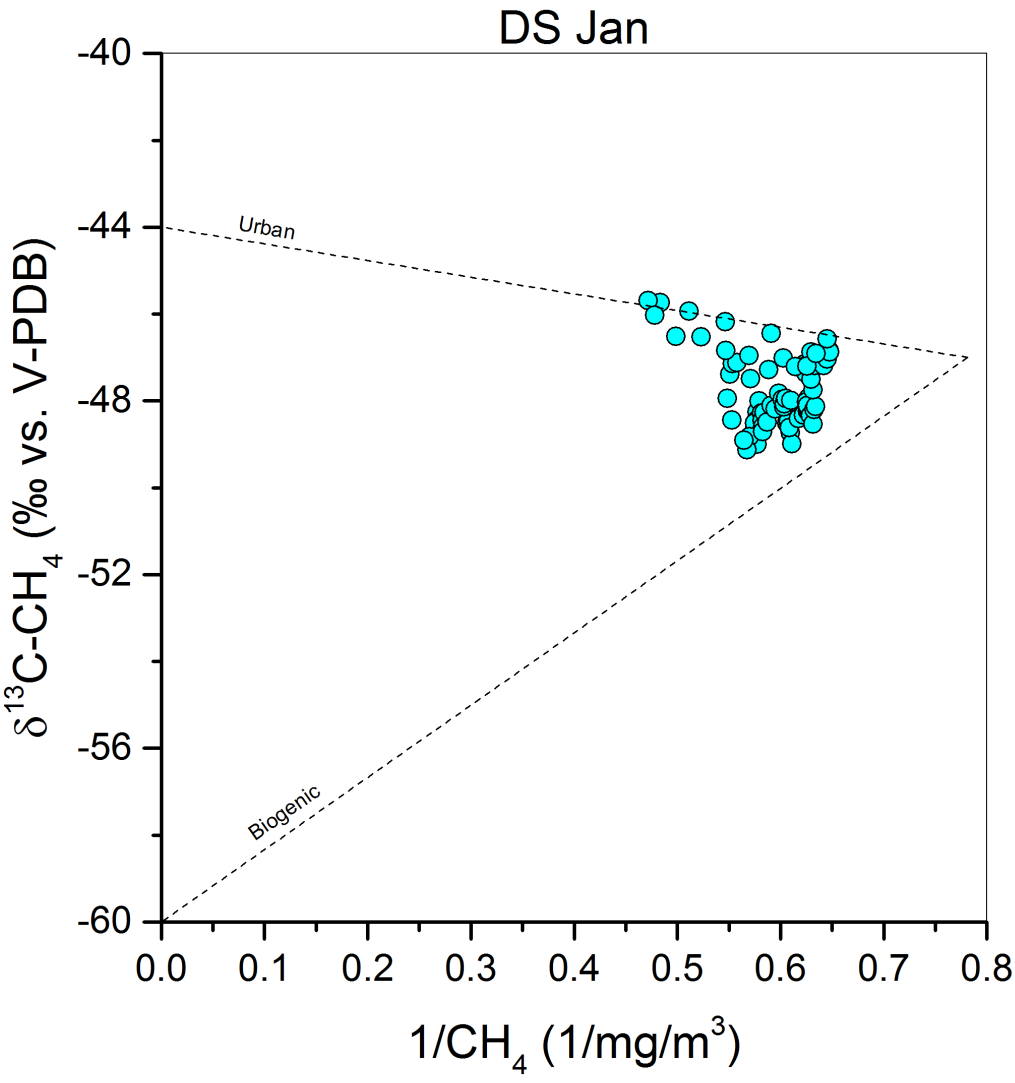
DS Jan
-40
-44
-48
-52
-56
-60
Urban
Biogenic
0.0
0.1
0.2
0.3
0.4
0.5
0.6
0.7
0.8
δ13C-CH4 (‰ vs. V-PDB)
1/CH4 (1/mg/m3)

860

861

862 AppendixA

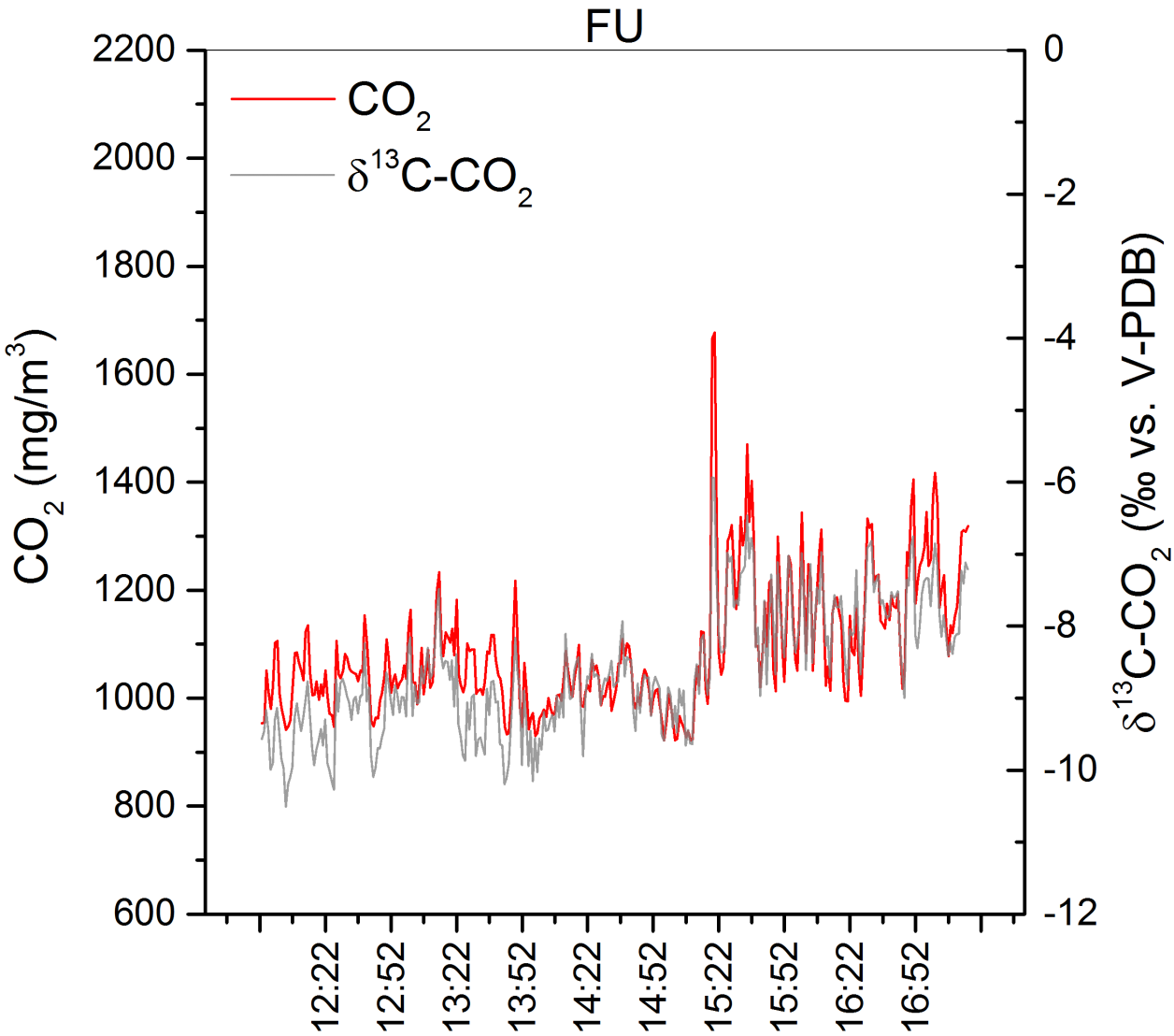

863
864 Figure A.1. CO_2 concentrations (mg/m^3; red line) and $\delta^{13}C$-CO_2 values (‰ vs. V-PDB; grey line) vs.
865 time of FU site on 22nd January 2020.

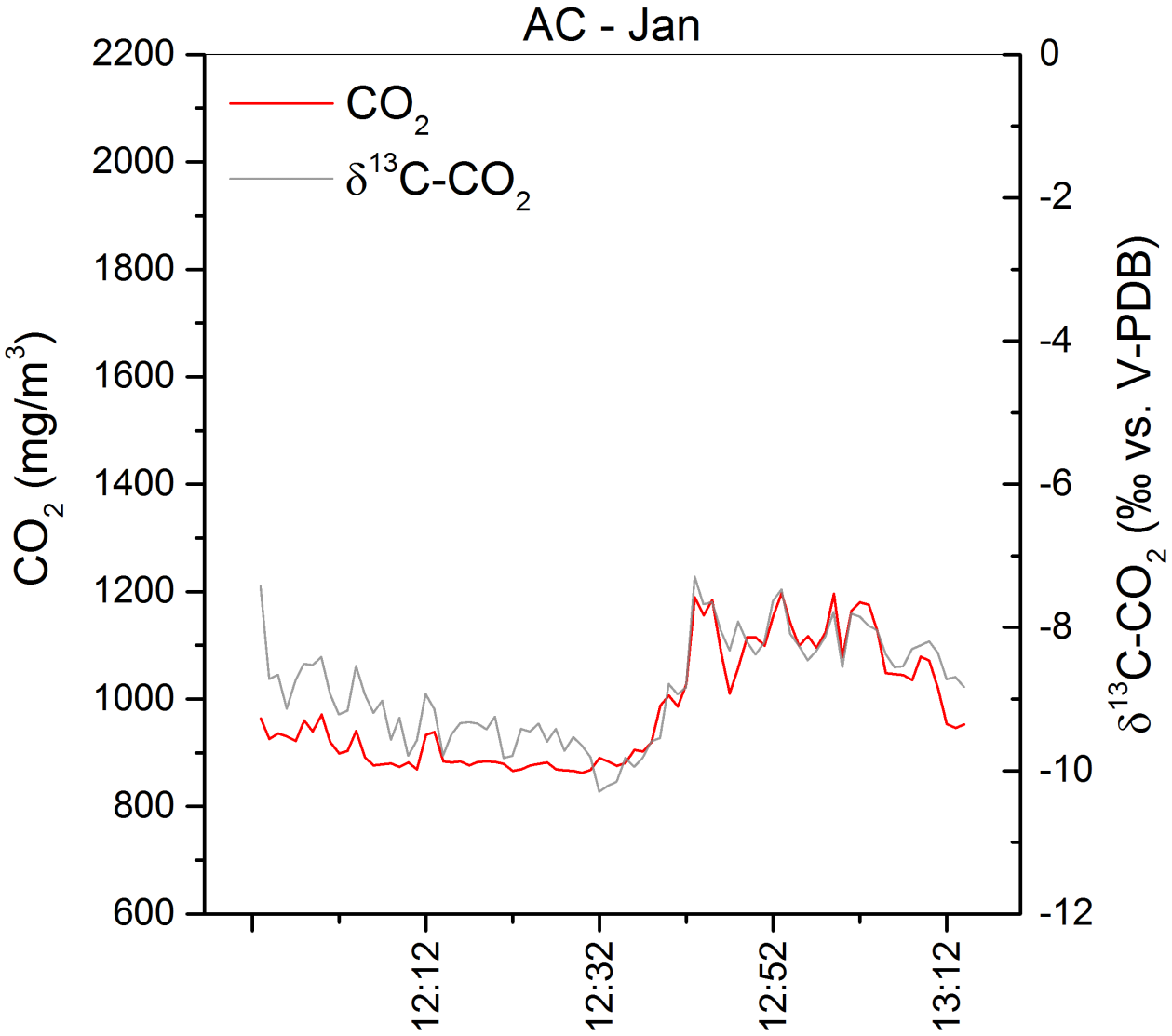

Figure A.2. CO_2 concentrations (mg/m^3; red line) and $\delta^{13}C$-CO_2 values (‰ vs. V-PDB; grey line) vs. time of AC site on 21st January 2020.

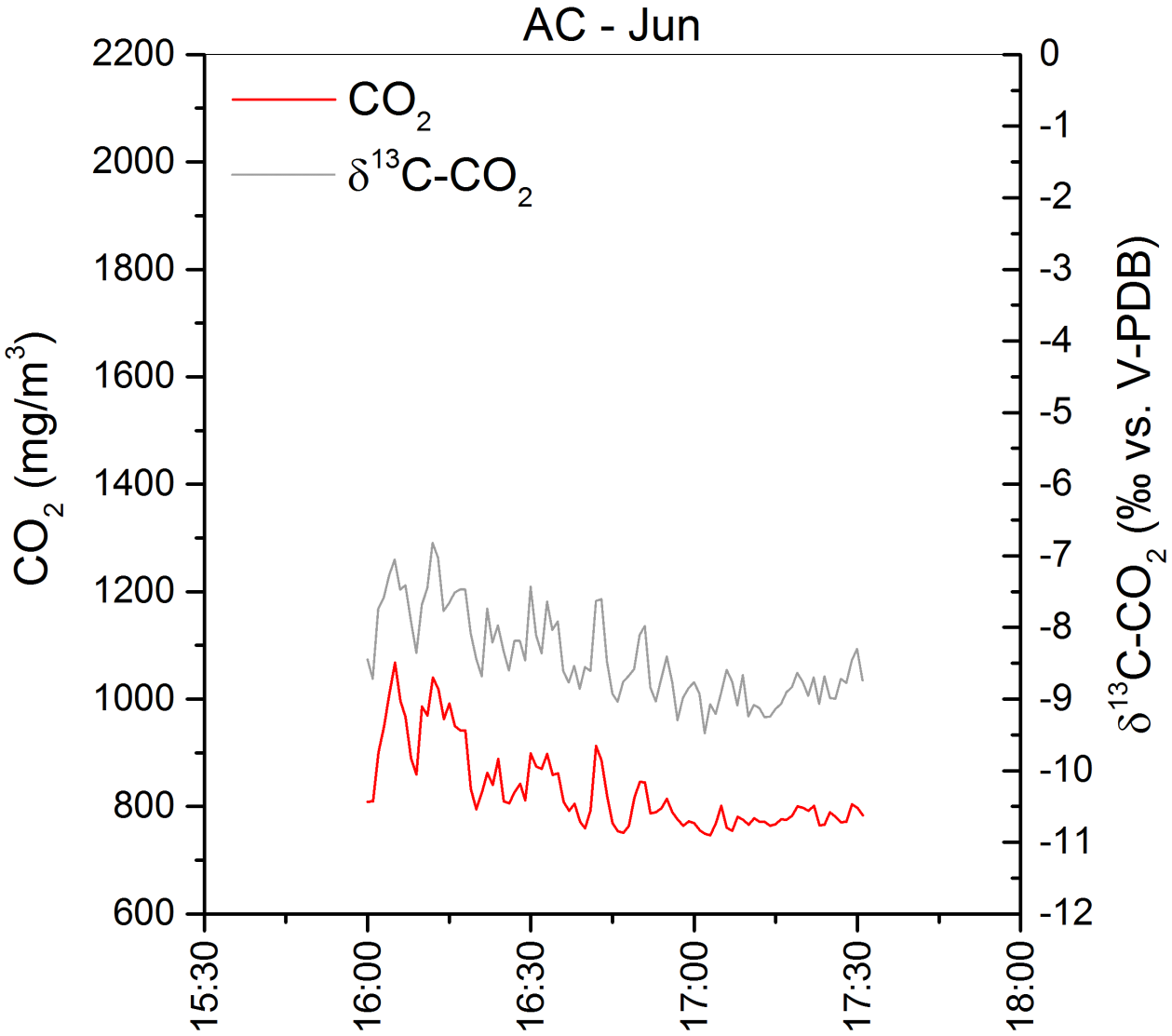

870
871 Figure A.3. CO_2 concentrations (mg/m^3; red line) and $\delta^{13}C$-CO_2 values (‰ vs. V-PDB; grey line) vs.
872 time of AC site on 9th June 2020.

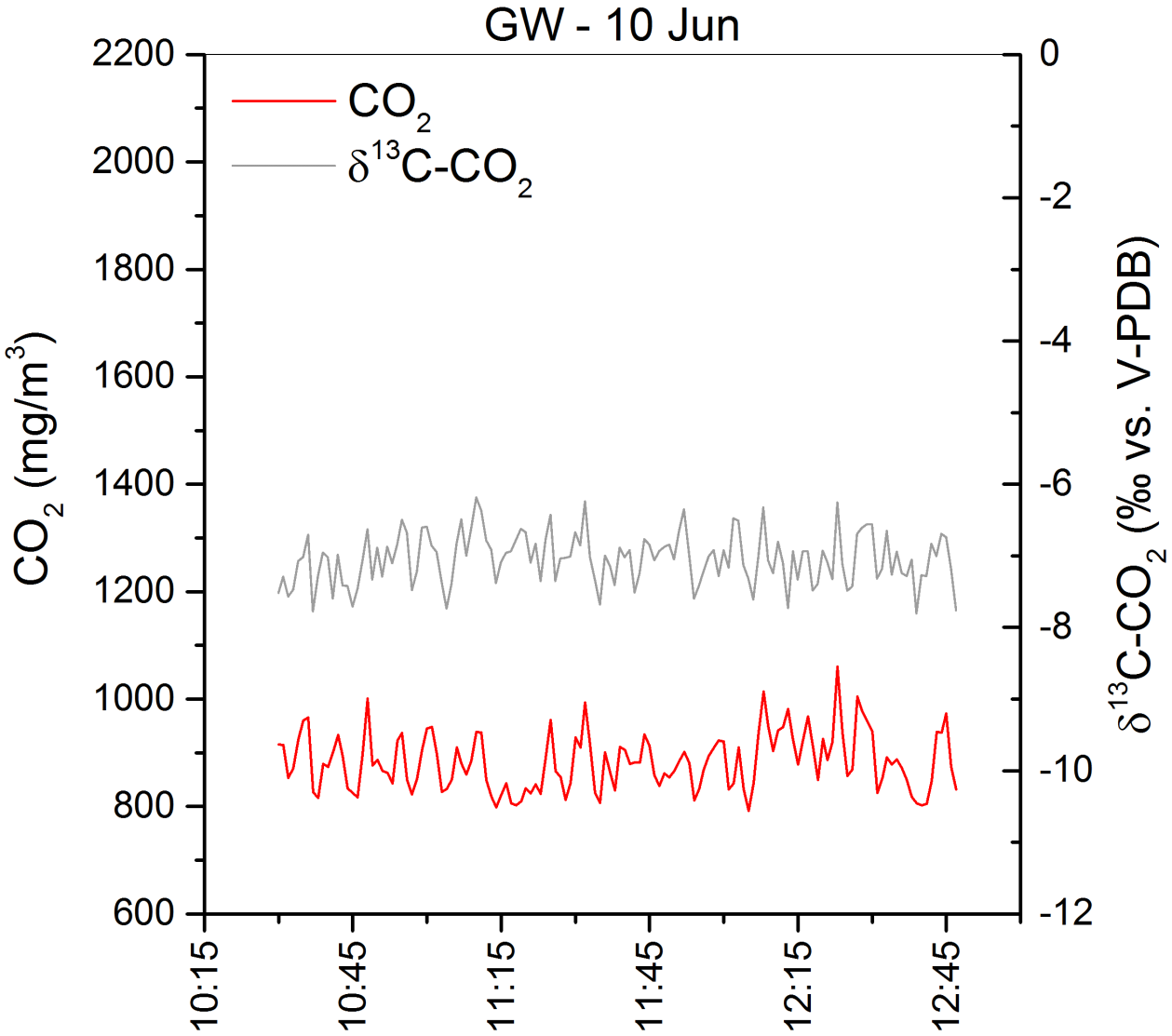

873
874 Figure A.4. CO_2 concentrations (mg/m^3; red line) and $\delta^{13}C$-CO_2 values (‰ vs. V-PDB; grey line) vs.
875 time of GW site on 10th June 2020 (morning).

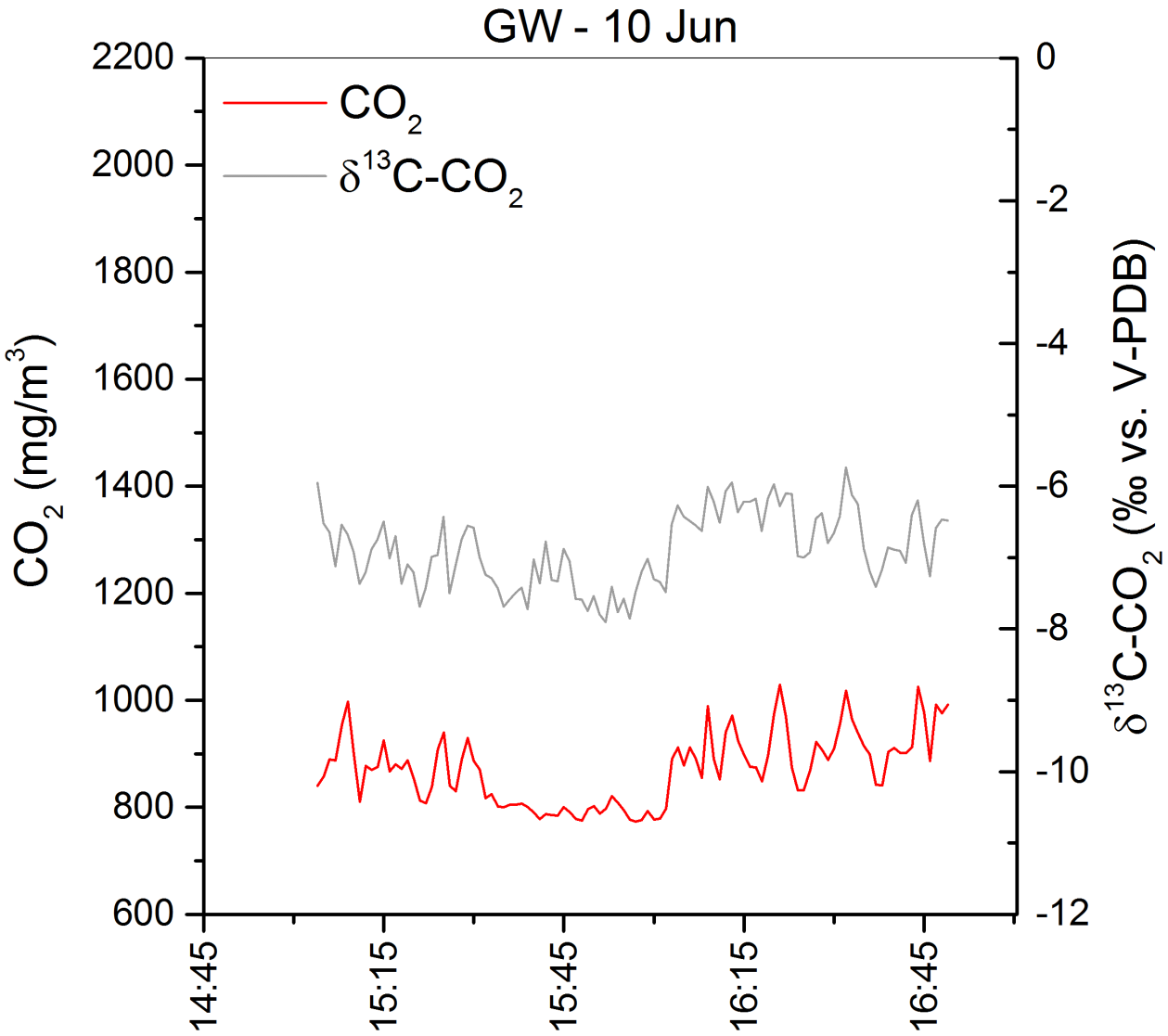

Figure A.5. CO_2 concentrations (mg/m^3; red line) and $\delta^{13}C$-CO_2 values (‰ vs. V-PDB; grey line) vs. time of GW site on 10th June 2020 (afternoon).

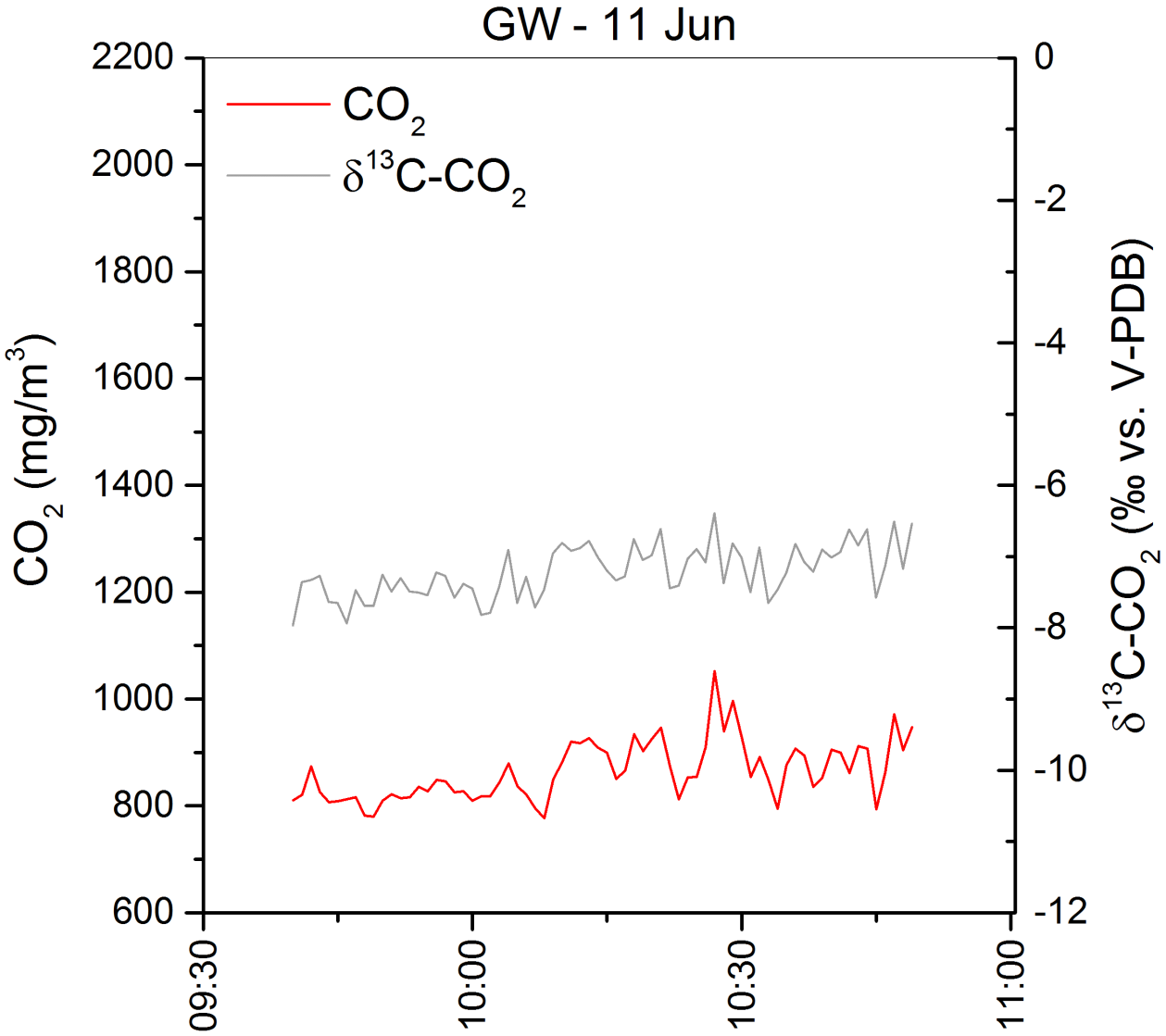

Figure A.6. CO_2 concentrations (mg/m^3; red line) and $\delta^{13}C$-CO_2 values (‰ vs. V-PDB; grey line) vs. time of GW site on 11th June 2020.

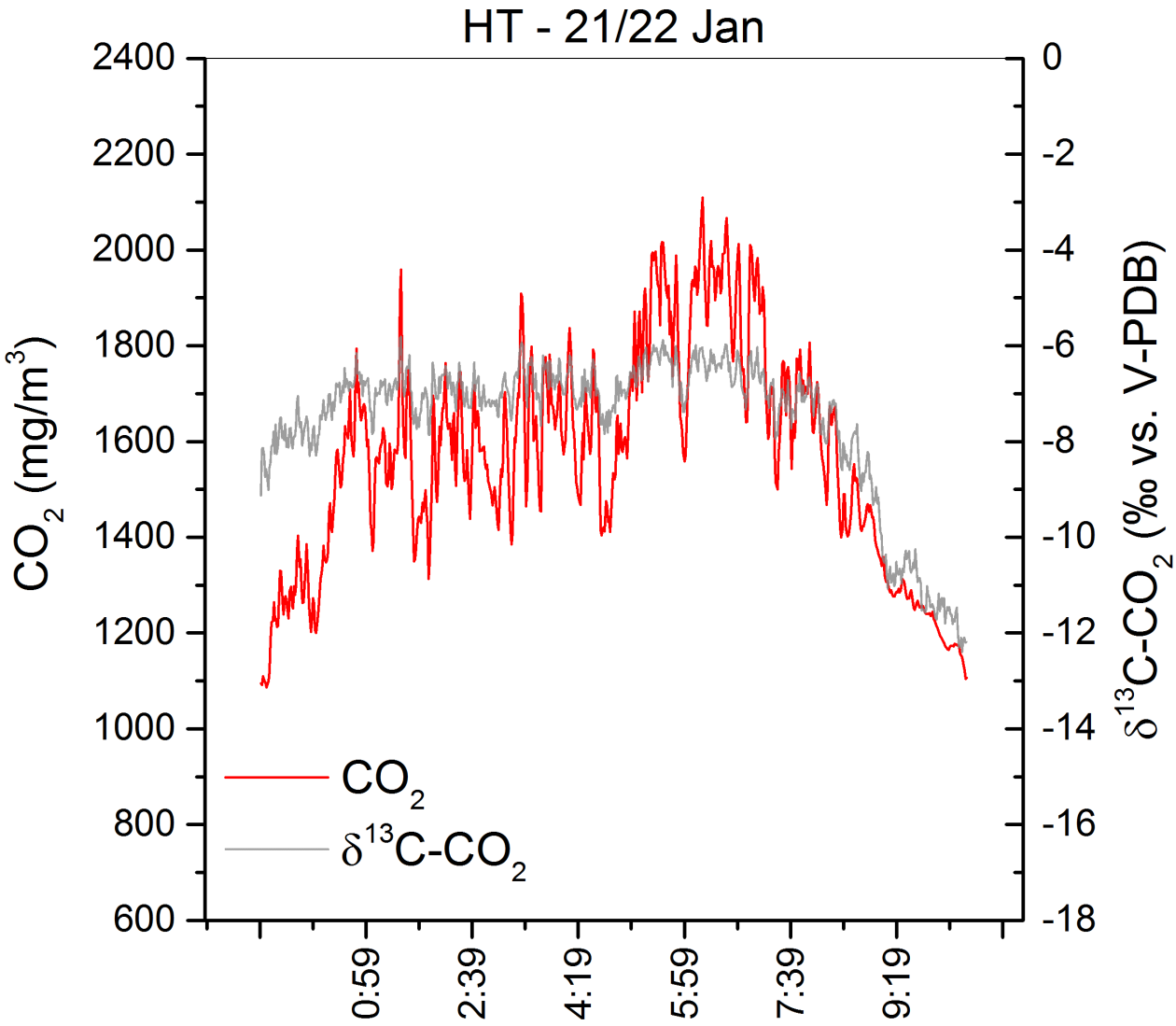

884
885 Figure A.7. CO_2 concentrations (mg/m^3; red line) and δ^{13}C-CO_2 values (‰ vs. V-PDB; grey line) vs.
886 time of HT site on 21st-22nd January 2020.
887

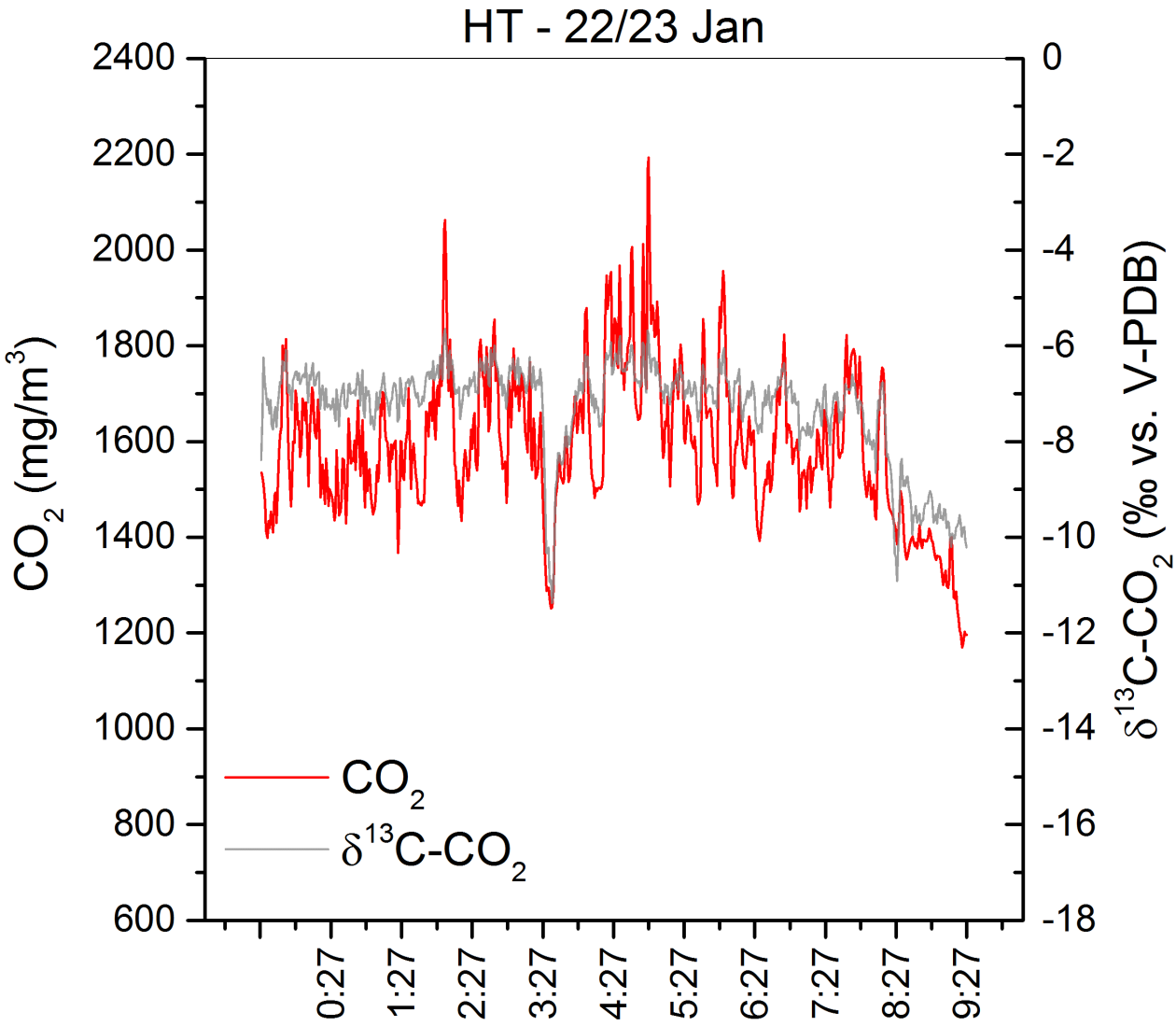

888
889 Figure A.8. CO_2 concentrations (mg/m^3; red line) and δ^{13}C-CO_2 values (‰ vs. V-PDB; grey line) vs.
890 time of HT site on 22nd-22rd January 2020.
891

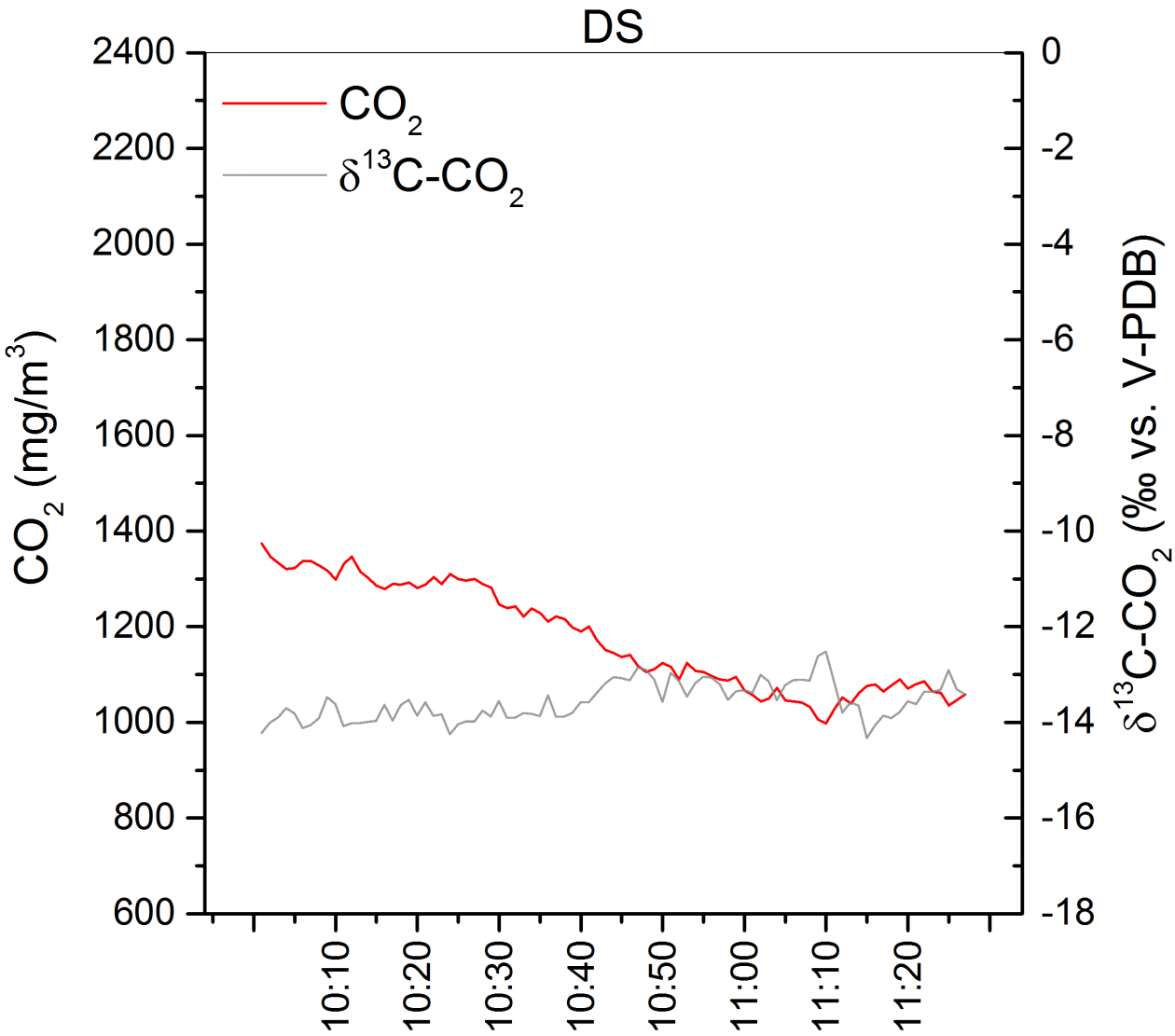

892
893 Figure A.9. CO_2 concentrations (mg/m^3; red line) and $\delta^{13}C$-CO_2 values (‰ vs. V-PDB; grey line) vs.
894 time of DS site on 23rd January 2020.
895

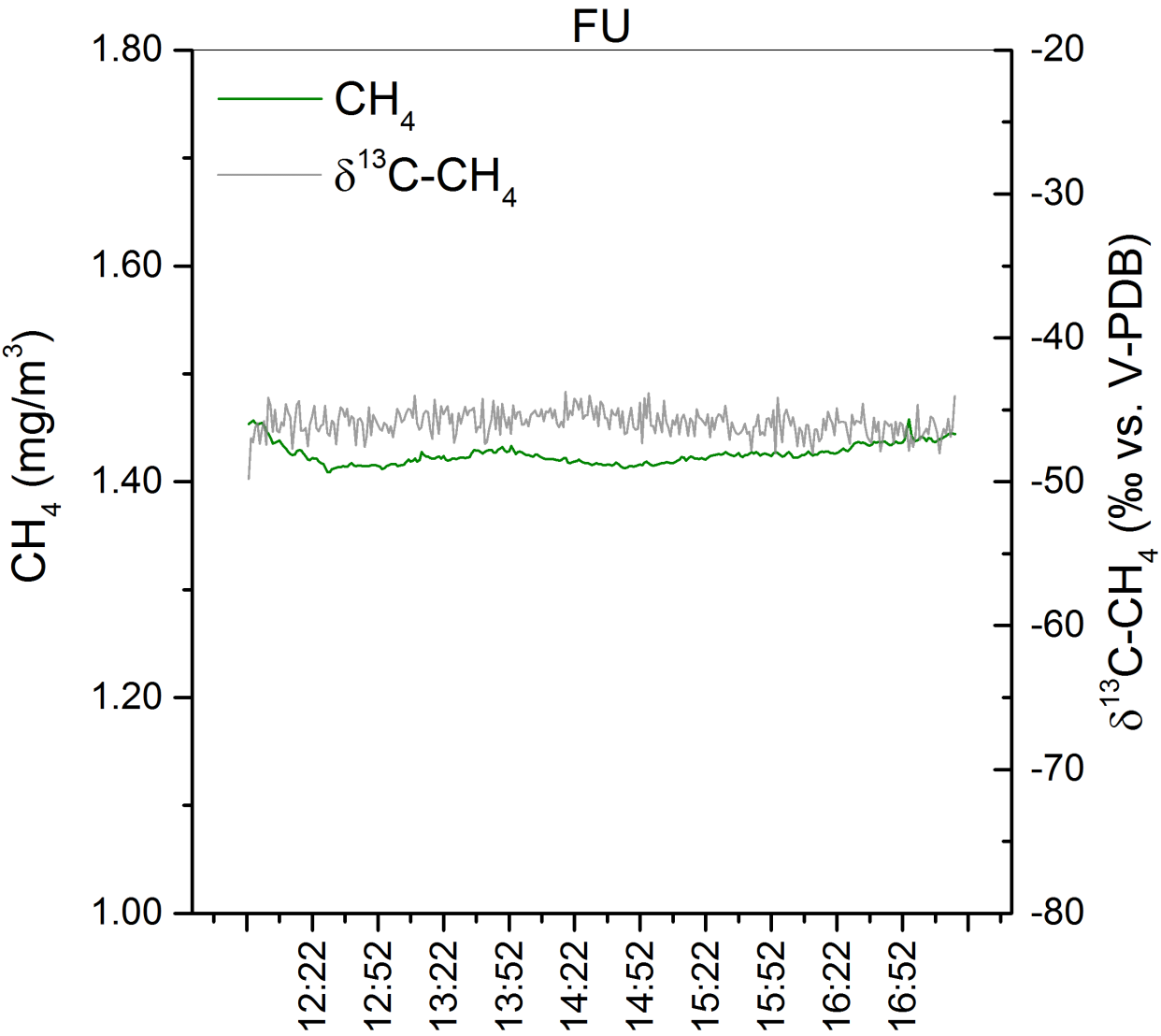

Figure A.10. CH_4 concentrations (mg/m^3; green line) and δ^{13}C-CH_4 values (‰ vs. V-PDB; grey line) vs. time of FU site on 22nd January 2020.

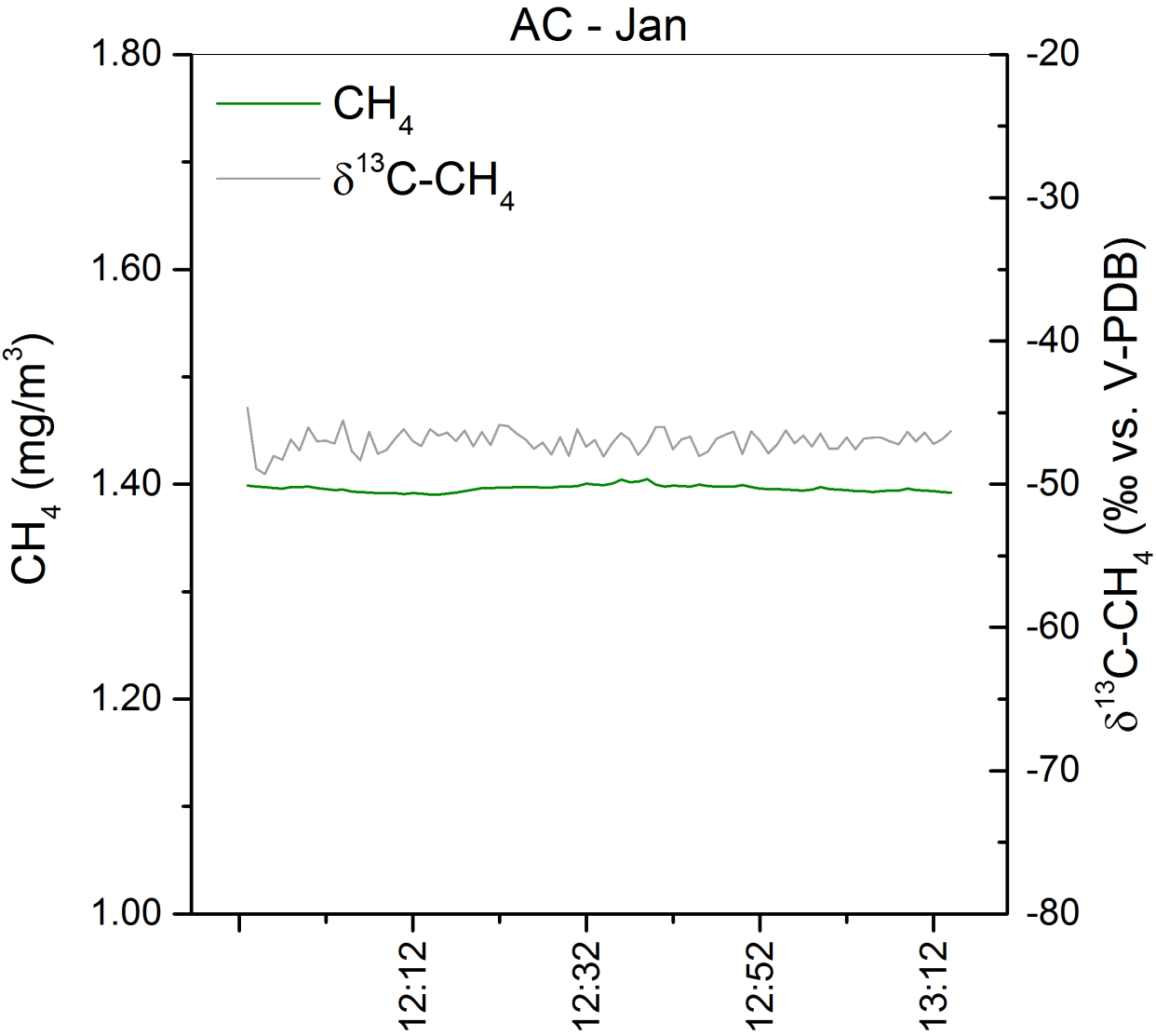

Figure A.11. CH_4 concentrations (mg/m^3; green line) and δ^{13}C-CH_4 values (‰ vs. V-PDB; grey line) vs. time of AC site on 21st January 2020.

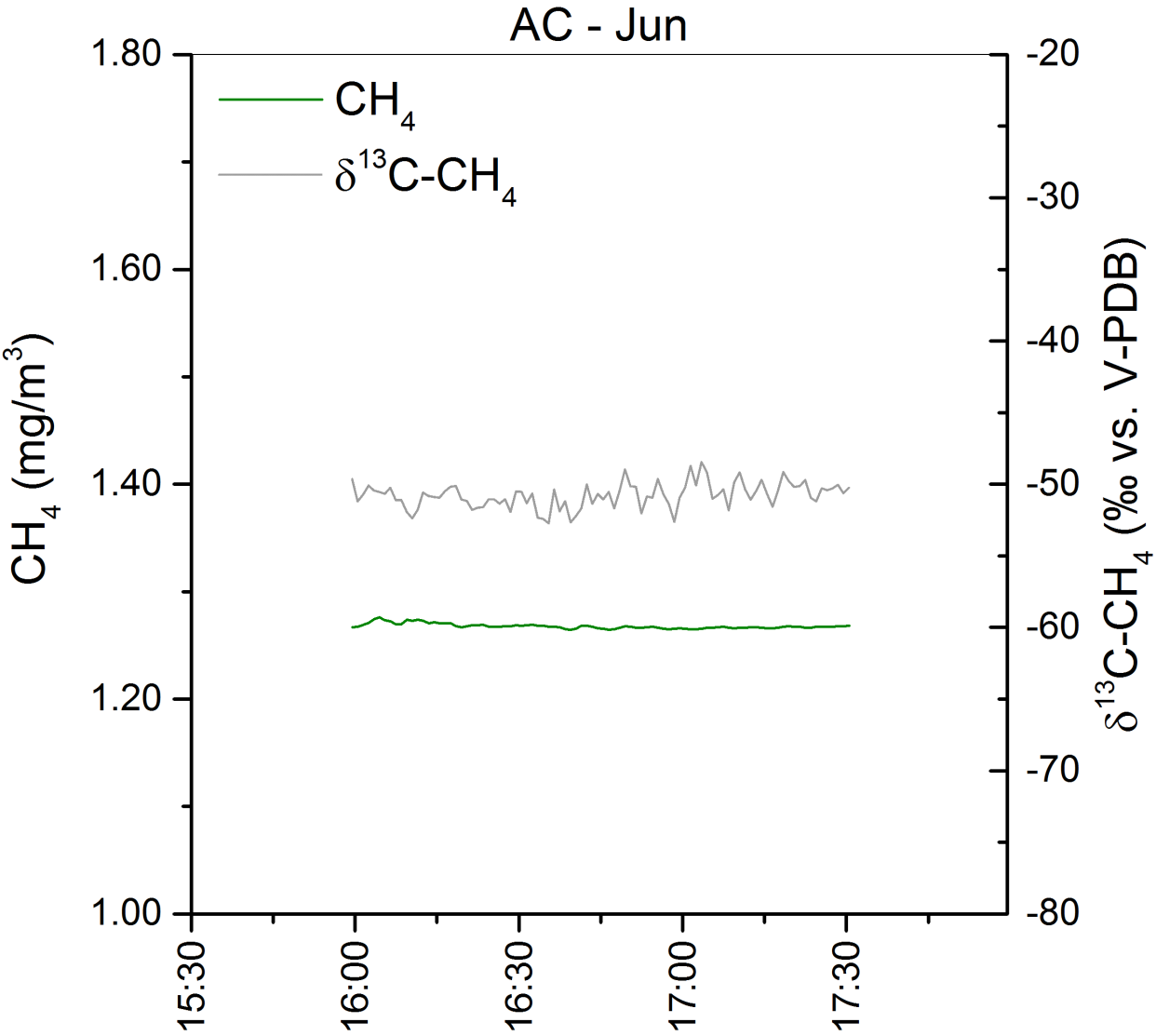

Figure A.12. CH_4 concentrations (mg/m^3; green line) and $\delta^{13}C\text{-}CH_4$ values (‰ vs. V-PDB; grey line) vs. time of AC site on 9th June 2020.

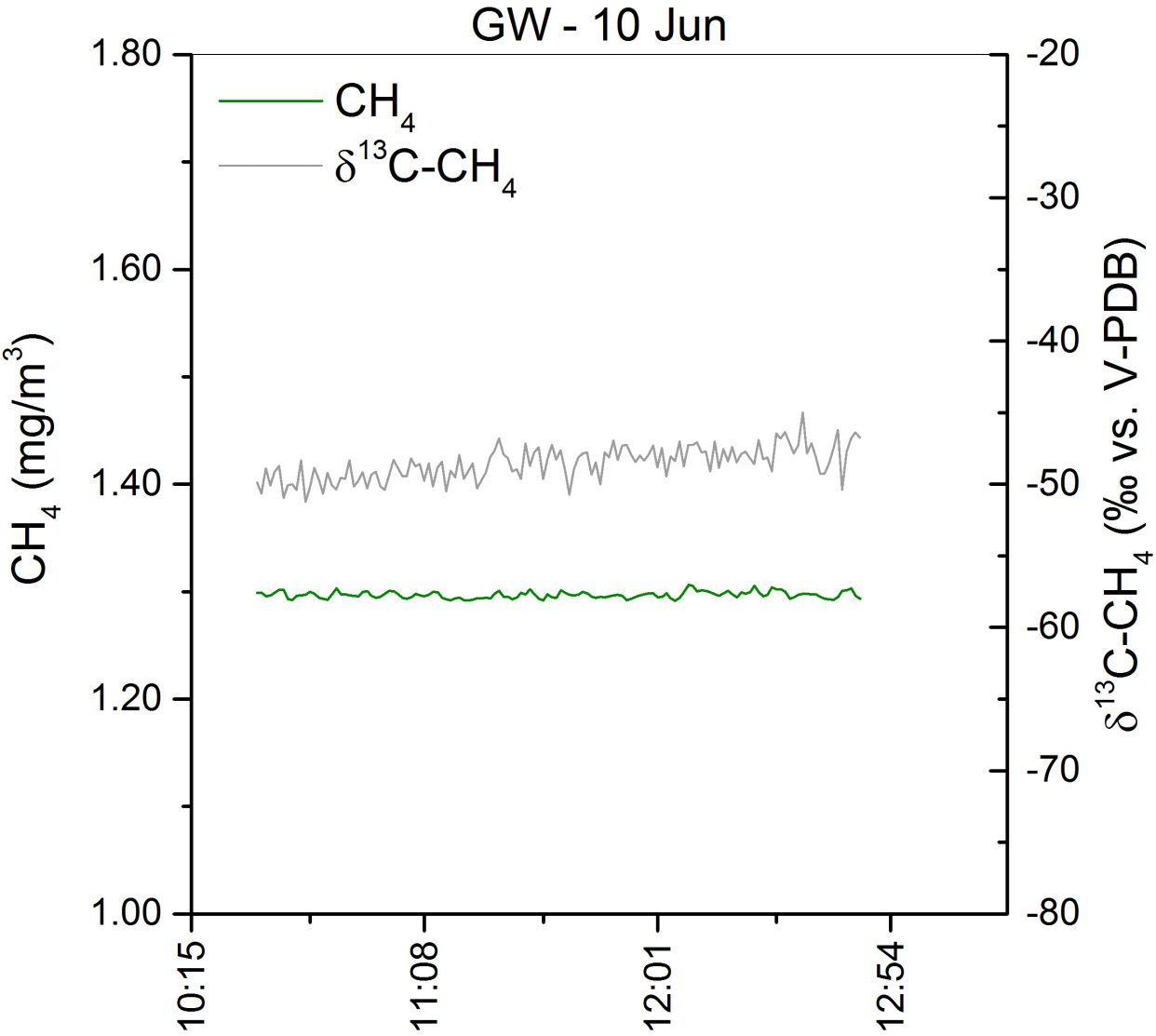

908
909 Figure A.13. CH_4 concentrations (mg/m^3; green line) and δ^{13}C-CH_4 values (‰ vs. V-PDB; grey line) vs.
910 time of GW site on 10th June 2020 (morning).
911

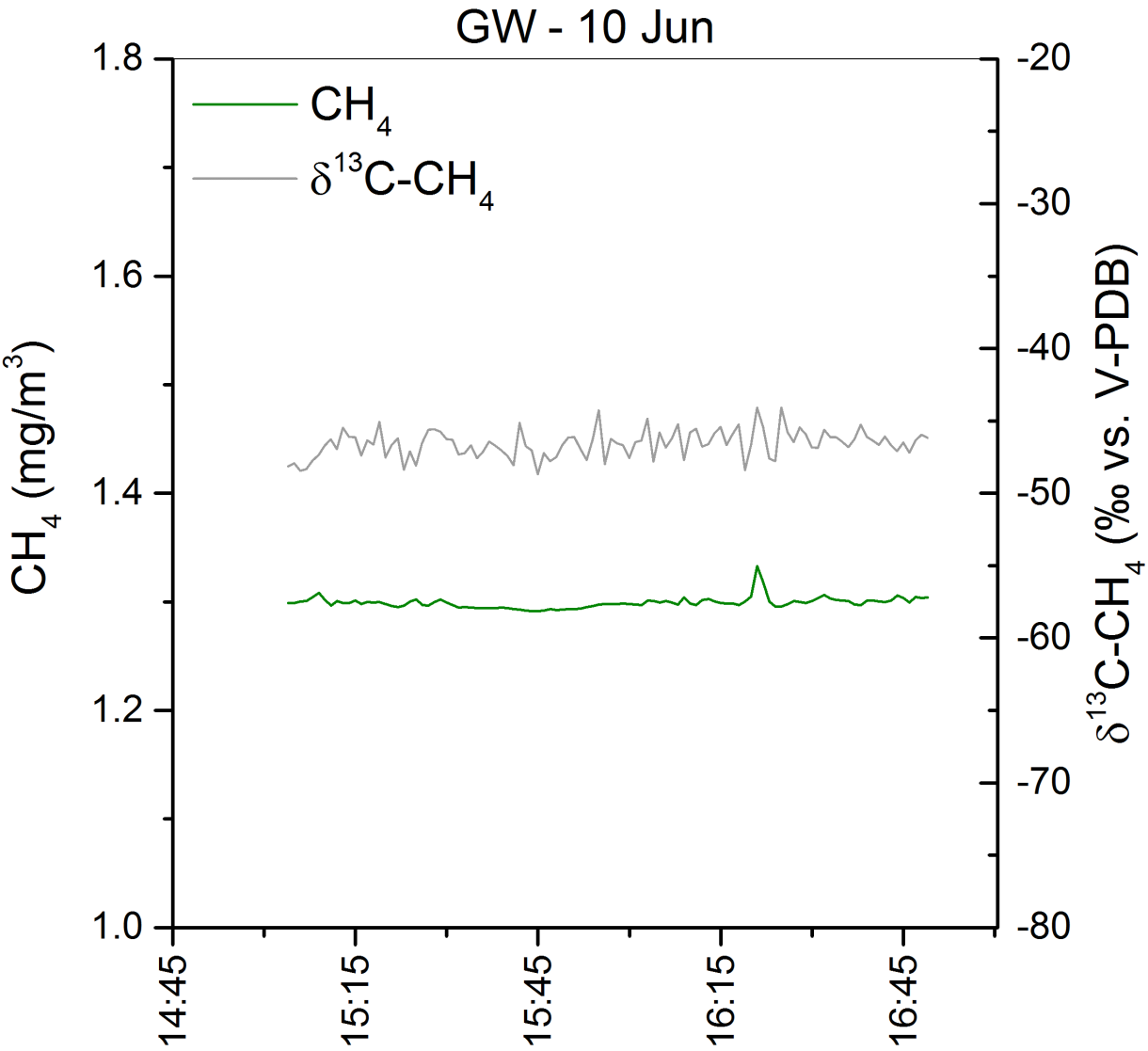

912
913 Figure A.14. CH_4 concentrations (mg/m^3; green line) and δ^{13}C-CH_4 values (‰ vs. V-PDB; grey line) vs.
914 time of GW site on 10th June 2020 (afternoon).
915

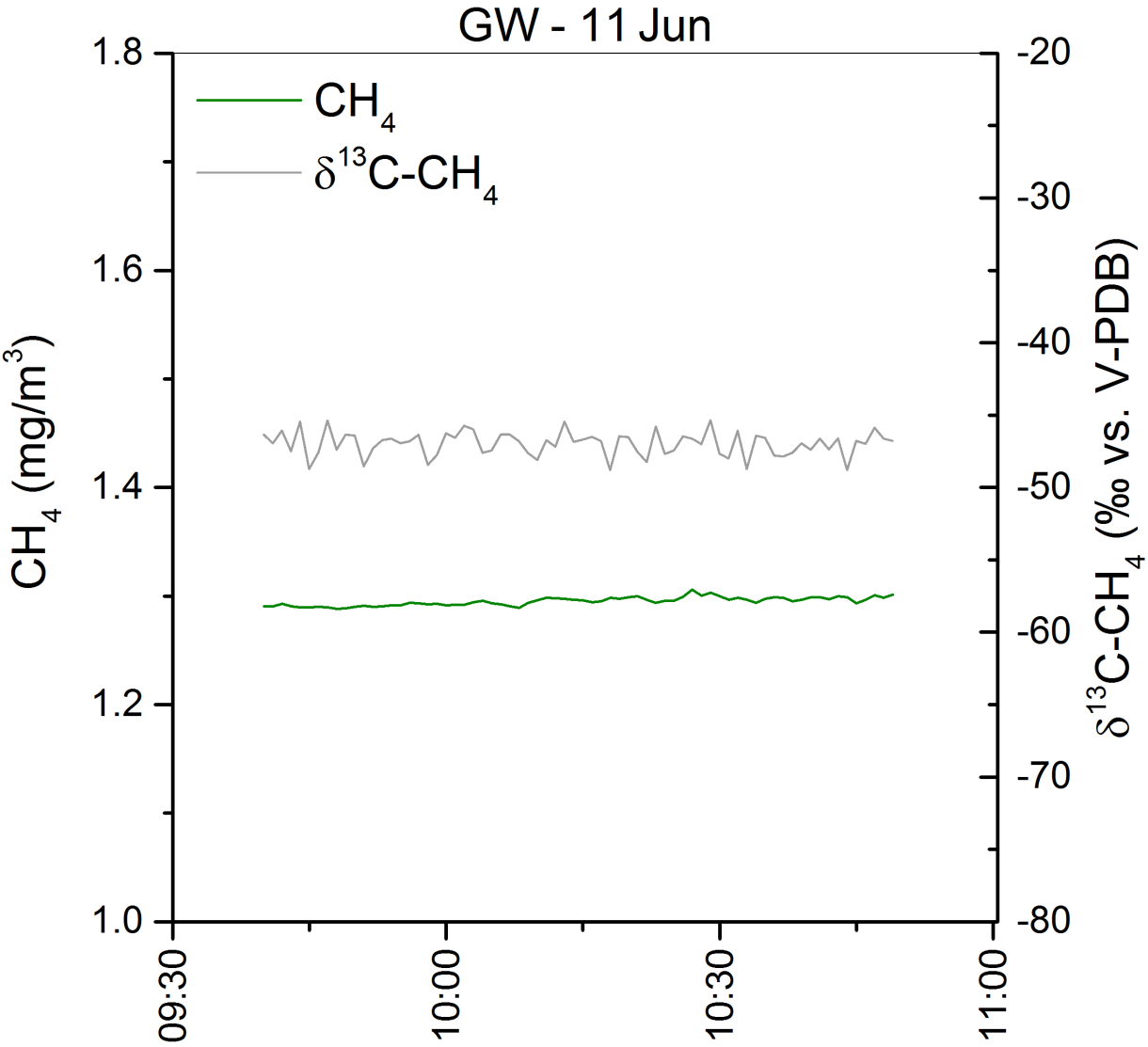

916
917 Figure A.15. CH_4 concentrations (mg/m^3; green line) and δ^{13}C-CH_4 values (‰ vs. V-PDB; grey line) vs.
918 time of GW site on 11th June 2020.
919

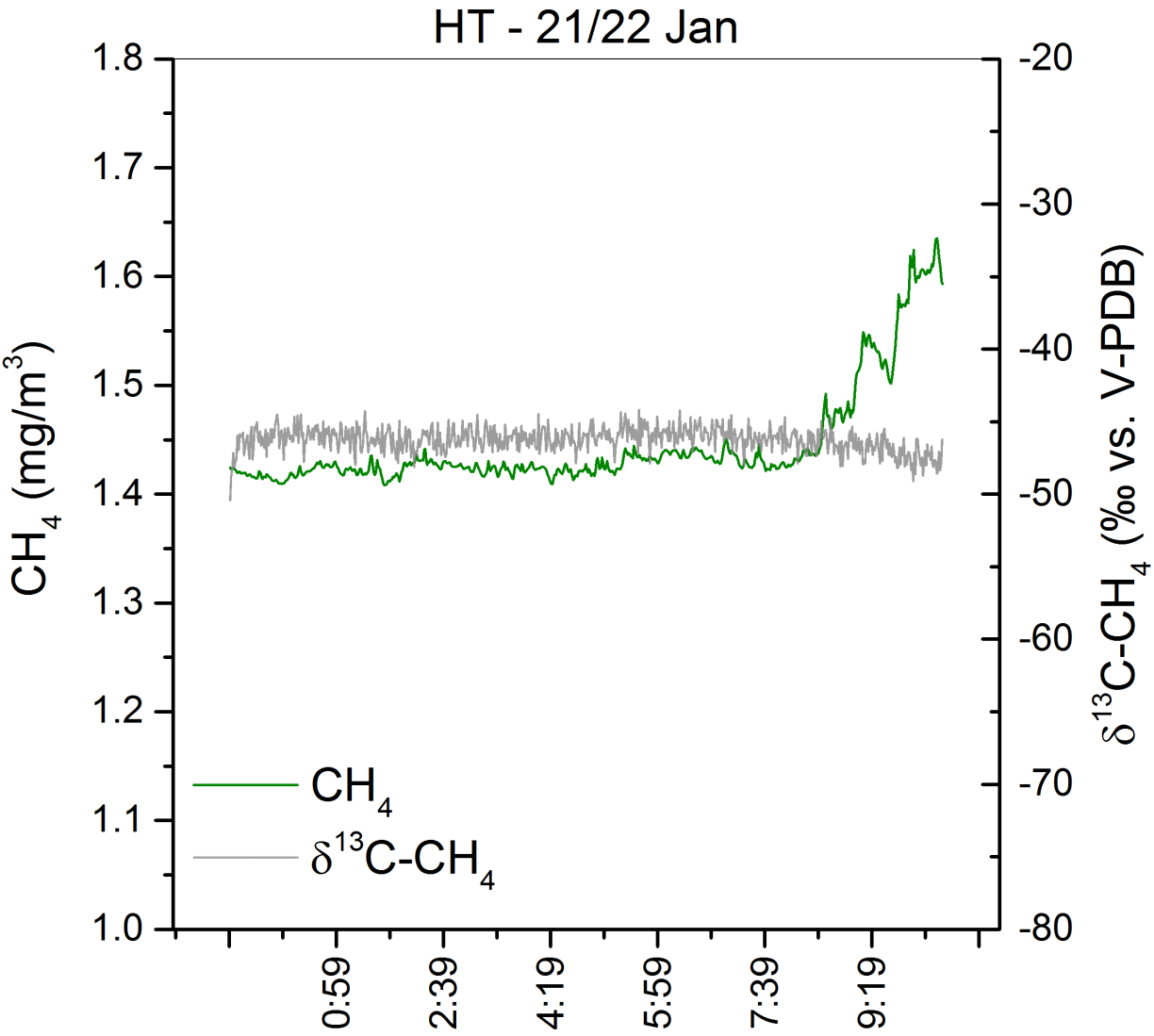

Figure A.16. CH_4 concentrations (mg/m^3; green line) and δ^{13}C-CH_4 values (‰ vs. V-PDB; grey line) vs. time of HT site on 21st-22nd January 2020.

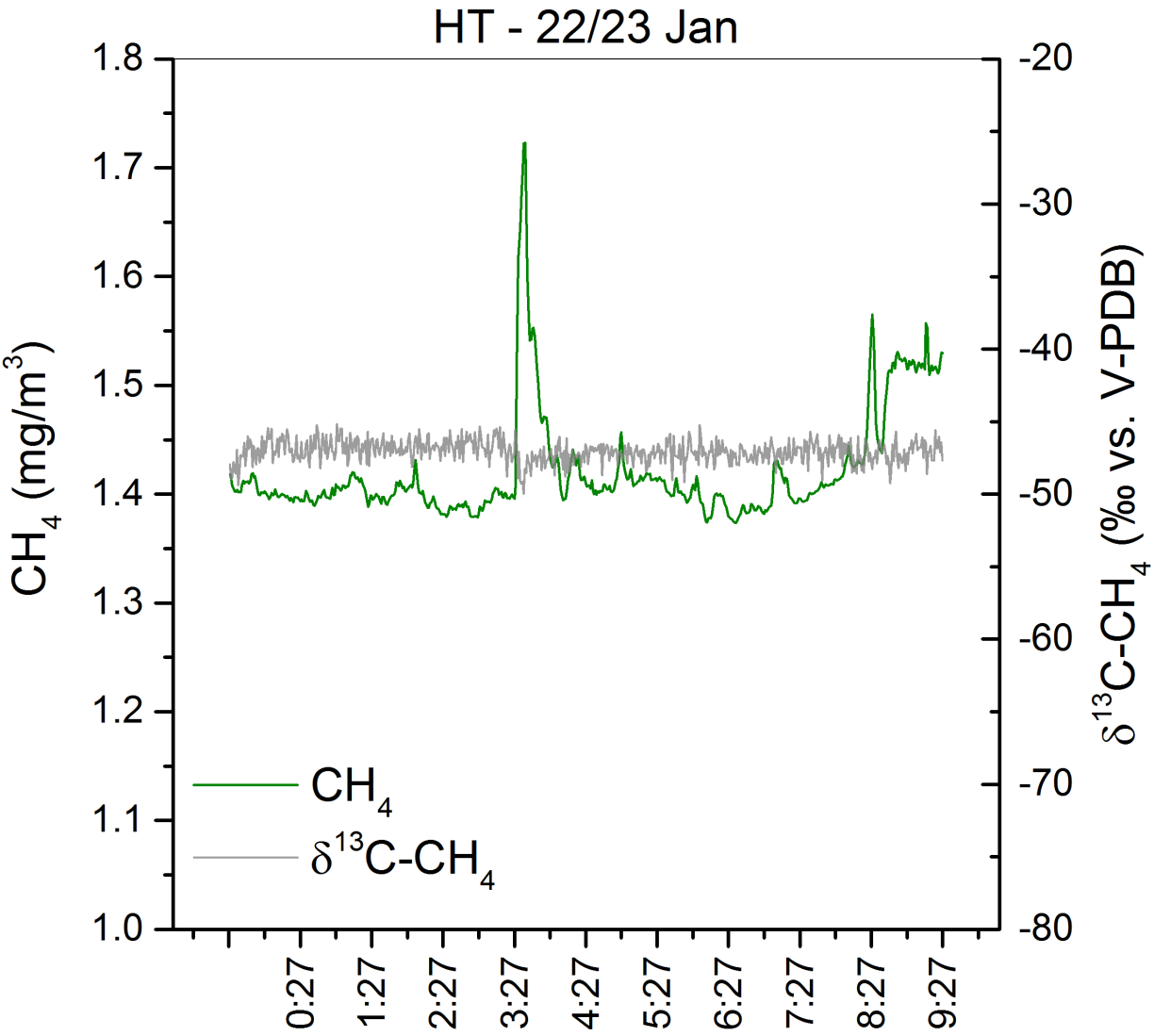

924
925 Figure A.17. CH_4 concentrations (mg/m^3; green line) and δ^{13}C-CH_4 values (‰ vs. V-PDB; grey line) vs.
926 time of HT site on 22nd-23rd January 2020.
927

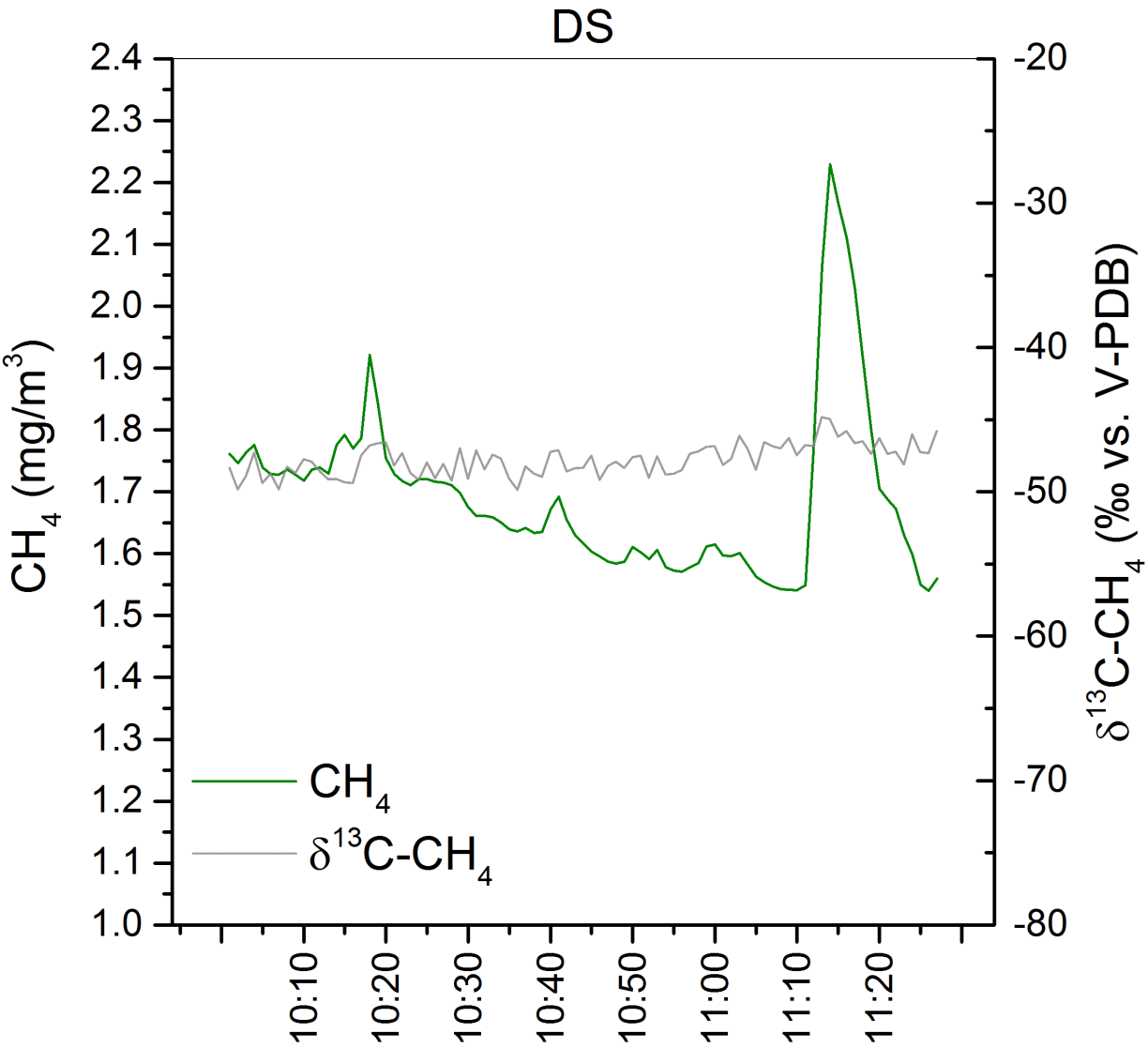

928
929 Figure A.18. CH_4 concentrations (mg/m^3; green line) and δ^{13}C-CH_4 values (‰ vs. V-PDB; grey line) vs.
930 time of DS site on 22rd January 2020.
931

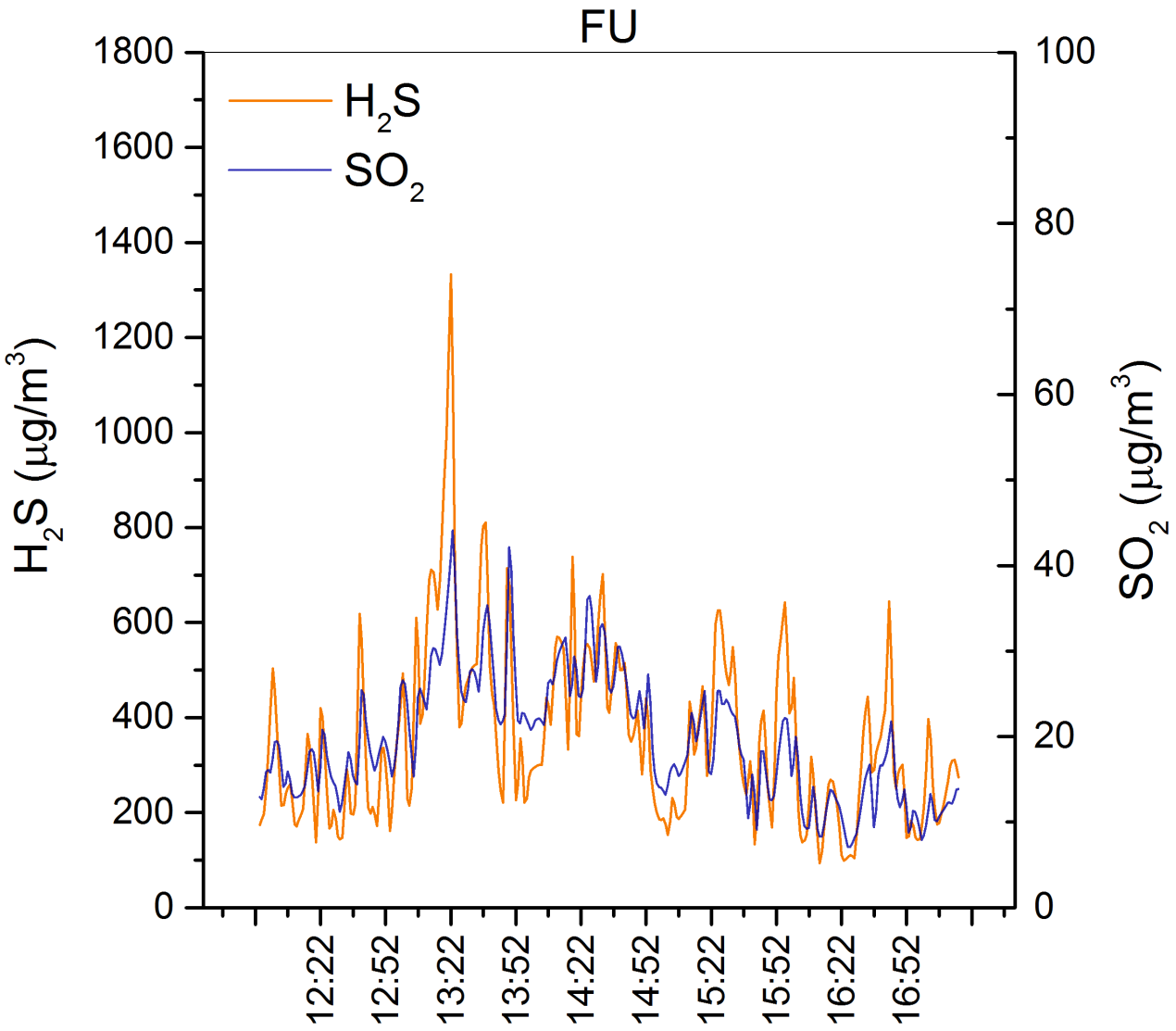

932
933 Figure A.19. H_2S and SO_2 concentrations (µg/m^3; orange and blue line, respectively) vs. time of FU
934 site on 22nd January 2020.
935

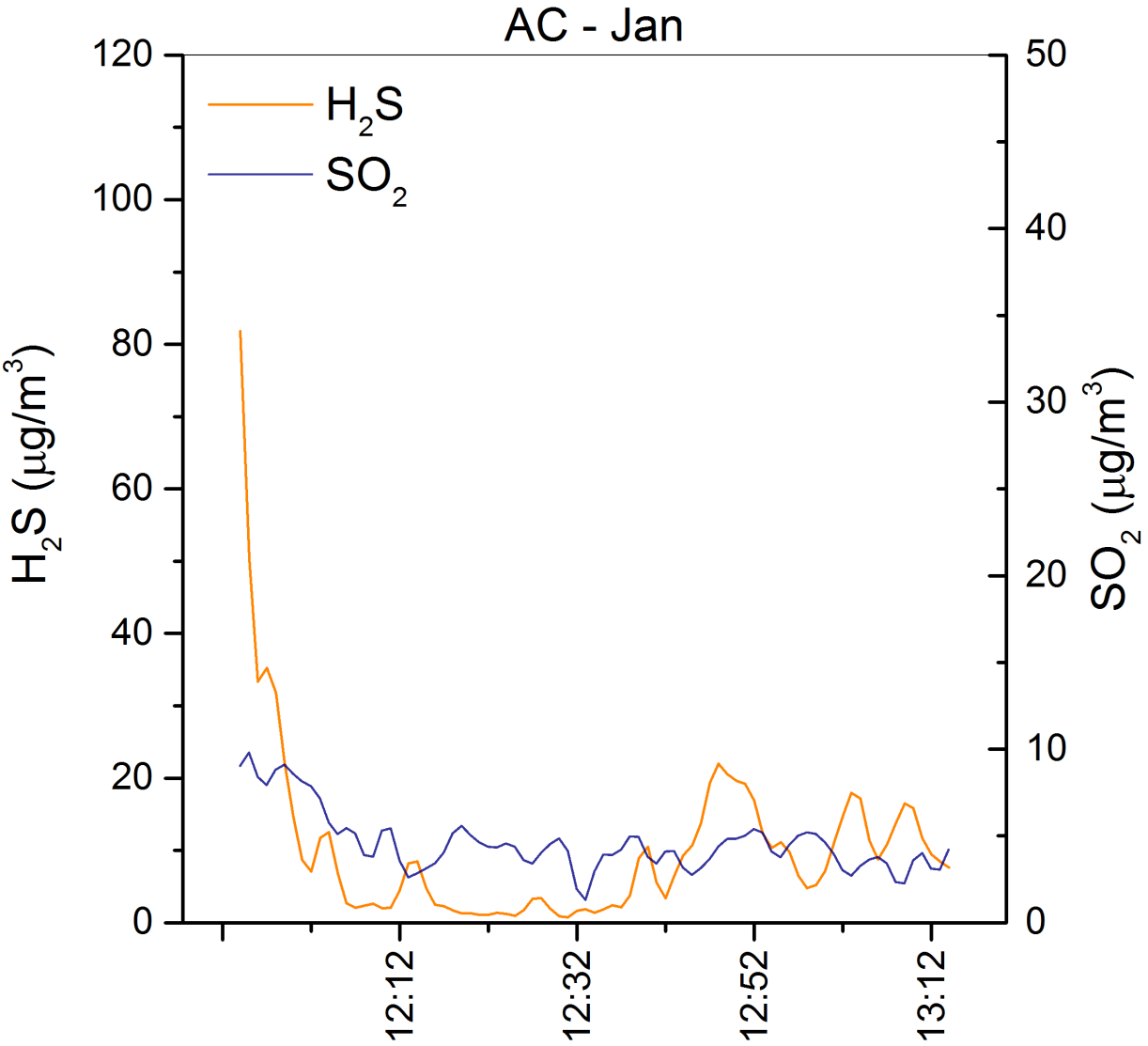

936
937 Figure A.20. H_2S and SO_2 concentrations (µg/m^3; orange and blue line, respectively) vs. time of AC
938 site on 21st January 2020.

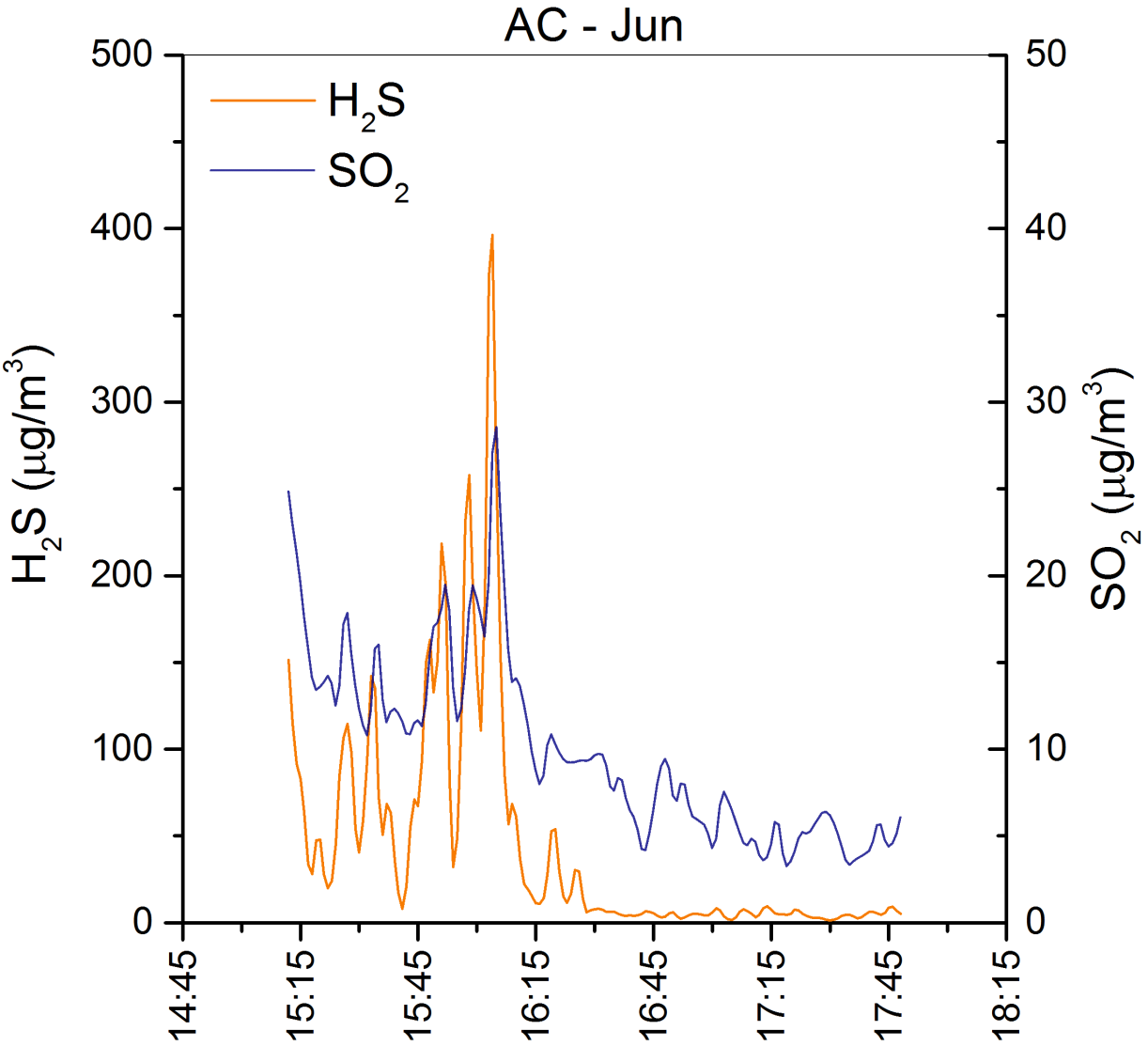

939
940 Figure A.21. H_2S and SO_2 concentrations (µg/m^3; orange and blue line, respectively) vs. time of AC
941 site on 9th June 2020.
942

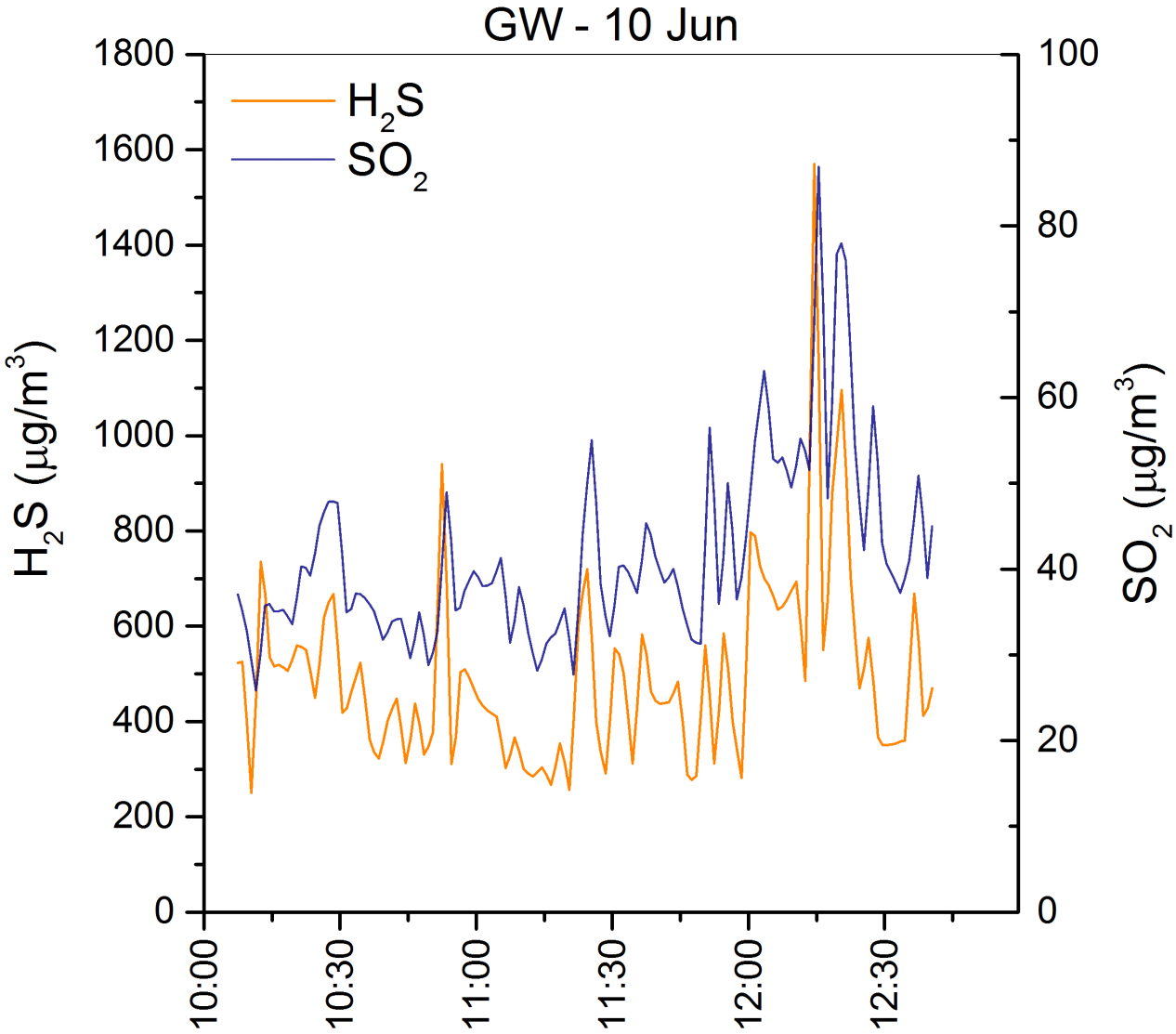

943
944 Figure A.22. H_2S and SO_2 concentrations (µg/m^3; orange and blue line, respectively) vs. time of GW
945 site on 10th June 2020 (morning).
946

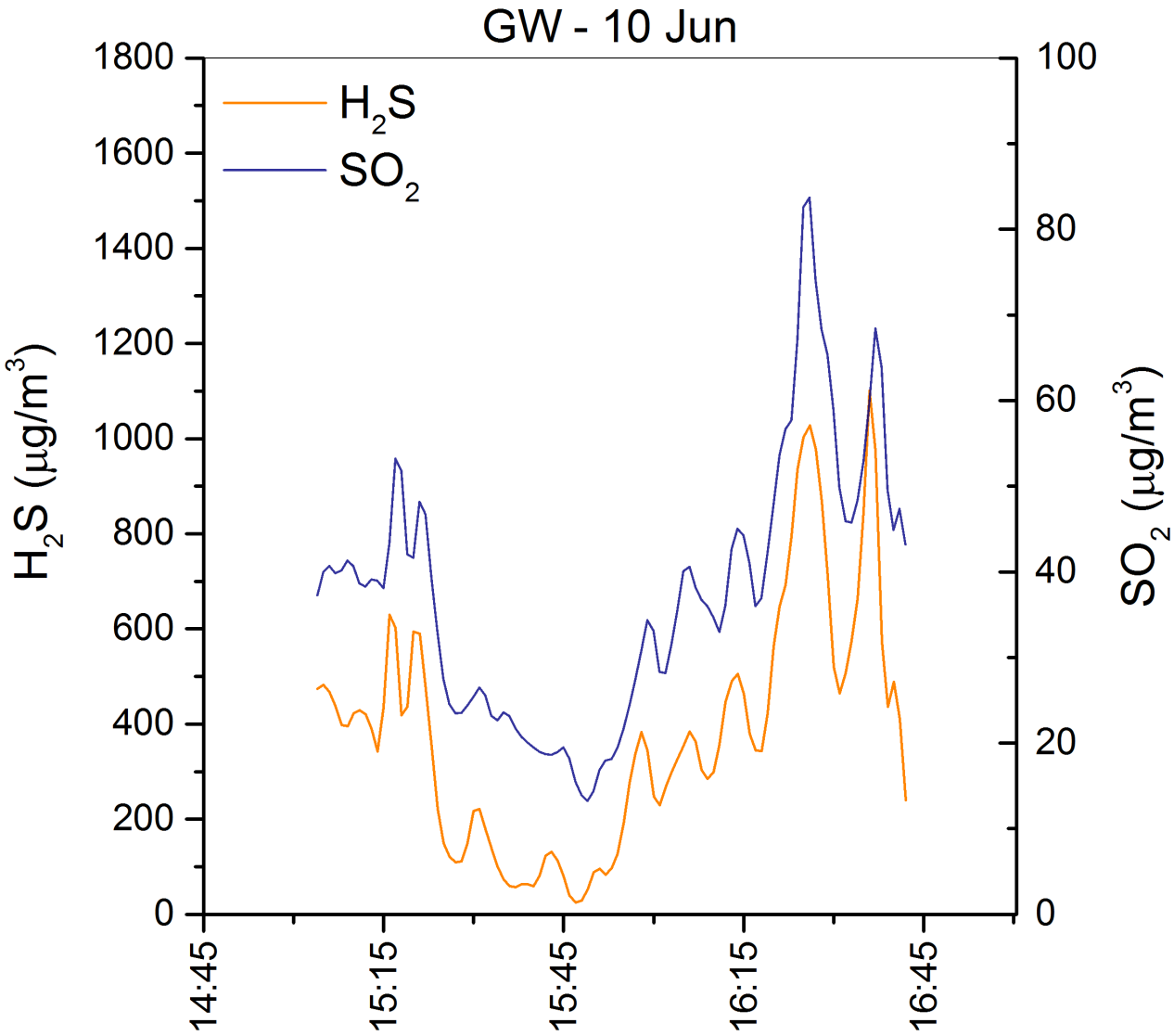

947
948 Figure A.23. H_2S and SO_2 concentrations (µg/m^3; orange and blue line, respectively) vs. time of GW
949 site on 10th June 2020 (afternoon).
950

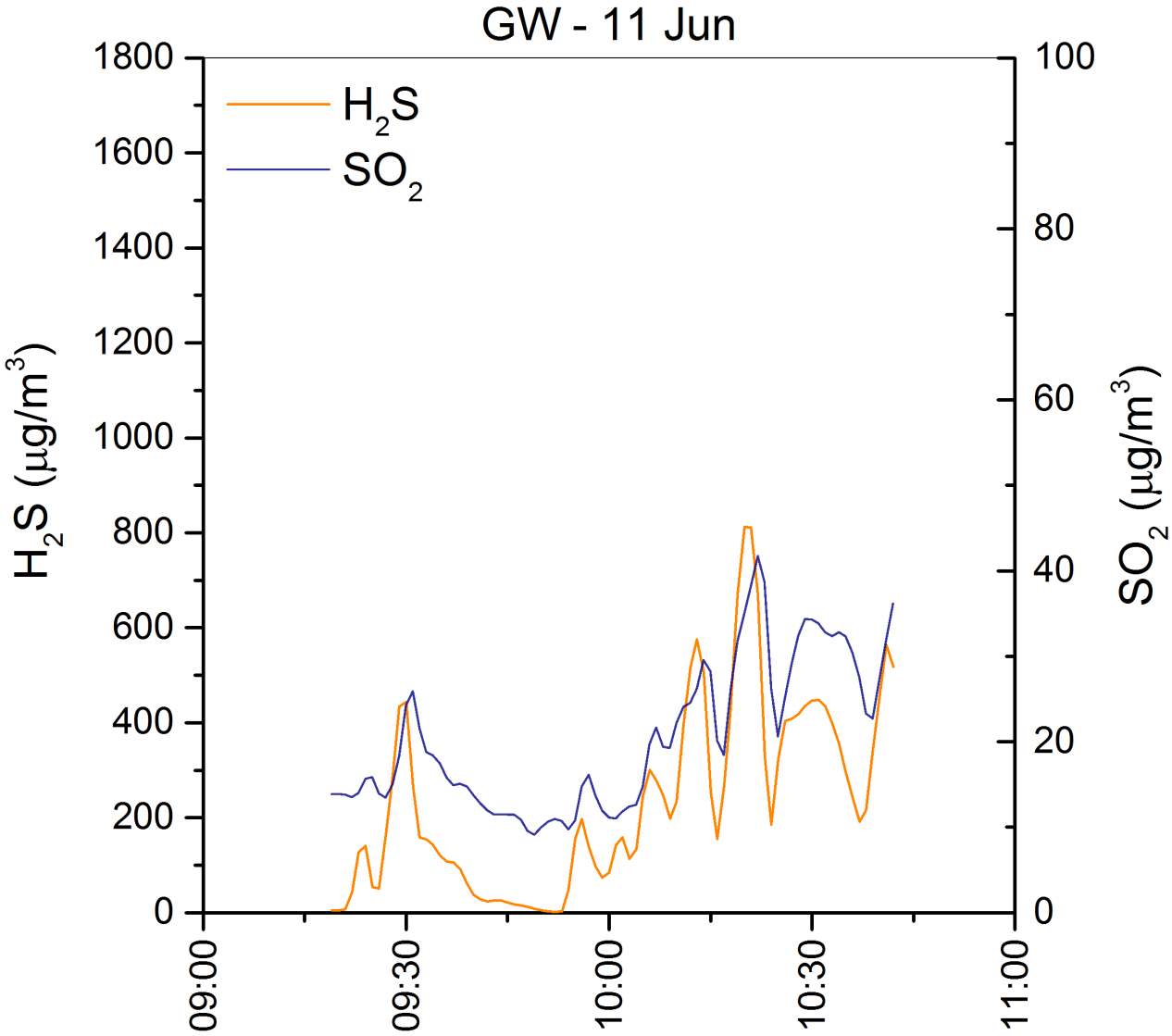

951
952 Figure A.24. H_2S and SO_2 concentrations (µg/m^3; orange and blue line, respectively) vs. time of GW
953 site on 11th June 2020.
954

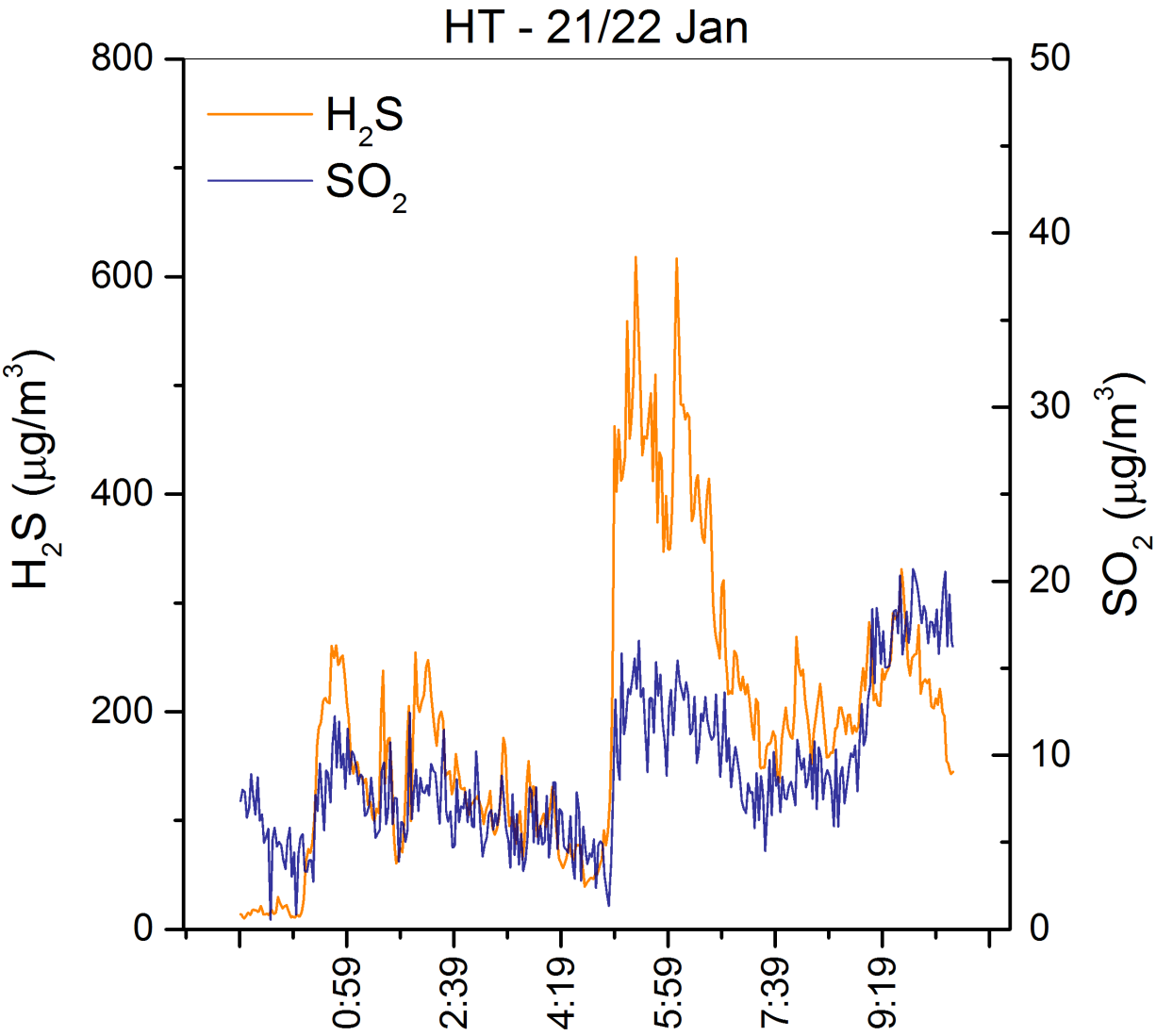

955
956 Figure A.25. H_2S and SO_2 concentrations (µg/m^3; orange and blue line, respectively) vs. time of HT
957 site on 21st-22nd January 2020.
958

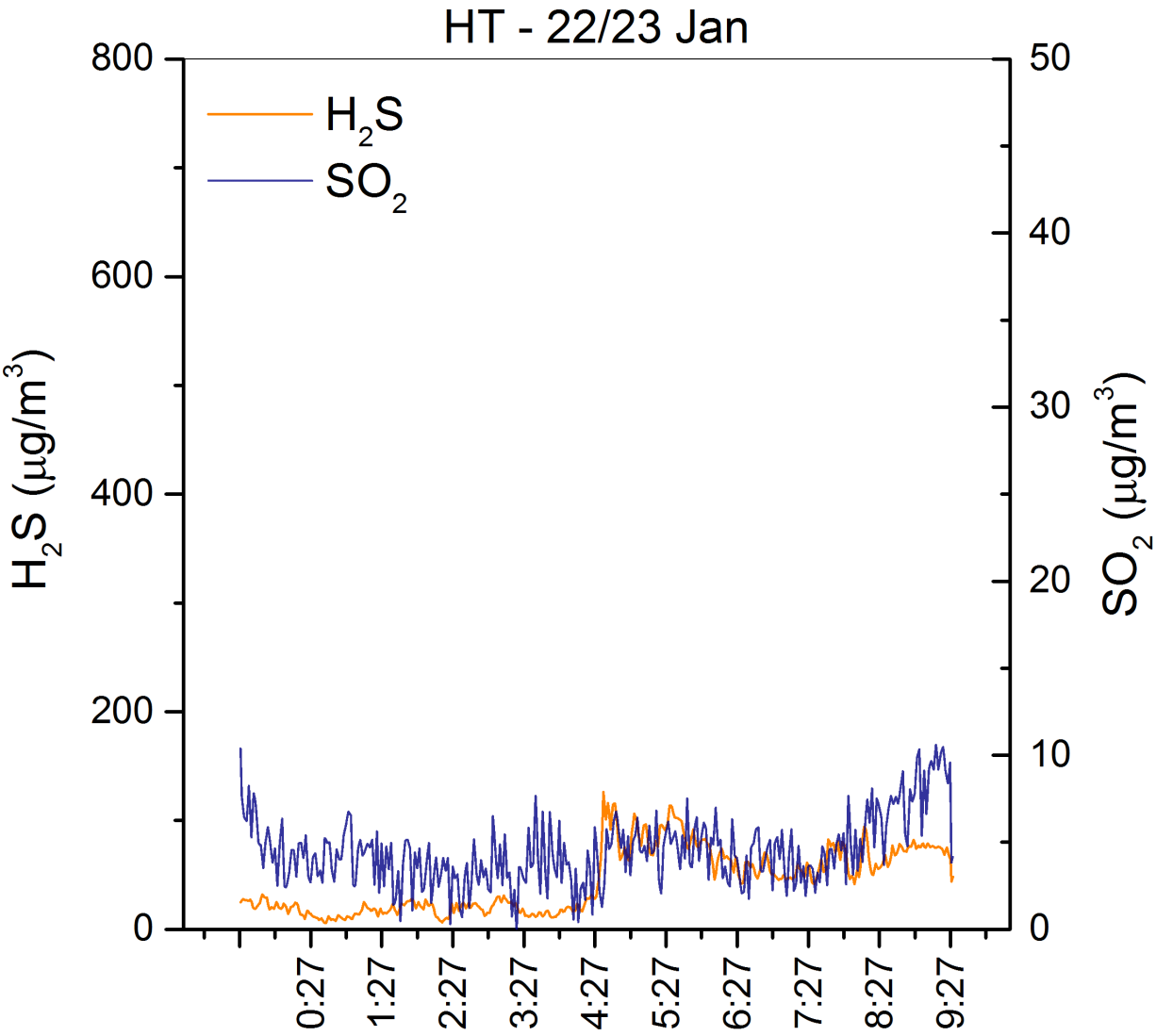

959
960 Figure A.26. H_2S and SO_2 concentrations (µg/m^3; orange and blue line, respectively) vs. time of HT
961 site on 22nd-23rd January 2020.
962

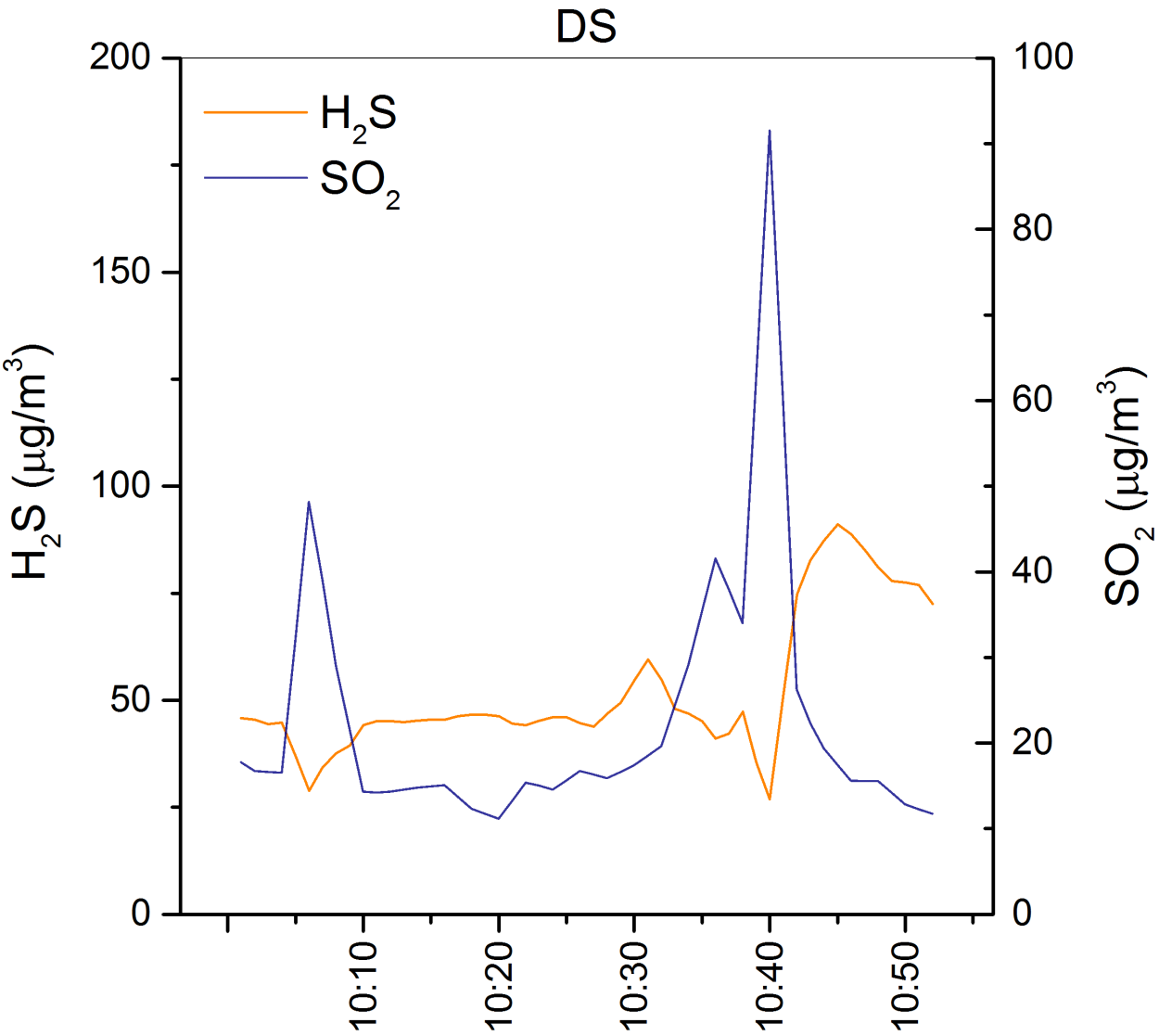

Figure A.27. H_2S and SO_2 concentrations (µg/m^3; orange and blue line, respectively) vs. time of DS site on 23rd January 2020.

969 Table1

Site	Latitude	Longitude	Distance	Date	Parameter	Start	Stop	Duration	Min	Max	Mean	Median	SD	WD	WS
FU	40.82967463	14.1478353	85 m	22/01/2020 (UTC+1)	CO_2	11:53	17:16	05 h 24 min	922	1677	1090	1054	120	variable	3-8
					CH_4	11:53	17:16	05 h 24 min	1.41	1.46	1.43	1.42	0.009		
					$\delta^{13}C\text{-}CO_2$	11:53	17:16	05 h 24 min	-10.51	-5.94	-8.61	-8.73	0.87		
					$\delta^{13}C\text{-}CH_4$	11:53	17:16	05 h 24 min	-49.8	-43.8	-45.9	-45.9	0.88		
					SO_2	11:54	17:16	05 h 23 min	7.05	44	20	18	7.3		
					H_2S	11:54	17:16	05 h 23 min	94	1333	362	326	184		
AC	40.83010249	14.14789704	120 m	21/01/2020 (UTC+1)	CO_2	16:50	18:11	01 h 22 min	862	1197	980	939	107	NE-NNE	13
					CH_4	16:50	18:11	01 h 22 min	1.39	1.40	1.40	1.40	0.003		
					$\delta^{13}C\text{-}CO_2$	16:50	18:11	01 h 22 min	-10.30	-7.29	-8.85	-8.84	0.73		
					$\delta^{13}C\text{-}CH_4$	16:50	18:11	01 h 22 min	-49.3	-44.7	-47.0	-47.0	0.75		
					SO_2	16:51	18:11	01 h 21 min	1.30	9.79	4.58	4.19	1.7		
					H_2S	16:51	18:11	01 h 21 min	0.78	82	10	7.64	12		
AC	40.83010249	14.14789704	120 m	09/06/2020 (UTC+2)	CO_2	16:00	17:31	01 h 32 min	746	1068	831	801	77	W	19-22
					CH_4	16:00	17:31	01 h 32 min	1.26	1.28	1.27	1.27	0.002		
					$\delta^{13}C\text{-}CO_2$	16:00	17:31	01 h 32 min	-9.48	-6.82	-8.43	-8.61	0.61		
					$\delta^{13}C\text{-}CH_4$	16:00	17:31	01 h 32 min	-52.8	-48.5	-50.8	-50.7	0.88		
					SO_2	15:12	17:48	02 h 37 min	3.26	29	10	9.22	5.4		
					H_2S	15:12	17:48	02 h 37 min	1.40	396	45	8.48	68		
GW	40.82580187	14.14767757	40 m	10/06/2020 (UTC+2)	CO_2	10:30	12:47	02 h 18 min	792	1061	884	879	53	W	11-24
					CH_4	10:30	12:47	02 h 18 min	1.29	1.31	1.30	1.30	0.003		
					$\delta^{13}C\text{-}CO_2$	10:30	12:47	02 h 18 min	-7.81	-6.19	-7.05	-7.02	0.35		
					$\delta^{13}C\text{-}CH_4$	10:30	12:47	02 h 18 min	-51.2	-45.0	-48.6	-48.5	1.17		
					SO_2	10:08	12:41	02 h 34 min	26	87	42	39	10.6		
					H_2S	10:08	12:41	02 h 34 min	250	1570	497	460	188		
GW	40.82580187	14.14767757	40 m	10/06/2020 (UTC+2)	CO_2	15:04	16:49	01 h 46 min	774	1029	871	875	66	W	11-24
					CH_4	15:04	16:49	01 h 46 min	1.29	1.33	1.30	1.30	0.005		
					$\delta^{13}C\text{-}CO_2$	15:04	16:49	01 h 46 min	-7.91	-5.74	-6.89	-6.90	0.52		
					$\delta^{13}C\text{-}CH_4$	15:04	16:49	01 h 46 min	-48.7	-44.1	-46.6	-46.6	0.94		
					SO_2	15:04	16:42	01 h 39 min	13	84	37	38	15.5		
					H_2S	15:04	16:42	01 h 39 min	25	1101	375	357	254		
GW	40.82580187	14.14767757	40 m	11/06/2020 (UTC+2)	CO_2	9:40	10:49	01 h 10 min	777	1052	864	853	55	SSW-SW	11-19
					CH_4	9:40	10:49	01 h 10 min	1.29	1.31	1.30	1.30	0.004		
					$\delta^{13}C\text{-}CO_2$	9:40	10:49	01 h 10 min	-7.97	-6.39	-7.22	-7.27	0.36		
					$\delta^{13}C\text{-}CH_4$	9:40	10:49	01 h 10 min	-48.8	-45.4	-47.0	-46.8	0.84		
					SO_2	9:19	10:42	01 h 24 min	9.10	42	20	18	8.6		
					H_2S	9:19	10:42	01 h 24 min	2.28	813	233	175	198		
HT	40.83085249	14.15036252	325 m	21-22/01/2020 (UTC+1)	CO_2	23:20	10:25	11 h 06 min	1087	2109	1567	1580	230	N-NNE	5-11
					CH_4	23:20	10:25	11 h 06 min	1.41	1.63	1.45	1.43	0.049		
					$\delta^{13}C\text{-}CO_2$	23:20	10:25	11 h 06 min	-12.41	-5.82	-7.58	-7.06	1.50		
					$\delta^{13}C\text{-}CH_4$	23:20	10:25	11 h 06 min	-50.4	-44.2	-46.3	-46.2	0.85		
					SO_2	23:20	10:25	11 h 06 min	0.54	20.68	9.15	8.22	4.2		
					H_2S	23:20	10:25	11 h 06 min	10	618	192	180	126		
HT	40.83085249	14.15036252	325 m	22-23/01/2020 (UTC+1)	CO_2	23:28	9:27	10 h 00 min	1170	2193	1591	1584	154	variable	<8
					CH_4	23:28	9:27	10 h 00 min	1.37	1.72	1.42	1.40	0.051		
					$\delta^{13}C\text{-}CO_2$	23:28	9:27	10 h 00 min	-11.38	-5.65	-7.31	-7.00	1.03		
					$\delta^{13}C\text{-}CH_4$	23:28	9:27	10 h 00 min	-50.0	-45.2	-47.1	-47.1	0.78		
					SO_2	23:28	9:29	10 h 02 min	u.d.l.	11	4.50	4.33	1.9		
					H_2S	23:28	9:29	10 h 02 min	5.83	126	44	35	29		
DS	40.83165231	14.15530663	800 m	23/01/2020 (UTC+1)	CO_2	10:01	11:27	01 h 27 min	998	1374	1176	1145	110	N-NE	3-5
					CH_4	10:01	11:27	01 h 27 min	1.54	2.23	1.69	1.66	0.136		
					$\delta^{13}C\text{-}CO_2$	10:01	11:27	01 h 27 min	-14.3	-12.5	-13.6	-13.6	0.39		
					$\delta^{13}C\text{-}CH_4$	10:01	11:27	01 h 27 min	-49.9	-44.8	-47.8	-47.7	1.10		
					SO_2	10:01	10:52	00 h 52 min	11	92	23	17	15		
					H_2S	10:01	10:52	00 h 52 min	27	91	52	46	16		

*WGS 84

970

971

Table2

Site		$\delta^{13}C\text{-}CO_2$	Standard error	R^2	$\delta^{13}C\text{-}CH_4$	Standard error	R^2
FU	22 Jan	-0.41	0.21	0.82049	-	-	-
AC	21 Jan	-2.75	0.29	0.85113	-	-	-
	9 Jun	-1.75	0.16	0.95343	-	-	-
GW	10 Jun (morning)	-6.54	0.44	0.00247	-	-	-
	10 Jun (afternoon)	-1.21	0.38	0.68901	-	-	-
	11 Jun	-2.51	0.3	0.78132	-	-	-
HT	21-22 Jan (night)	-2.85	0.06	0.93457	-	-	-
	21-22 Jan (morning)	-	-	-	-60.28	0.56	0.7
	22-23 Jan (night)	0.26	0.28	0.64373	-58.36	0.63	0.48
	22-23 Jan (morning)	-	-	-	-47.01	0.66	-0.005
DS	23 Jan	-16.3	0.28	0.5396	-44.48	1.36	0.06